

Università di Genova
Dipartimento di Ingegneria delle Costruzioni, dell'Ambiente e del Territorio
Via Montallegro 1
16145 Genova Italy
e-mail: matteo.bargiacchi@alice.it



UNIVERSITÀ DEGLI STUDI DI GENOVA

FACOLTÀ DI INGEGNERIA

Tesi di Laurea Specialistica
in

INGEGNERIA MECCANICA

Analysis and control of thermoacoustic instabilities in gas turbine systems

Relatore
Chiar.mo Prof. Alessandro Bottaro

Candidato
Matteo Bargiacchi

Correlatore
Dott. Giulio Mori

Anno Accademico 2009/2010

DICAT

Riassunto

Le normative ambientali degli ultimi anni hanno spostato i limiti sulle emissioni inquinanti verso valori sempre più stringenti. Basse emissioni di ossidi di azoto possono essere ottenute mediante una combustione premiscelata povera. Sfortunatamente queste sono proprio le condizioni ideali per cui si possono instaurare instabilità termoacustiche che portano ad una combustione inefficiente generando vibrazioni così intense da mettere in serio pericolo la resistenza strutturale della macchina. Comprendere la natura di questi fenomeni è molto importante ed è attualmente uno dei maggiori argomenti di studio riguardo allo sviluppo di turbine heavy-duty e aeronautiche. In questa tesi è stato sviluppato e implementato un modello lineare a parametri concentrati chiamato LOMTI in grado di fare luce sui parametri che guidano questi processi fisici. In modo da rendere i risultati sufficientemente affidabili è stata portata a termine una calibrazione della geometria basata su simulazioni 3D con modelli FEM.

Introduzione. L’humming è un fenomeno caratterizzato da fluttuazioni di rilascio termico che generano onde di pressione e quindi vibrazioni. Queste onde, viaggiando in direzione circonferenziale in una camera di combustione anulare o riflettendosi sulle sue pareti, ritornano ad influenzare la zona di fiamma innescando un processo di retroazione. Diversi criteri sono già stati proposti in letteratura già nel XIX secolo, primo fra tutti il criterio di Rayleigh; purtroppo, anche se formalmente corretti nell’ambito delle loro ipotesi, essi non sono di facile implementazione a causa della loro natura integrale. Un modello ispirato alla moderna teoria del controllo dei sistemi è stato sviluppato nell’ambito di un progetto di collaborazione fra il DICAT e Ansaldo Energia. Questo codice implementato in MATLAB prende il nome di LOMTI (Low Order Model for Thermoacoustic Instabilities). Il LOMTI è un modello a parametri concentrati lineare che rappresenta una configurazione reale della camera di combustione di un turbogas come una successione di condotti interconnessi.

Il modello matematico. I gradi di libertà del sistema sono il minor numero di variabili di stato interne x_i in grado di rappresentarlo univocamente a tempo fissato. La camera di combustione del turbogas è analizzata mediante un set di equazioni rappresentative del sistema contenenti solo le variabili x_i che dà luogo all’espressione:

$$[\mathbf{M}] \cdot \mathbf{x} = \mathbf{0} \tag{1}$$

dove $[\mathbf{M}]$ è la matrice quadrata dei coefficienti di \mathbf{x} .

In accordo con l'approccio a parametri concentrati si ipotizza un flusso medio dalle caratteristiche costanti in ogni condotto (plenum, 24 premixers e camera di combustione). Quindi ogni grandezza $G(x, r, \theta, t)$ viene scomposta in una parte costante \bar{G} (diversa per ogni condotto) e in una parte fluttuante $G'(x, r, \theta, t) \ll \bar{G}$.

La parte variabile rappresenta le perturbazioni del flusso medio. Queste possono essere ricavate dalla teoria acustica elementare per il caso più generale di condotto anulare a spessore finito tenendo conto anche delle onde di entropia che si generano a valle della fiamma.

La matrice dei coefficienti $[\mathbf{M}]$ è funzione della sola variabile $\omega = \omega_r + i\omega_i$. Il sistema ammette soluzione non banale solo se $\det([\mathbf{M}]) = 0$. Quindi il cuore numerico del LOMTI risiede nel calcolo dei valori complessi di ω che annullano il determinante. Una volta ottenuti questi valori ω_r , rappresenterà la frequenza di oscillazione di un modo [Hz] e ω_i il suo tasso di crescita [s^{-1}].

Calibrazione della geometria. Le dimensioni del modello a parametri concentrati, ossia lunghezza, raggio medio e spessore di ogni condotto, non sono immediate da ricavare una volta che si ha a disposizione la geometria reale. Essi non sono quindi valori geometrici veri e propri ma delle dimensioni acustiche equivalenti. Per calibrare questi valori ci si avvale di simulazioni tridimensionali ottenute con il software ad elementi finiti COMSOL Multiphysics. Per dare valore ai risultati tutte le condizioni al contorno e operative come la portata massica di esercizio sono state fatte coincidere.

In modo da padroneggiare gli effetti della variazione della geometria sono stati fatti 8 studi preliminari, uno per ogni parametro geometrico in gioco. Una volta noti gli effetti si è stati in grado di far coincidere i modi ottenuti in LOMTI con quelli di COMSOL analizzando le autofunzioni risultanti.

Altre simulazioni COMSOL con le perturbazioni di fiamma attive sono state utilizzate per ottenere ulteriori informazioni. Mentre nella fase senza fiamma attiva gli unici valori importanti sono le frequenze di oscillazione, in questo caso hanno rilevanza anche i tassi di crescita. Il fatto che ci sia una fiamma attiva implica che la funzione di trasferimento della fiamma che modella il rilascio termico sia del tipo:

$$\frac{Q'}{Q} = \kappa \frac{u'}{\bar{u}} e^{-i\omega\tau} \quad (2)$$

dove κ e τ assumono valori non nulli. Il valore di κ rappresenta quanto la fiamma è sensibile alle fluttuazioni di una certa quantità. Il valore di τ rappresenta invece il ritardo con cui tale quantità influenza il rilascio termico.

Studi parametrici Una volta che la geometria è fissata è possibile portare a termine degli studi parametrici su diverse quantità di interesse accademico e progettuale. Per esempio le dimensioni della camera di combustione sono state fatte variare in modo da comprenderne gli effetti sulla stabilità. Altri studi sono stati sviluppati in modo da comprendere l'effetto dei parametri $\kappa-\tau$ e l'influenza dell'approssimazione $c_P, c_V = cost$.

Funzione di trasferimento della fiamma. In definitiva, sia da studi pregressi che dagli ultimi studi parametrici, è ormai lampante la criticità del modello di fiamma. Quindi si è cercato di sviluppare una nuova funzione di trasferimento della fiamma basandosi su principi assodati. Partendo dall'equazione:

$$Q = \frac{\dot{m}_F H_i}{A}, \quad (3)$$

e applicando la legge di Dalton delle pressioni parziali si ottiene, dopo aver linearizzato:

$$\frac{Q'}{\bar{Q}} = \frac{\rho'_{flame}}{\bar{\rho}_3} + \frac{u'_{flame}}{\bar{u}_3} - \frac{\bar{\alpha} + \chi}{\bar{\alpha} + 1} \cdot \frac{p'_{inj}}{\bar{p}_2} e^{-i\omega\tau}, \quad (4)$$

dove α è il rapporto aria/combustibile, χ il rapporto fra i pesi molecolari di aria e combustibile e τ il tempo che impiega una particella ideale a percorrere il tratto iniezione-fiamma.

Da questa espressione si evince come le variabili che intervengono nell'oscillazione di rilascio termico sono sostanzialmente la perturbazione di portata massica in corrispondenza della fiamma e le oscillazioni di pressione in corrispondenza degli iniettori di combustibile le quali influenzano il rapporto di equivalenza della miscela. Anche con questo modello modificato per le funzioni di trasferimento sono stati ottenuti risultati incoraggianti.

Abstract

Low level of pollutants can be achieved by a lean and premixed burning. Unfortunately these are just the conditions that cause the unwelcome phenomenon of self-excited oscillations that yield inefficient burning and promote structural stresses so intense that can lead to engine and combustor failure. Understanding these phenomena is an important goal and it is of current interest to designers and theoreticians. A linear lumped model was created and implemented in order to achieve awareness of the effects of leading parameters of the physical process. Just to render results reliable a calibration has been carried out on the basis of three-dimensional finite element simulations. Finally a new transfer function model has been developed and tested.

Acknowledgments

I would like to express my gratitude to the Flubio research group, especially my supervisor Alessandro Bottaro. He has helped me throughout the entire development of this thesis, providing me with information, wisdom and friendship. Thinking about my future career I would not imagine something that will not be influenced by these years. I am also greatly indebted to Ezio Cosatto who has suffered from my continuous requests for explanations for a long time (let's not forget the previous thesis!). Special thanks are obviously reserved to Anaïs Guaus who has followed all my technical and numerical affairs with admirable endurance. Finally, I want to thank Giulio Mori and Ansaldo Energia to have initiated and supported my work in these years.

E ora passiamo a noi. Ovviamente voglio ringraziare papà e mamma per tutto il sostegno morale e finanziario di tutti questi anni a partire dalle tabelline ripetute alla morte e dalla colazione sempre pronta, così come i nonni dai quali, senza bisogno di molte parole, ho imparato le cose più importanti. Poi ringrazio Fra, Albi, Ale (tutti perchè si e basta, non servono spiegazioni), Edo (a cui rispondo alla domanda posta in [35]: NO!!), Gamba (per le fantastiche ed interminabili discussioni sui massimi sistemi...), Gian (per tutto!), Bèrto (sperando che non si arrabbi...), Cin, Filippino, Flavia, Giulia, Lorenza, Michela, Sara, Matteo R., Matteo M., Andrea, Gianni, insieme a tutti quelli di 'Al Solito Posto' (per tutto il resto, vi prego non fatemi trovare una motivazione per ognuno!) e tanti altri amici che sono stati importanti negli anni anche per piccole cose. E infine, ebbene no, non me ne sono dimenticato, ringrazio Tiziana per quando, tutte le volte che le ho detto devo studiare, mi ha sopportato, e anche per tutte le volte che non lo ha fatto! Uh a proposito, Gaspare...

Nomenclature

- A area [m^2]
- B sum of Bessel functions (first and second kind)
- c_s speed of sound [ms^{-1}]
- c_p, c_v specific heats [$KJKg^{-1}K^{-1}$]
- D molecular diffusivity [m^2s^{-1}]
- $Da = (l_0/\delta_L)(S_L/u'_{rms})$ Damköhler number
- f frequency [Hz]
- g gravity acceleration [ms^{-2}]
- GR growth rate [s^{-1}]
- H enthalpy [$KJKg^{-1}$]
- H_i lower heat of combustion [$KJKg^{-1}$]
- $H_n = \omega L/c_s$ Helmholtz number
- i imaginary unit
- k_{\pm}, k_0 axial wave number [m^{-1}]
- l_k Kolmogorov turbulence scale [m]
- l_0 integral turbulence scale [m]
- $Le = \alpha_T/D$ Lewis number
- \dot{m} mass flow rate [Kgs^{-1}]
- $M = u/c_s$ Mach number
- m radial wave number []
- n azimuthal wave number []
- p pressure [Pa]

-
- ppm part per million []
 - PM molecular mass [$Kgmol^{-1}$]
 - q heat release per unit of volume [Wm^{-3}]
 - Q heat release per unit of area [Wm^{-2}]
 - r radial coordinate [m]
 - R perfect gas constant for air [$KJKg^{-1}K^{-1}$]
 - $Re_{l_0} = u'_{rms}l_0/\nu$ turbulence Reynolds number
 - \mathfrak{R}_u universal perfect gas constant [$KJKg^{-1}mol^{-1}$]
 - S entropy [$KJKg^{-1}K^{-1}$]
 - $Sc = \nu/D$ Schmidt number
 - S_L laminar flame velocity [ms^{-1}]
 - S_T turbulent flame velocity [ms^{-1}]
 - t time [s]
 - T temperature [K]
 - T_p period [s]
 - u axial velocity [ms^{-1}]
 - \mathbf{v} velocity [ms^{-1}]
 - v radial velocity [ms^{-1}]
 - V volume [m^3]
 - w azimuthal velocity [ms^{-1}]
 - x axial coordinate [m]
 - \mathbf{x} general spatial coordinate [m]
 - y_i mass fraction

Greek

- α_T thermal diffusivity [m^2s^{-1}]
 - α air/fuel ratio []
 - β_i fraction of combustor associated with burner i
 - γ specific heat ratio []
-

-
- δ_L flame thickness [m]
 - θ azimuthal coordinate [rad]
 - κ sensitivity of the flame transfer function []
 - λ wavelength [m]
 - λ_T thermal conductivity [$Wm^{-1}K^{-1}$]
 - ν kinematic viscosity [m^2s^{-1}]
 - ρ density [Kgm^{-3}]
 - τ time lag [s]
 - τ_v viscous stress [Pa]
 - φ phase [rad]
 - Φ equivalence ratio []
 - ϕ viscous heating [Wm^{-3}]
 - χ molar fraction []
 - ω angular frequency [$rads^{-1}$]

Superscripts

- $(..)'$ fluctuating quantities
- $(\bar{..})$ mean quantities

Subscripts

- $(..)_{0}$ total quantities
- $(..)_{1}$ plenum
- $(..)_{2}$ premixers
- $(..)_{3}$ combustion chamber

Preface

The work in this thesis was entirely conducted at the University of Genoa (DICAT) between January 2010 and November 2010 under the supervision of Professor Alessandro Bottaro. This work is the natural continuation of the previous three-year thesis. The whole activity was part of a wider project consisting in a collaboration between DICAT and Ansaldo Energia for the development of a numerical tool able to predict thermoacoustic instabilities, and oriented to the design of a new LP gas turbine. This cooperation involves the University of Bari (PoliBa) and the Centre Européen de Recherche et de Formation Avancée en Calcul Scientifique in Toulouse (CERFACS). The former group, thank to a commercial simulation software environment, COMSOL Multiphysics, has performed three dimensional simulations that are the basis for the calibration of chapter 5. The latter team is developing a complex three dimensional acoustic tool (AVSP) and has performed LES simulations on the flame dynamics useful to obtain characteristic flame parameters.

The whole code is the ultimate development of several subsequent refinements of a very simple code implemented for the first time in 2008. Even if I wrote part of this earlier code, in these years the actual development has been carried out by Julien Favier and Anaïs Guaus, together with Ezio Cosatto. The final code implemented in the MATLAB environment is called LOMTI, that means Low Order Model for the study of Thermoacoustic Instabilities. In addition to several parametric studies my contribution was directed to connect the real geometry to the lumped approach of LOMTI. Furthermore I have shown the advantages of a non constant specific heats model calculating their effective values for each mixture evolving in the gas turbine taken into account. Finally I proposed a new transfer function based on well known thermodynamic principles.

Part of this work has been submitted to the ASME Turbo Expo 2011 conference with the title 'A Quantitative comparison between a low order model and a 3D FEM codes for the study of thermoacoustic combustion instabilities', GT 2011-45969.

Contents

1	Introduction	1
2	A brief literature review	3
2.1	The humming phenomenon	3
2.2	General criteria	4
2.2.1	Rayleigh criterion	4
2.2.2	Recently developed criteria	8
2.3	Flame dynamics	11
2.3.1	Flame transfer functions	13
3	Starting point	19
3.1	Increasing complexity	19
4	The governing equations	25
4.1	No mean flow and heat release	26
4.2	Adding mean flow and heat release	27
4.3	Coupling between perturbations	31
4.4	Equations for the mean flow computation	33
4.4.1	Perfect gas equations	33
4.4.2	Mass flux conservation equations	34
4.4.3	Energy conservation equations	34
4.4.4	Isentropic/grid conditions	34
4.4.5	Borda equations	35
4.5	Perturbations equations	35
4.5.1	Mass flux conservation equations	35
4.5.2	Energy conservation equations	36
4.5.3	Isentropic conditions	36
4.5.4	Borda equations	36
4.5.5	Inlet and outlet conditions	37
4.5.6	Flame transfer function	37
4.6	Flame model	37
5	Calibration on a FEM code	41
5.1	Influence of the plenum geometry	43
5.2	Influence of the premixers geometry	45
5.3	Influence of the combustion chamber geometry	46
5.4	Calibration of the geometry	47

5.5	Mode shape analysis	48
5.6	Comparison with flame perturbations	58
6	Parametric studies	63
6.1	Combustion chamber size	64
6.2	Flame parameter τ	65
6.3	Flame parameter κ	70
6.4	Transfer function's reference point	71
6.5	Influence of the transfer functions	72
7	Annular ducts with non-negligible thickness	81
8	Proposal for a new transfer function	87
8.1	Deducing the expression	87
8.2	Results for the turbine configuration	92
9	Conclusions and future developments	95
9.1	Conclusions	95
9.2	Future developments	96
9.2.1	Further development of the FTF	96
9.2.2	Computational time	97
9.2.3	Passive controls	97
A	Combustion processes and related emissions	99
B	The function determinant	103
C	Specific heat ratio dependency	107
D	LOMTI user guide	115
	Bibliography	125

Chapter 1

Introduction

The production of massive amounts of energy required by wealthy developed countries necessarily leads to the use of more efficient and more environmentally friendly power plants. In fact, in thermoelectric plants combustion is achieved burning solid, liquid and gaseous fuels which necessarily leads to the formation of substances that can interact negatively with the environment endangering public health. Nowadays combined gas turbine plants are the best perspective to supply rising demand for energy. Combined cycle plants are able to ensure a very high efficiency (55% to 65%) allowing a lower environmental impact than usual thermal power plants. In such a plant, emissions consist in Carbon Monoxide (CO) and Nitrogen Oxides (NO_X , primarily NO). Other pollutants, such as Sulfur Dioxide (SO_2) and particulate matter (PM) are practically negligible due to the low concentration of sulfur in fuels suitable for gas turbine systems and the high burning efficiency. As a matter of fact no restriction on particulate matter emission is contemplated in nowadays regulations. CO emissions are less critical than NO_X ones despite their overall amount (approximately 50 and 30 ppm). Research in reducing NO_X emissions have led to a complete redesign of combustion systems: at this time the rising technology is Lean Premix (Prevaporized) Combustion that is going to replace usual diffusion flame. Such a process allows to have combustion with a lower mean temperature that inhibits thermal NO_X formation and yields SCR (Selective Catalytic Reduction) systems to be even detrimental as far as overall pollution levels are concerned. Unfortunately these plants are strongly susceptible to thermoacoustic instabilities with unstable strong vibrations that can damage the machinery and limit its operating conditions. Since LP and LPP combustion is actually the best way to reduce dangerous pollutants, thermoacoustic instabilities have become one of the major topics of research in the design of gas turbines combustors. In LP (gaseous fuel) and LPP (liquid fuel requesting also vaporization) plants, air and fuel are mixed before entering the combustion chamber where ignition, flame anchoring and safety are provided by a pilot diffusion flame. If the relationship between the phases of minimal perturbations in acoustic field and thermal power meets certain criteria, these perturbations may self-excite, growing in size and causing potentially dangerous vibrations.

Chapter 2

A brief literature review

2.1 The humming phenomenon

Humming is a phenomenon characterized by fluctuations of heat release that cause pressure waves. These waves reflected on the walls of the chamber, or travelling in the azimuthal direction, return to influence the flame in a feedback process. This phenomenon seems to occur primarily due to the alteration of the stoichiometric ratio in the flow field, i.e. the equivalence ratio. This disturbance causes an irregular heat release generating a closed cycle.

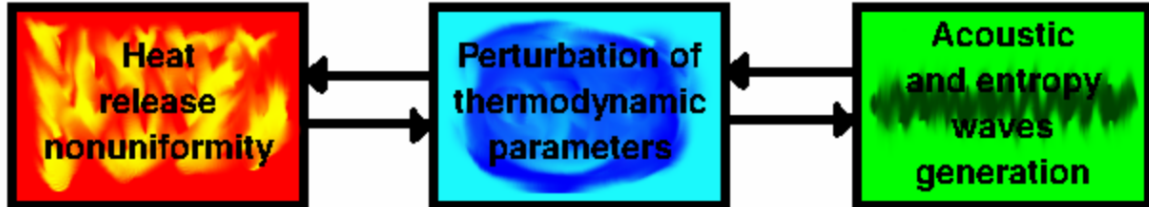


Figure 2.1 - *Feedback process*

Depending on many parameters, both fluid dynamical and geometrical, these disturbances can be unstable or not. The goal of nowadays activities is to create a tool able to predict the possibility of a gas turbine to generate unstable modes of oscillation without calculating the entire flow field. In order to achieve this purpose a lumped parameters linear approach is useful. This is the so called LOMTI (Low Order Model for Thermoacoustic Instabilities). The influence of this choice will be discussed later, but it is important to highlight that, with this approach, we can only predict whether a mode of oscillation is stable or not. No information is provided on the amplitude of these oscillations; only a non-linear approach can predict them. So an unstable mode with small growth rate is, a priori, as dangerous as another one with much larger growth rate even though it is conceivable that the last one is more likely to be predominant. However there is practically a unique interesting development for both modes: a limit cycle caused by the energy exchange between modes, arising from a balance between the resonant forcing of the mode and damping phenomena. We want to avoid this op-

erating condition because it generates fatigue and a stress cycle on the plant limiting its potential. In fact it is known how much a gas turbine is susceptible to working under conditions of partial load in terms of efficiency. There is also another borderline development: a continuous increase of the oscillations causing the immediate failure of some component due to the static stress. Needless to say, also this case is to be avoided.

Several criteria are present in the literature but none can easily predict whether the instability ensues or not. This is because they are generic relationship based on integral inequalities.¹ Even if they correspond loosely with experimental observations it is necessary to calculate the entire flow field, a task much beyond the goal of the present research. They are useful to try to understand the physical problem at its origin nonetheless.

2.2 General criteria

2.2.1 Rayleigh criterion

Thermoacoustic instabilities were observed by Higgins [2] in 1777 simply by realizing that a flame in a tube could generate sound (and thus vibrations). Subsequently in 1850 Rijke studied the "Higgins singing flame" creating a self excited process inserting a grid that releases heat in an open ended duct [8].

For certain ranges of position of the heat source within the tube, the Rijke tube emits a loud sound. Rijke's original interest in the phenomenon appears to have been from the point of view of musical acoustics. He first experimented with a vertical tube which had a piece of fine metallic gauze stretched across it in the lower part of the tube. The gauze was heated until red hot by a flame, which was then withdrawn. The tube then emitted an audible sound for a few seconds. When the gauze was heated electrically instead of using a flame, Rijke found that the tube could be made to sound continuously. However, the response of the tube did not satisfy Rijke's requirement for musical acoustics.



Figure 2.2 - Rijke tube.

Following this, the Rijke tube remained merely an object of curiosity for nearly a century, until the emergence of jet and rocket propulsion. Combustion in jet and rocket engines involves very high power densities of the order of the GW/m^3 . A very small fraction of this energy is more than adequate to excite and sustain acoustic waves inside the combustion chamber or afterburners. These acoustic waves result in a loud,

¹Discussed further in section 2.2

annoying sound (called screech, buzz, humming, etc.) and can also cause structural damage to the combustion chamber. The need to control thermo-acoustic phenomena in jet afterburner and gas turbine combustion chambers led to renewed interest in Rijke tube thermoacoustics. Today, the Rijke tube serves as a convenient prototypical system for the study of thermo-acoustic phenomena. Since its rebirth, Rijke phenomenon has therefore been widely discussed and reviewed in the literature.

A first explanation of the phenomenon was given by Rijke himself. According to him, the resulting variation in pressure was such that fluid elements in the lower half of the tube always experienced expansion, while those in the upper part of the tube underwent compression. The weakness of this argument is evident since it does not explain why sound is generated. The role of the energy source in a sounding Rijke tube is not merely to excite acoustic waves in the tube but also to build up and sustain the already excited acoustic waves. In other words sound must be generated by the setting up of standing waves.²

By the end of XIX century, Lord Rayleigh had formulated a criterion to explain how acoustic waves could be excited and sustained by heat addition. Rayleigh's criterion (in Lord Rayleigh's words) can be stated as follows:

"If heat be communicated to, and abstracted from, a mass of air vibrating (for example) in a cylinder bounded by a piston, the effect produced will depend upon the phase of the vibration at which the transfer of heat takes place. If heat be given to the air at the moment of greatest condensation, or be taken from it at the moment of greatest rarefaction, the vibration is encouraged. On the other hand, if heat be given at the moment of greatest rarefaction, or abstracted at the moment of greatest condensation, the vibration is discouraged."

This criterion does not seem to satisfactorily explain the sounding of the Rijke tube. When a Rijke tube sounds, a stationary acoustic wave is set up in the tube and every fluid element experiences alternate compression and expansion during each cycle. Thus, it appears that the heat source, irrespective of its location, must drive the acoustic waves during the compression half of each cycle but damp them out during the expansion half cycle. Summing over a full cycle, the heat source appears to neither drive nor damp the acoustic waves, i.e., the heat source does not seem to sustain the acoustic waves. However, we shall show below that the above argument does not correctly interpret Rayleigh's criterion for the sounding of the Rijke tube.

To really understand this statement it is useful to perform a decomposition of each quantity: $G(t) = \bar{G} + G'(t)$ where $G' \ll \bar{G}$. In fact Rayleigh's criterion talk about *giving or taking heat*, that means $q' > 0$ or $q' < 0$ (\bar{q} is always positive). Now Rayleigh's criterion could be written in mathematical terms as follows:

²Consider two opposite sinusoidal travelling waves with the same amplitude: $A = a \cdot \sin(\omega t - kx)$; $B = a \cdot \sin(\omega t + kx)$. Using trigonometrical expression: $A + B = 2a \cdot \sin(\omega t) \cdot \cos(kx)$ the resulting standing wave is composed by a time independent term modulated by $\sin(\omega t)$. Indeed, standing waves do not carry a net flux of energy: they 'stand' with fixed nodes in space and time at $kx = \pi/2 + n\pi$

$$\int_{\Omega} \int_0^{T_P} p'(\mathbf{x}, t) \cdot q'(\mathbf{x}, t) dt dV > 0 \quad (2.1)$$

where

- Ω is the domain in analysis,
- T_P is the period of excitable harmonics,
- p' is the perturbation of the pressure field,
- q' is the perturbation of heat release rate.

If viscous dissipation is taken into account, equation (2.1) becomes:

$$\int_{\Omega} \int_0^{T_P} p'(\mathbf{x}, t) \cdot q'(\mathbf{x}, t) dt dV > \int_{\Omega} \int_0^{T_P} \phi(\mathbf{x}, t) dt dV \quad (2.2)$$

where ϕ is the local viscous heating term.

Just to understand the phenomenon let us forget the dissipation term $\phi(\mathbf{x}, t)$ in equation (2.2) applying the first ideal inequality to Rijke tube configuration. Considering p' and q' as sinusoidal waves of period $T_P = 1s$ differing by a phase φ_{pq} only, we can argue that Rayleigh's criterion is satisfied when $|\varphi_{pq}| < \pi/2$. Let us analyze a few interesting cases:

- $\varphi_{pq} = 0$: amplification is maximum because p' is completely superimposed to q' thus $q' \cdot p' > 0 \forall x$.
- $\varphi_{pq} = \pi/4$: amplification is zero because for half a cycle heat is given for $q' \cdot p' < 0$ and for the other half $q' \cdot p' > 0$. See figure 2.3.
- $\varphi_{pq} = \pi/2$: amplification is negative because $q' \cdot p' < 0 \forall x$, thus waves are always damped. See figure 2.4.
- $\varphi_{pq} = 3\pi/4$: it is practically the same case as $\varphi_{pq} = \pi/4$.

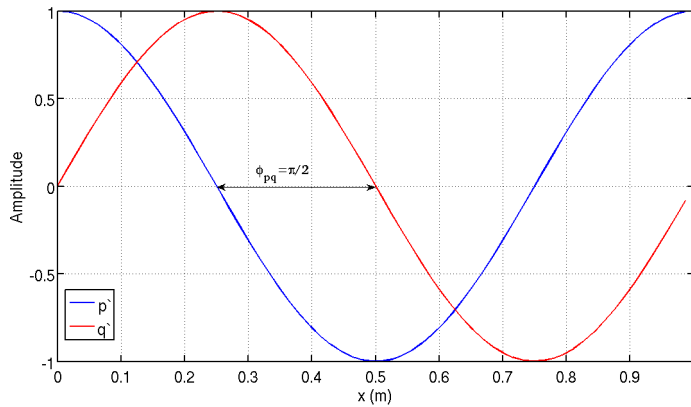


Figure 2.3 - $p'(x)$ and $q'(x)$ with $\varphi = \pi/2$

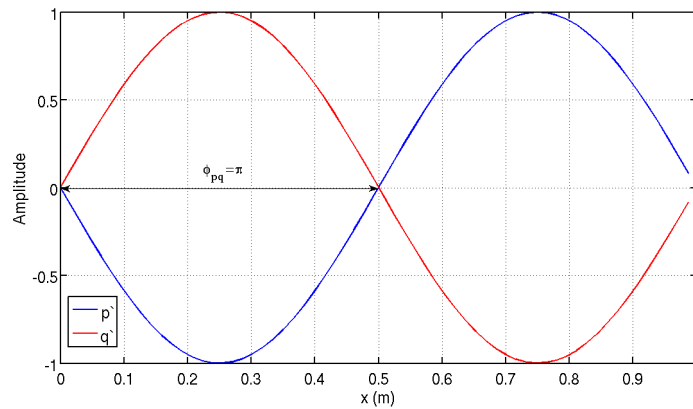


Figure 2.4 - $p'(x)$ and $q'(x)$ with $\varphi = \pi$

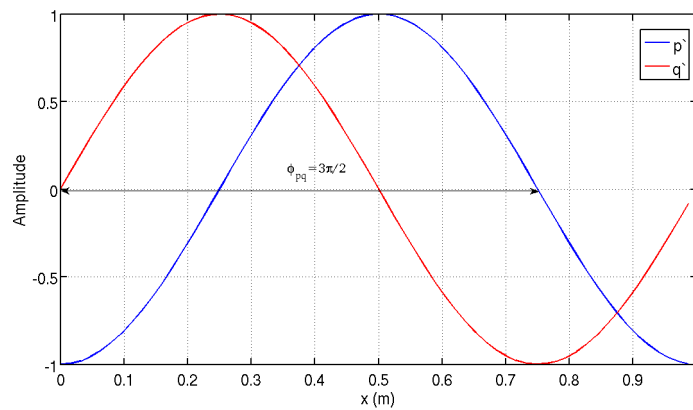
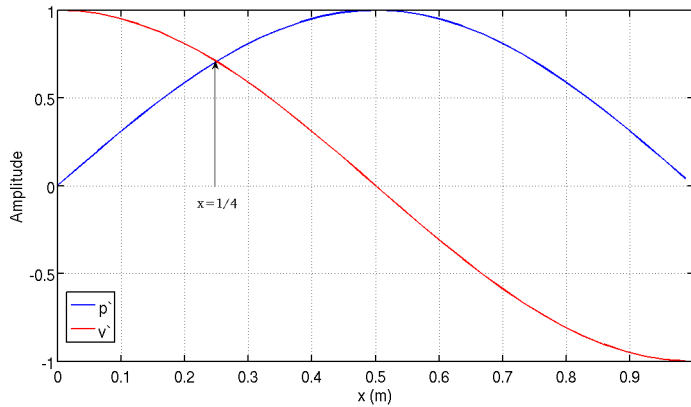


Figure 2.5 - $p'(x)$ and $q'(x)$ with $\varphi = 3\pi/2$

Now it is interesting to determine where heat source must be located to generate instabilities. As in [8] we can describe all quantities in a phasor diagram. Integrating the one dimensional Euler equation, where u is derived according to phasors' rule, we infer that u' follows p' with a quarter period lag (quadrature), i.e. u' is zero when p' is maximum (or minimum).

$$\begin{aligned}
 u &= Ae^{i\omega t} \\
 \frac{du}{dt} &= -\frac{1}{\rho} \frac{dp}{dx} \\
 i\omega u &= -\frac{1}{\rho} \frac{dp}{dx} \\
 u &= \frac{i}{\rho\omega} \frac{dp}{dx}
 \end{aligned}$$


 Figure 2.6 - $p'(x)$ and $u'(x)$

With analogous steps we get a similar expression combining energy equation and Gibbs relationship.

$$\rho T \frac{DS}{Dt} = \dot{q} \qquad T dS = c_p dT - \frac{dp}{\rho}$$

Gathering all these relations we can infer that if a heat source is located at a quarter of the duct, the product $p' \cdot q'$ is always positive, thus instabilities are encouraged. If heat is located at one end or in the middle of the tube Rayleigh's integral (2.1) is zero and no amplification arises. Finally if a heat source is located in the upper half of the duct Rayleigh's integral is negative and perturbations are damped.

Finally another aspect must be taken into account: mean flow. In fact if $u(t) = \bar{u} + u'(t)$ and $\bar{u} = 0$ fluid particles stand near the flame and after a few cycles they reach the same temperature of the flame inhibiting unsteadiness needed for the onset for thermoacoustic instabilities. Thus, for a Rijke tube to "sing", the heat source must be able to create a mean flow, and the fluctuations in heat transfer due to the acoustic waves must be in phase (or at least not too far from being in phase) with the acoustic pressure. The mean heat transfer to the fluid in the duct over a cycle is still \bar{q} , but additional heat is given to the fluid when it is undergoing compression, which is then recovered from the fluid during the expansion half cycle.

2.2.2 Recently developed criteria

Recent studies [9] have shown that Rayleigh's integral $\int_{\Omega} \int_0^T p'(\mathbf{x}, t) \cdot q'(\mathbf{x}, t) dt dV$ focusses just on one of the terms appearing in the acoustic energy equation. Considering all terms in the momentum equation we have:

$$\rho \frac{D\mathbf{v}}{Dt} = -\nabla p + \nabla \cdot \tau_{\mathbf{v}}. \qquad (2.3)$$

Performing the dot product of (2.3) with \mathbf{v} we get the energy equation. Introducing the sensible energy equation

$$\rho \frac{De_s}{Dt} = -p \nabla \cdot \mathbf{v} + q + \nabla \cdot (\lambda_T \nabla T) + \tau_{\mathbf{v}} : \nabla \mathbf{v}, \quad (2.4)$$

together with the continuity equation and $\rho e_s = p/(\gamma - 1)$, we get an exact non linear equation:

$$\rho \frac{D\mathbf{v}^2/2}{Dt} + \frac{1}{\rho c^2} \frac{Dp^2/2}{Dt} + \nabla \cdot (p\mathbf{v}) = \frac{\gamma - 1}{\gamma} (q + \nabla \cdot (\lambda_T \nabla T) + \tau : \nabla \mathbf{v}) + \mathbf{v} \cdot (\nabla \cdot \tau_{\mathbf{v}}) \quad (2.5)$$

Equation (2.5) can be linearized by considering small fluctuations according to a classical decomposition superimposed to a zero Mach number mean flow. These assumptions lead to a new criterion on an arbitrary domain Ω confined by a closed surface Σ :

$$\int_{\Omega} \frac{\gamma - 1}{\gamma \bar{p}} p' q' dV > \int_{\Sigma} p' \mathbf{v}' \cdot d\mathbf{A}. \quad (2.6)$$

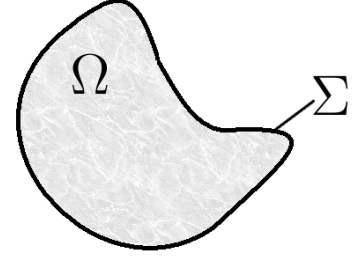


Figure 2.7 - Generic domain for the modified Rayleigh criterion.

Equation (2.6) means that the usual Rayleigh's integral must be greater than the net flux of acoustic energy across the surface Σ for instabilities to arise.³ Such a criterion becomes useful only with advanced LES analysis able to predict these losses.

Nevertheless there is no evidence that e_s in equation (2.4) is the relevant energy that must be taken into account. It is possible to show that such a definition loses consistency in a non-isentropic flow field. This means that another quantity should be used in the case of reacting flows to characterize the global amount of fluctuations properly and that this energy should include entropy fluctuations. Moreover, the entropy field is not constant over space when combustion occurs rendering equation (2.4) inconsistent.

This assumption leads to a new definition of the relevant energy, a so called fluctuation energy:

$$\frac{\partial e_{tot}}{\partial t} + \nabla \cdot (p' \mathbf{v}') = \frac{T'}{\bar{T}} [q' + \nabla \cdot (\lambda_T \nabla T)] - \frac{\bar{p}}{Rc_p} s' \mathbf{v}' \cdot \nabla \bar{s} + \mathbf{v}' \cdot (\nabla \cdot \tau'_{\mathbf{v}}) \quad (2.7)$$

where e_{tot} is defined as

$$e_{tot} = \bar{\rho} \frac{\mathbf{v}' \cdot \mathbf{v}'}{2} + \frac{p'^2}{2\bar{\rho}c^2} + \frac{S'^2 \bar{p}}{2Rc_p} \quad (2.8)$$

³The flux term in equation (2.6) is completely different from the r.h.s. of equation (2.2) which includes only viscous losses.

Note that the fact that entropy is included does not mean that entropy fluctuations are added to the analysis since the zero Mach number approximation removes entropy waves that cannot propagate without a non zero mean flow. Nevertheless a non-isentropic steady flow field ($\omega = 0$) could be taken into account.

Integrating over the domain equation (2.7) we get the extended Rayleigh like criterion:

$$\int_{\Omega} \left(\frac{T'q'}{\bar{T}} - \frac{\bar{p}}{Rc_p} S' \mathbf{v}' \cdot \nabla \bar{S} \right) dV > \int_{\Sigma} p' \mathbf{v}' \cdot d\mathbf{A}. \quad (2.9)$$

What reported so far might appear as a useless complication without an order of magnitude estimate of the different terms. It is possible to show that the additional term related to the non-uniform entropy field is potentially larger than the classical Rayleigh's term. This argument is supported by numerical results that yield values of entropy fluctuations often larger than acoustical ones. Several studies already present in the literature have developed purely acoustic models. Due to recent evidence we cannot trust these results when combustion occurs. Since the presence of entropy fluctuations requires a non-zero mean flow, the Mach number assumes a double importance considering that its general influence on stability has already been demonstrated [1] (see section 3.1).

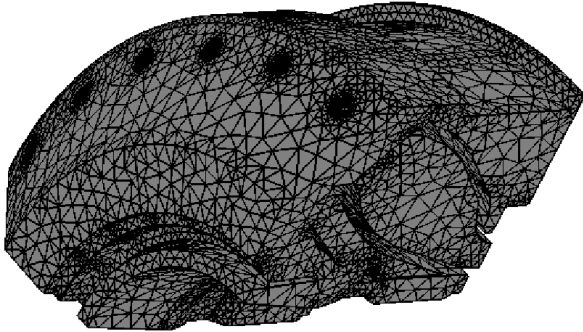


Figure 2.8 - *Discretization of a AE94.3A gas turbine combustor [24].*

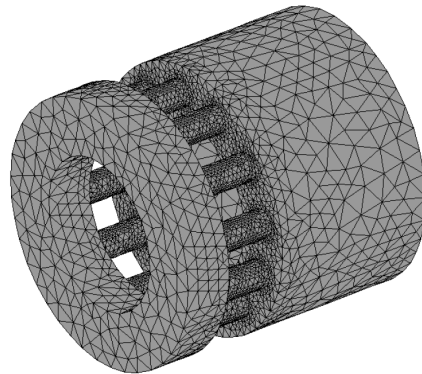


Figure 2.9 - *Discretization of a simple domain [14].*

In the present work no integral criterion is applied since it would required a spatial and temporal discretization of the whole domain, like in figure 2.8 or 2.9. The aim of the present research is to develop and validate a simple tool able to predict rapidly the influence of geometrical parameters on the onset of instabilities. In this model the geometry is defined by few parameters straightforwardly modifiable (only 10 effective values in the *AE94.3A* gas turbine model). It is trivial that a three dimensional approach would lead to large time for the setting of every simulation with different geometrical configuration since every geometry would require hours for generating the CAD and the adequate mesh. Our simulations, describe later, require only minutes of CPU time on a desktop computer.

2.3 Flame dynamics

An important step for a correct modelling and to be able to envisage passive or active control techniques to full-scale combustors is the development and analysis of low-order dynamical models that contain the fundamental physics of the system. It will be clear in chapter 4 that the core of the system is the flame model, in other words the equation that describe the interaction between the heat release and the perturbations. Theoretical and numerical techniques in non-linear dynamical systems theory have been developed in the research community over the past ten years and can be effectively applied to these reduced order models.

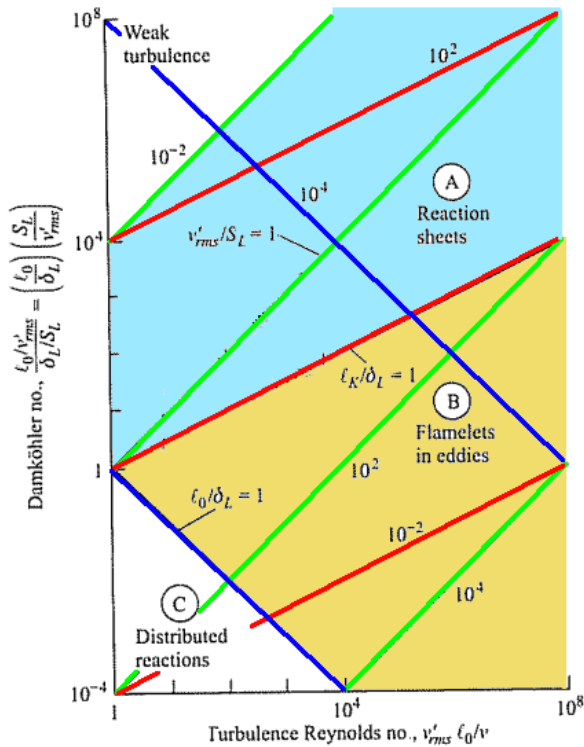


Figure 2.10 - Important parameters characterizing turbulent premixed combustion. Conditions satisfying the Williams-Klimov criterion for the existence of wrinkled flames lie above the red line ($l_k = \delta_L$), and conditions satisfying the Damköhler criterion for distributed reactions fall below the blue line ($l_0 = \delta_L$). Hypothesis: $Le = 1, Sc = 1 \Rightarrow \nu = 1$. Integral scale is dependent on the Kolmogorov one: $l_0 = l_k \cdot Re_{l_0}^{3/4}$.

The interaction between turbulence and combustion is to be investigated in order to achieve awareness on the dominating processes. Without going too deeply into the theoretical analysis, we distinguish three different kinds of interactions:

- Ⓐ reaction sheets
- Ⓑ flamelets in eddies
- Ⓒ distributed reactions

Distributed reactions occur when the turbulence integral scale l_0 is smaller than the scale relative to combustion forcing turbulence time to be larger than the chemical one. This fact implies that chemical kinetics is influenced by the features of the flow. Flamelets in eddies occur when $l_k < \delta_L < l_0$; in this case combustion may take place inside small enough vortical structures. Reaction sheets occur when the turbulence scale l_k is greater than the scale relative to combustion. Reactions develop in a range internal to the Kolmogorov scale, thus turbulence is able only to wrinkle the surface of the flame.

Combustion itself is not influenced but a new flame speed that takes into account turbulence is to be defined ($S_T = S_L + u'$ for example, with S_T and S_L the turbulent and laminar flame speed, and u' a fluctuating velocity). Distributed reactions are useless for engineering applications since they would require high flow velocities in small diameters (in order to get large u' and small l_0) generating unacceptable losses. Flamelets in eddies assume interest in few applications such as some four-stroke internal combustion engines. Gas turbine combustion fits in the reaction sheets due to the high Damköhler number together with reduced turbulence Reynolds numbers.

The significant influence of unsteady phenomena connected with turbulence interaction with flame fronts makes CFD simulations far from being trivial. It is very important to know the flame shape and its position since from this information we can deduce parameters that can be tuned in order to get a model able to describe properly the interactions between a flame and acoustic waves occurring in the combustion system. Simulations have already been performed with classical turbulence models based on the Reynolds-Averaged Navier Stokes Equations and LES simulations. Results were significantly different according to previous statements: it is clear that a model that cuts off the integral scale that would have an influence on the flame front is hardly suitable to predict in a reliable way the flame front itself. Furthermore LES simulations on such a complicated geometry with coupled combustion models require large computational time and resources.⁴

The heat release rate $[W]$ of a turbulent premixed flame may be expressed according to [23] as:

$$\rho_u A S_T H_i,$$

where

- ρ_u is the unburnt gas density,
- A is the flame surface area,
- S_T is the turbulent burning velocity or turbulent flame speed,
- H_i is the heat of reaction per unit mass.

The turbulent flame speed can be defined using dimensionless groups (Reynolds, Damköhler and Lewis numbers) and relating it to the laminar flame speed S_L :

$$\frac{S_T}{S_L} = f(Re, Da, Le, \dots).$$

⁴Combustion process can be preliminarily modelled as a double stage combustion process, as $CH_4 + \frac{3}{2}O_2 \rightarrow CO + 2H_2O$, followed by $CO + \frac{1}{2}O_2 \leftrightarrow CO_2$

2.3.1 Flame transfer functions

An operational transfer function is simply a mathematical model that relates a thermodynamic variable to another one. Considering an input signal $Ae^{i\omega t}$ and an output one $Be^{i\omega t + \tau}$ we define the transfer function as the ratio between output and input. Therefore B/A is the gain of the transfer function and τ is the phase angle. In this manner the time dependence is not needed in a feedback-loop analysis because all the equations have the same time dependence $e^{i\omega t}$.

A flame transfer function is needed in order to describe the flame-acoustic interaction. Three physical mechanism are to be identified:

1. flame front kinematics,
2. flame speed modifications,
3. equivalence ratio perturbations.

For turbulent premixed flames, the direct influence of pressure, temperature, and density variations on the heat release rate is usually considered to be negligibly small. In reality temperature and pressure could influence the laminar flame speed S_L .⁵ In this case the flame frequency response or flame transfer function, defined as the normalized ratio of heat release rate and velocity fluctuations, completely characterizes the dynamic response of a flame to acoustic perturbations.

$$F(\omega) = \frac{Q'/\bar{Q}}{u'/\bar{u}} \quad (2.10)$$

From equation (2.10) several simple criteria have been developed. The validation of such a model is in practice often difficult, because many parameters cannot be determined from first principles. Instead, parameters must be adjusted to match experimental or numerical data. In recent years, detailed laser diagnostic studies in gas turbine relevant combustors have contributed significantly to a better understanding of processes like flame stabilization, combustion instabilities, pollutant formation and finite-rate chemistry effects. Frequently used measuring techniques were particle image velocimetry (PIV) or laser Doppler velocimetry (LDV) for the flow field, laser induced fluorescence (LIF) for flame radicals (OH^- chemiluminescence in figure 2.11), tracers, pollutants or temperature, coherent anti-Stokes Raman scattering (CARS) for temperature, and laser Raman scattering for species concentrations. Numerical data which are often limited in scope as well as accuracy, such that significant uncertainties still remain. Despite these problems it is possible to get information above certain parameters just from global conservation laws in a quasi-steady limit[23], i.e. the state that any physically valid model reach when $\omega \rightarrow 0$.

⁵For hydrocarbons $S_L \propto T_i^{0.875} \cdot T_u^{0.5} \cdot T_b^{-0.875} \cdot e^{-E_a/(2RT_b)} p^{-0.125}$ where subscripts are respectively ignition, unburned and burned, see [37].

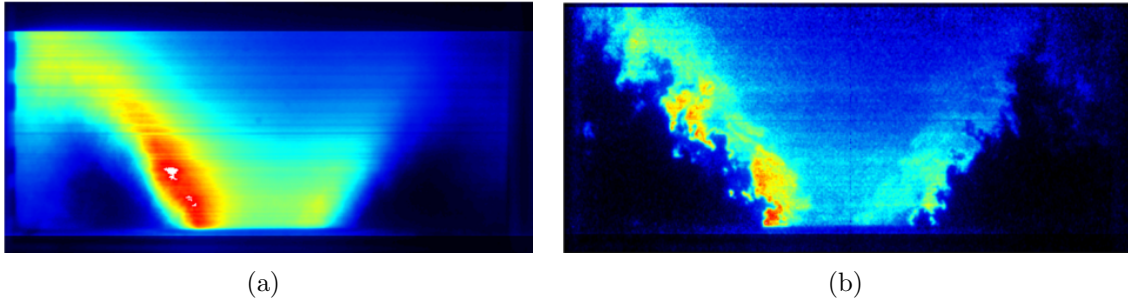


Figure 2.11 - Images of OH^- PLIF from oscillating flame [41].
 (a): mean OH distribution. (b): single shot measurement.

Let us consider a general flame transfer function that correlates heat release relative fluctuations Q'/\bar{Q} with the N quantities G_i that could have influence on it.

$$\frac{Q'}{\bar{Q}} = \kappa_1 \frac{G'_1}{\bar{G}_1} + \kappa_2 \frac{G'_2}{\bar{G}_2} + \cdots + \kappa_i \frac{G'_i}{\bar{G}_i} + \cdots + \kappa_N \frac{G'_N}{\bar{G}_N} \quad (2.11)$$

Then we are able to say that:

$$\lim_{\omega \rightarrow 0} \sum_{i=1}^N \kappa_i = K \quad (2.12)$$

where K satisfies the quasi-steady limit inferable from global conservation laws. This is useful to verify the validity of any transfer function. For example, assuming a stiff fuel injection $\dot{m}'_F = 0$, the heat release Q'_V [W] must be zero when $\omega \rightarrow 0$ because $Q_V = \dot{m}_F H_i$.

Difficulties in implementing such models are obvious since too many parameters are to be taken into account simultaneously, even if they are correlated by an equation (only one equation such as (2.12)). To overrun this problem several simplified models have been developed considering only the most pertinent quantities and disregarding all others.

Research on flame dynamics is made considering the influence of equivalence ratio on flame dynamics as in figure 2.12. Direct numerical simulation are performed to understand the interaction of acoustic waves with flame (figure 2.13). As stated previously the experimental analysis is extremely complicated since it is very difficult to get a good instrumentation of a critical flow field (temperatures are very high) and to get measurement of certain quantities like heat release fluctuations.

Therefore few empirical models remain. Let us list some of them from the simplest to the more elaborated:

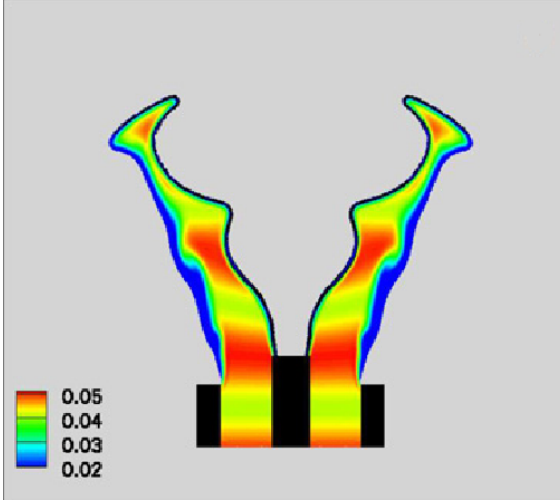


Figure 2.12 - Perturbed equivalence ratio distribution in a "V" flame [22].

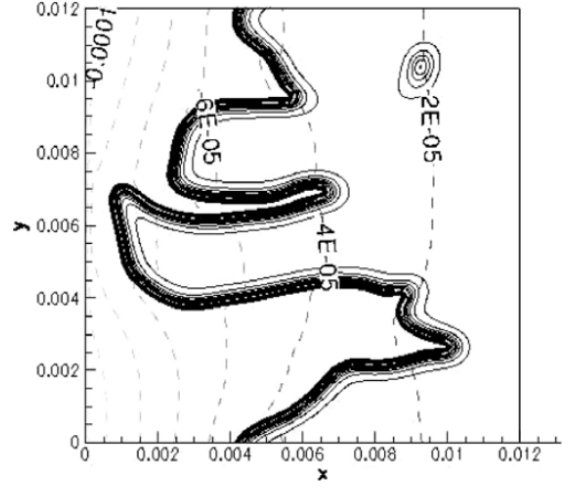


Figure 2.13 - Acoustically-induced pressure fluctuation (dashed lines). The instantaneous position of the flame front is shown with isolevels of heat release (black solid lines) [27].

$$\frac{Q'}{Q} = 0 \quad (2.13)$$

$$\frac{Q'}{Q} = \frac{m'_i}{\bar{m}_i} \quad (2.14)$$

$$\frac{Q'}{Q} = -\kappa \frac{m'_i}{\bar{m}_i} e^{i\omega\tau} \quad (2.15)$$

$$(2.16)$$

$$\frac{Q'}{Q} = \kappa \frac{\Phi'_i}{\bar{\Phi}_i} = -\kappa \frac{u'_i \sin(\omega\Delta\tau)}{\bar{u}_i \omega\Delta\tau} e^{i\omega\tau} \quad (2.17)$$

$$\frac{Q'}{Q} = \kappa_p \frac{p'_i}{\bar{p}_i} e^{i\omega\tau_u} + \kappa_u \frac{u'_i}{\bar{u}_i} e^{i\omega\tau_u} + \kappa_v \frac{v'_i}{\bar{v}_i} e^{i\omega\tau_v} + \kappa_w \frac{w'_i}{\bar{w}_i} e^{i\omega\tau_w} \quad (2.18)$$

Model (2.13) makes the hypothesis of flame kinematics independent from flow field. As first approximation this is very useful because it cuts off all the eigenmodes connected with the flame. In effect such a model is a sub case of all the other models when $\kappa_i = 0$. In model (2.14) the heat release is considered directly dependent from the mass flow rate perturbation at the reference point i , that could be fuel injection point, for example.⁶ Model (2.15) due to Crocco is a sort of milestone in transfer function evolution since it represents the delay time of perturbations from a reference point to the flame sheet. At present this is the most frequently used model since it seems to represent fairly well the physics of the system. Unfortunately, parameters κ

⁶Such a model was used in previous work. See section 3.1

and τ have to be tuned accurately otherwise results are far from be reliable. All of these equations have a common hypothesis: a flat thin flame. The thin assumption at first glance seems to be reasonably acceptable since the flame thickness δ_L have an order of magnitude of $10^{-3} \sim 10^{-2}$ m, small enough if compared with combustor geometry. Analyzing better this hypothesis, if we consider that the flame is interacting with waves, we have to perform a dimensional analysis that compares wavelength λ with δ_L . The κ - τ model in (2.15) is suitable to represent the physics of the system only if $\delta_L \ll \lambda$. Thus, respectively for acoustic and convective waves, let us evaluate this limit considering very prudent values for the speed of sound, the mean flow velocity and the flame thickness:

$$\lambda_{ac} = \frac{c_s}{f} \implies f \ll \frac{c_s}{\delta_L} \approx \frac{800m/s}{2cm} = 40 \text{ KHz}$$

$$\lambda_{cv} = \frac{\bar{u}}{f} \implies f \ll \frac{\bar{u}}{\delta_L} \approx \frac{20m/s}{2cm} = 1 \text{ KHz}$$

Since humming is a phenomenon occurring at low frequency $\omega \ll 1 \text{ KHz}$, the thin flame assumption is a good approximation beyond any doubt even for convective waves. On the contrary the flat flame assumption seems to be very weak because reactions are distributed over a very complex three-dimensional surface distributed over a not negligible length as in figure 2.14. Model (2.17) proposed in [21] tries to model a three-dimensional flame surface through a varying value of τ . Finally model (2.18) considers several dependency associating to every quantity proper values for κ and τ . This is a more complete model but it is very hard to calibrate since there are several degree of freedom.

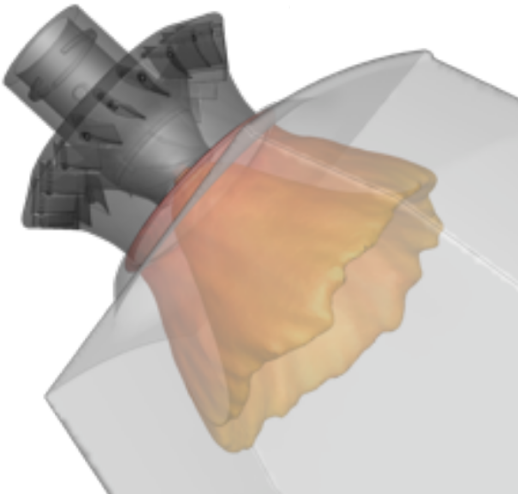


Figure 2.14 - *Three dimensional flame surface, LES simulation.*

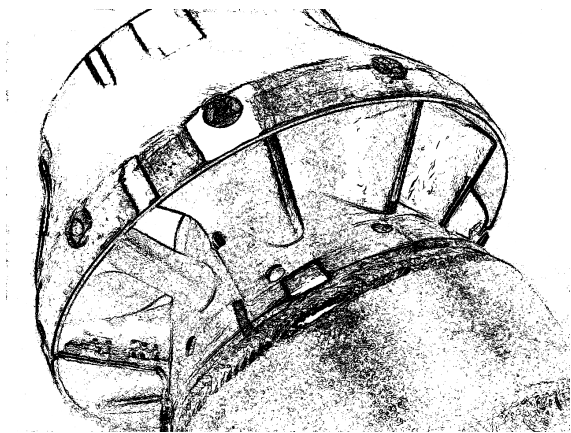


Figure 2.15 - *Swirler*

Taking a glance at all the issues presented, it is clear that a strong physical model where empirical parameters are not critical is still far from having been developed.

Until such a theory is available results from a lumped approach are hardly reliable and appropriate tuning of the model parameters must be constantly carried out against full simulations or/and experimental results. Thus, almost all efforts at this time tend towards the development of a good transfer function.

The shape of the flame surface is connected with the indispensable anchoring of the flame itself. To gain this condition the flame speed must be taken into account: the turbulent flame velocity for methane in air is about $S_T \approx 10 \text{ m/s}$. Since mean flow velocity in each combustor is about 7 times faster, flame stabilizer are required. In order to achieve stability, the presence of recirculation is a simply and safe way to get in the flow field a surface where $\bar{u} = S_T$. Recirculation is obtained due to the concurrent presence of a sudden cross sectional area increase and a swirler that provides a Swirl number $Sw = (\text{Moment of momentum})/(\text{Momentum} \cdot \text{Radius})$ greater then the minimum required (about 0.5). These devices provide a lobed shape of the flame as shown in figure 2.14.

Increasing mean flow velocity will shift the flame downstream. A second condition for stability is that the time flow is in contact with hot recirculating fluid (τ_c) must be greater than the time required for ignition (τ_i); these two characteristic times are:

$$\tau_c \approx \frac{L_{REC}}{\bar{u}} \approx \frac{d}{U_{BlowOff}} \quad \tau_i \approx \frac{\alpha_T}{S_L^2}$$

where S_L is the laminar flame velocity (about 1 m/s) and α_T the thermal diffusivity.

In order to prevent flashbacks grids are usually placed at the beginning of the premix. Thank to quenching phenomena the upstream transmission of the flame is inhibited. Grids that generate pressure drop are already modelled in the present code.

In figure 2.15 only the diagonal swirler is visible. Indeed near the axis there is also an axial swirler that processes about 10 % of the total mass flow rate. Finally, near the axis there is a pilot diffusion flame that grants ignition for every operating condition. The downstream shifting of the flame when the velocity in the burners increases cannot be neglected when choosing the geometry. In fact the coupling between azimuthal modes at the flame might be shifted downstream, where the radius is smaller. At present no data allow to appreciate the appropriateness of this statement.

Chapter 3

Starting point

This thesis is part of a broader project conducted by Ansaldo Energia for the design of new gas turbines, known as *AE94.3A*. Currently, research evolves along several directions, since many aspects must be investigated, such as the physics of the flame, its interactions with mean flow perturbations, damping and controlling devices able to avoid instabilities, 3D computations useful to have a better idea of phenomena, etc. The collaboration with DICAT begun in 2008 and is focused on providing a code able to evaluate the influence of several parameters on the onset of instabilities. This code should be useful in the design phase in order to understand where and what to modify when instabilities arise. Furthermore, a flame model is to be investigated and calibrated.

3.1 Increasing complexity

Since the complete problem has never been treated completely in the literature small steps toward a more complex set of equations are required. Analytical treatment is developed as far as possible in order to achieve a more complete comprehension of the problem and to gain a better computational efficiency when possible. Every step has been validated with experimental data and CFD numerical results from the literature. The Matlab environment has been chosen for the development of the codes because of its easy and straightforward programming. In figure 3.1 the increasing complexity of the subsequent models is shown.

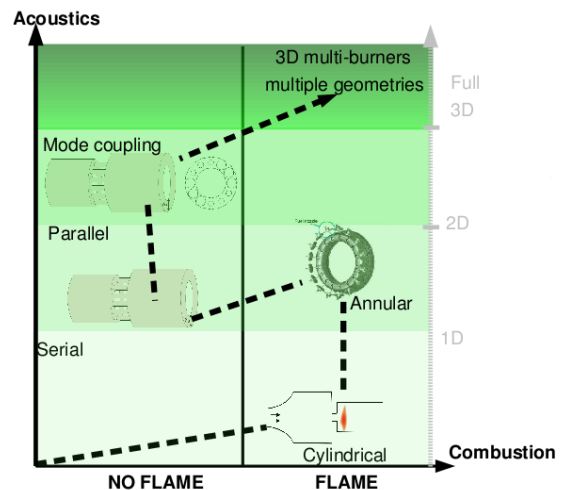


Figure 3.1 - *Steps currently carried out.*

The basic idea is to analyze the combustor of a gas turbine through a set of equations suited to represent the system. The approach chosen is a time-domain state space

representation derived from modern control theory. The internal state variables are the smallest possible subset of system variables that can represent the entire state of the system at any given time. The variables are expressed as vectors and the differential and algebraic equations that represent the system are written in matrix form (the latter only being possible when the dynamical system is linear or it is linearized). The number of unknown variables (i.e. the length of the relative vector) must be equal to the number of equations (i.e. to the rank of the relative matrix) in order to have a well posed problem. Sometimes, and this is the case here, the equations available are less than required and transfer functions are required. A transfer function is an equation that couples two or more variables. It is important to understand that using a transfer function form instead of physical principles may cause the loss of information of the system, and may provide a description of a system which is stable, when the state-space realization is unstable at certain points.

Internal variables for a gas turbine system are the perturbations of thermodynamic variables such as pressure, velocity or heat release. The combustor is composed by several ducts such as an annular diffuser at the compressor exit, 24 premixers and an annular combustion chamber just before the turbine entry. Since we use a lumped approach the system is uniquely represented by the amplitude of the perturbations of the thermodynamic variables in each duct together with heat release perturbation at the flame. Equations are deduced from conservation principles at the junctions of each duct (*jump conditions*), together with well posed boundary conditions. Furthermore a transfer function that couples heat release with other variables is required to close the problem.

The present matrix has more than one hundred rows and if vorticity terms are going to be included the number of unknowns should still grow in further models. Since the complexity of an immediate approach to the complete problem is large, easier models have been treated before the more complex ones. Let us take an overview of these models synthesized in figure 3.1.

Rijke tube. The first model produced was a simple one-dimensional system consisting of two ducts of the same cross sectional area separated by a thin flame at a fixed point. Two basic flame models were chosen and fuel injection is located exactly at the flame coordinate. In this case the influence of the Mach number (figure 3.3 A) and of heat release magnitude (figure 3.3 B) has been investigated. Moreover it allowed to detect immediately how critical the flame model is.

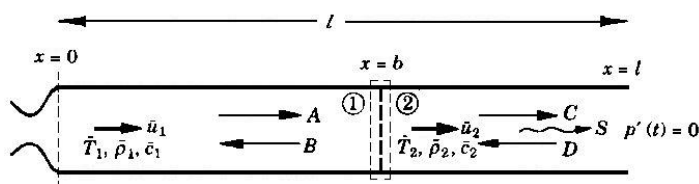


Figure 3.2 - *First one-dimensional model*

Parametric study on Mach number (Ma_1) and on heat release magnitude ($\bar{T}_{02}/\bar{T}_{01}$) were performed in order to achieve awareness of their influence on eigenfrequencies. These results were validated in [3].

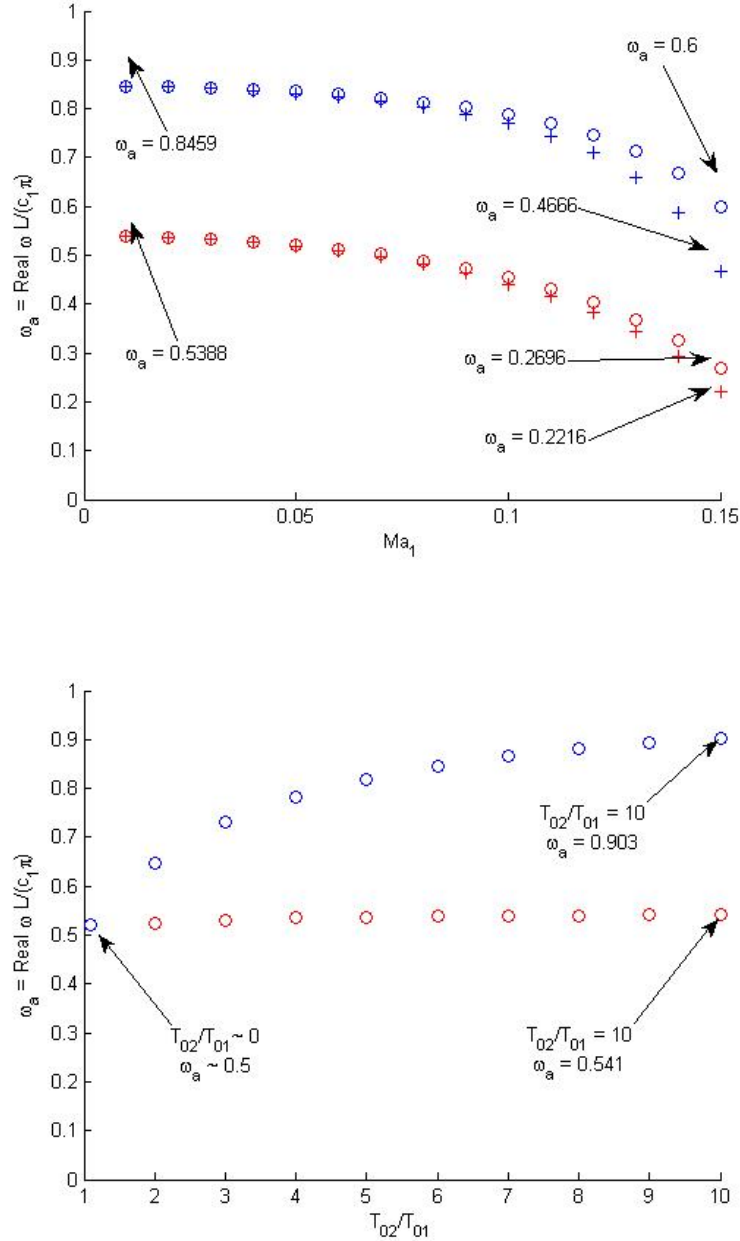


Figure 3.3 - Minimum frequency for (a): $\bar{T}_{02}/\bar{T}_{01} = 6$; (b): $Ma_1 = 0$. \circ : no heat release perturbation $\langle q' = 0 \rangle$. \circ : heat release perturbation proportional to mass flow rate perturbation $\langle q' = c_p(T_{02} - T_{01})(\bar{\rho}_1 u'_1 + \rho'_1 \bar{u}_1) \rangle$.

Single burner. A more complex geometry was eventually elaborated to approach a real burner geometry (lower right part of figure 3.1). Three ducts were considered: a large plenum that collects air from a compressor; a small premixer where fuel and

oxydizer are mixed separated by the combustion chamber by a still thin flame located exactly at the area increase. A more complex flame model was required in order to take into account that fuel is injected far upstream from the combustion process. A further parameter κ was added to have the possibility to vary continuously the sensitivity of the heat release perturbation to mean flow perturbations. The so called κ - τ model was: ¹

$$Q' = -\kappa \bar{Q} \frac{m'_i}{\bar{m}_i} e^{-i\omega\tau} \quad (3.1)$$

where m'_i and \bar{m}_i are mass flow rates calculated at area decrease where the premixer begins. The parameter τ is the so called time lag, i.e. the time a perturbations generated were fuel is injected takes to reach the flame. The κ - τ model influence was highlighted by results in figures 3.4 and 3.5:

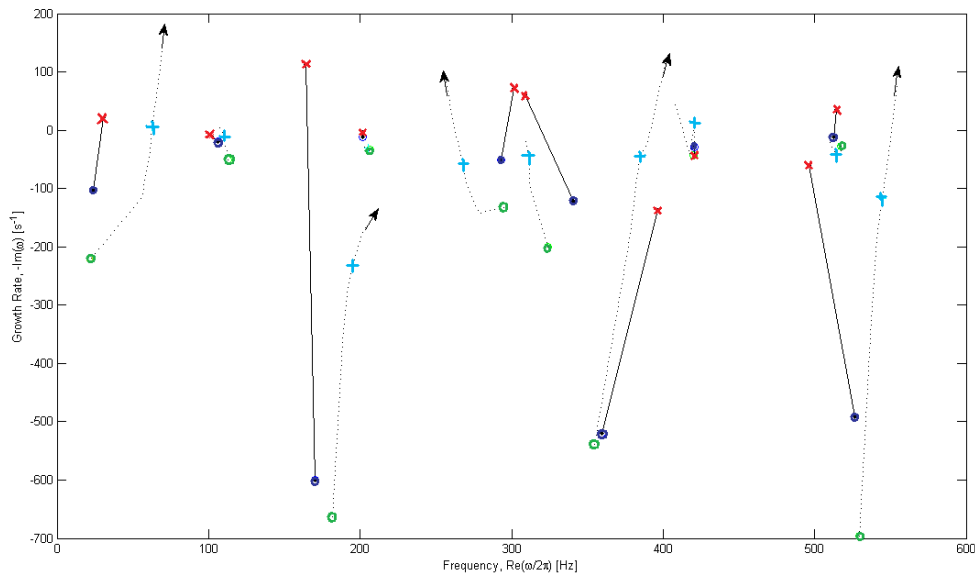


Figure 3.4 - Comparison between results obtained for $\kappa = 0$ (o) and $\kappa = 1$ ($+$) and resonance mode from [5] for $\kappa = 0$ (o) and $\kappa = 1$ (x).

So, even if it could be a suitable model, it needs a careful calibration that requires experimental data or CFD numerical solutions obtained with the same, or at least compatible, boundary conditions and assumptions.

2D model: annular duct. Since it is known from experience that thermoacoustic instabilities occurs in nowadays combustion chambers primarily along the circumferential direction, the model above omits the most interesting eigenfrequencies. Therefore the following steps consist in developing a two dimensional model that takes into account also the azimuthal coordinate. The expressions for the perturbations include also

¹See section 4.6 for a more complete treatment of the flame transfer function model.

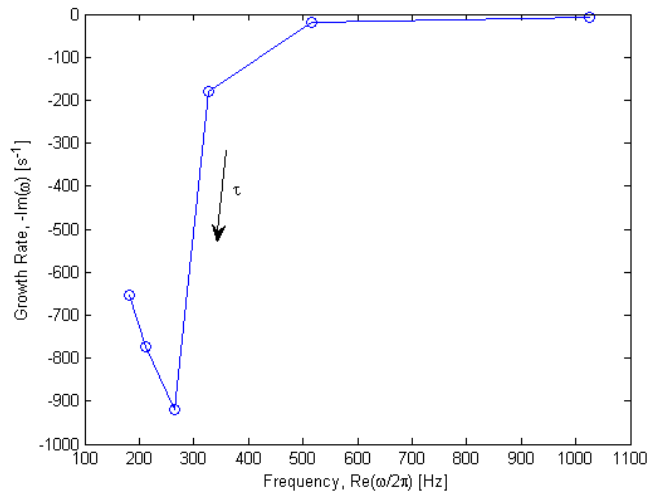


Figure 3.5 - Sensitivity of a mode of oscillation to τ choice

an $e^{in\theta}$ term where n represent the index of each azimuthal wave. Obviously this model incorporates the previous one since an ' $n = 0$ ' mode has no circumferential oscillation and thus it is purely axial.

Parallel burners. Again, from experience, it is known that adding *CBO's* at the end of some burners is positive for stability.² Thus, the modelling of all 24 burners is required. Jump conditions become more complex since each burner communicates only with a section of other ducts. Moreover, the equations suddenly become much more than before and the computation of the determinant of the matrix begins to be much slower than in previous models.

Modal coupling. Adding *CBO's* in the combustion chamber geometry breaks the axisymmetry. Modes of oscillation are no longer suitable to be represented by pure tones. A Fourier series expansion is thus needed, with all the modes coupled to one another. This is the actual model used in further test campaigns. See section 4.3 for the analytical treatment.

3D model: radial dependency. Finally, a radial dependency is taken into account to completely represent the system with all its features. See chapter 7 for the analytical treatment.

²See section 4.3.

Chapter 4

The governing equations

The spread of disturbances, in the absence of heat release, is exactly described by the acoustic d'Alembert equation. According to reality, the presence of a flame and a mean flow convective terms are taken into account modifying the energy equation and including a material derivative. Moreover, many systems of heat release generate significant pressure drop due to friction that certain components, like grids, exert on the fluid.

Hypothesis

- Volume forces $\rho\mathbf{g}$ negligible.
- Ideal gas¹: $\nu = 0$; c_p , c_v constant independent from temperature; $p = \rho RT$.
- Lumped parameters: in every duct the values of the mean flow variables are considered spatially constant.
- Linear approach: it is assumed that all quantities are the sum of a constant part and a variable one where the latter has a lower scale, so a generic G can be written as $\bar{G} + G'(t)$ where \bar{G} is the constant part associated with mean flow and G' the variable part, i.e. the perturbation. This assumption allows to neglect non linear terms (product of perturbations), provided that $G' \ll \bar{G}$.
- Speed of sound $c_s^2 = \left(\frac{\partial p}{\partial \rho}\right)_s = \gamma p / \rho = \gamma RT$.
- The flame is considered as a thin sheet where reactions are instantaneous.
- No evaluation of chemical composition is done; evolving gas is always considered air in both side of the flame and consequently no diffusion term such as $-\rho_M D_{i-M} \nabla y_i^2$ is taken into account.

¹Despite this assumption friction is not completely neglected because it is modelled when grids are present.

² ρ_M is the density of the mixture, D_{i-M} is the molecular diffusivity of the species i in the mixture M and ∇y_i is the gradient of the mass fraction of the species i itself.

4.1 No mean flow and heat release

Without mean flow and heat release the governing equation is d'Alembert equation. Writing the conservation equations we get:

Continuity

$$\begin{aligned}\frac{\partial(\bar{\rho} + \rho')}{\partial t} + \nabla \cdot ((\bar{\rho} + \rho')v') &= 0 \\ \frac{\partial \rho'}{\partial t} + \nabla \cdot (\bar{\rho}v') + \nabla \cdot (\rho'v') &= 0 \\ \frac{\partial \rho'}{\partial t} + \bar{\rho}(\nabla \cdot v') &= 0\end{aligned}\tag{4.1}$$

Momentum

$$\begin{aligned}(\bar{\rho} + \rho') \left(\frac{\partial v'}{\partial t} + v' \nabla \cdot v' \right) &= -\nabla(\bar{p} + p') \\ \bar{\rho} \frac{\partial v'}{\partial t} &= -\nabla p'\end{aligned}\tag{4.2}$$

Energy

$$\begin{aligned}(\bar{T} + T') \left(\frac{\partial}{\partial t}(\bar{S} + S') + v' \cdot \nabla(\bar{S} + S') \right) &= 0 \\ \frac{\partial S'}{\partial t} &= 0.\end{aligned}\tag{4.3}$$

Thermodynamic variable ρ could be decomposed, according to its dependency from other variable, as:

$$d\rho = \left(\frac{\partial \rho}{\partial p} \right)_S dp + \left(\frac{\partial \rho}{\partial S} \right)_p dS.$$

Combining the speed of sound relationship and the energy equation we get:

$$\rho' = c_s^{-2} p'.$$

Deriving with respect to time and considering continuity:

$$\frac{c_s^{-2}}{\bar{\rho}} \frac{\partial p'}{\partial t} + \nabla \cdot v' = 0.\tag{4.4}$$

Taking the divergence of the momentum equation we have:

$$\bar{\rho} \frac{\partial}{\partial t} \nabla \cdot v' = -\nabla^2 p'.$$

Finally, substituting in (4.4) we get:

$$\frac{\partial^2 p'}{\partial t^2} = c_s^2 \nabla^2 p',$$

that is d'Alembert equation.

This is an hyperbolic equation. The general solution (considering a one-dimensional propagation) will be:

$$p'(x, t) = f(x - c_s t) + g(x + c_s t) = f(\xi) + g(\eta),$$

where f and g are obtained from initial conditions (they give the wave's shape). They are respectively waves propagating towards positive x and negative x . In the simple case of sinusoidal waves the solution reduces to

$$p' = Ae^{i(kx - \omega t)} + Be^{i(kx + \omega t)}.$$

4.2 Adding mean flow and heat release

Unfortunately, the set of equations (4.1 - 4.3) is too simplified to represent phenomena taking place in a real gas turbine. To get a more realistic model involving mean flow and heat release, the equation to consider is:

$$\frac{D^2 p'}{Dt^2} - c_s^2 \nabla^2 p' = \bar{\rho}(\gamma - 1) \frac{Dq'}{Dt}$$

where the presence of a material derivative (a convective term) and of the heat release rate should be noted.

Let us analyze the structure of a real gas turbine combustor. It is clear that the one-dimensional solution able to solve D'Alembert equation severely limits the validity of the model. In annular plenum and combustion chamber waves could propagate not only along the axial direction but also in the azimuthal and radial ones.

Let us consider both the plenum and the combustion chamber as narrow annular ducts where $(r_e - r_i) \ll (r_e + r_i)$. We can assume that waves cannot propagate in the radial direction, considering only azimuthal and axial waves to be significant. Generally the perturbations of thermodynamic quantities are the sum of three different contributions called acoustic, vorticity and entropy wave:

$$p' = p'_a + p'_v + p'_e.$$

Acoustic wave. An expression for the acoustic wave is obtained from the resolution of a system composed by conservation equations in cylindrical coordinates:

$$\frac{\partial \rho'_a}{\partial t} + \bar{u} \frac{\partial \rho'_a}{\partial x} + \bar{\rho} \left(\frac{\partial u'_a}{\partial x} \right) = 0 \quad (4.5)$$

$$\bar{\rho} \left(\frac{\partial u'_a}{\partial t} + \bar{u} \frac{\partial u'_a}{\partial x} \right) = - \frac{\partial p'_a}{\partial x} \quad (4.6)$$

$$\rho'_a = \frac{p'_a}{\bar{c}^2} \quad (4.7)$$

$$\nabla \times \mathbf{v}' = \left(\frac{\partial \rho'_a}{r \partial \theta} - \frac{\partial w'_a}{\partial x} \right). \quad (4.8)$$

The acoustic wave is characterized by the superposition of two waves travelling upstream (A_-) and downstream (A_+). It is clear that the latter is faster in an absolute reference system due to the convective contribution of the mean flow. Here is the expression for the pressure disturbance:

$$p'_a(x, \theta, t) = A_{\pm} e^{i(k_{\pm}x + i\omega t + n\theta)} \quad (4.9)$$

where the wave number k_{\pm} for non dispersive waves is:

$$k_{\pm} = \frac{\bar{M}\omega \mp \sqrt{\omega^2 - \frac{n^2\bar{c}^2}{r^2}(1 - \bar{M}^2)}}{(1 - \bar{M}^2)\bar{c}}.$$

From the entropic relationship (4.7) we get an expression for density

$$\rho'_a(x, \theta, t) = \frac{1}{\bar{c}^2} A_{\pm} e^{i(k_{\pm}x + i\omega t + n\theta)}.$$

From (4.6) we get the axial velocity disturbance expression:

$$u'_a(x, \theta, t) = \frac{k_{\pm}}{\bar{\rho}(\omega + \bar{u}k_{\pm})} A_{\pm} e^{i(k_{\pm}x + i\omega t + n\theta)}.$$

And finally from irrotationality we get the azimuthal disturbance:

$$w'_a(x, \theta, t) = \frac{n}{r\bar{\rho}(\omega + \bar{u}k_{\pm})} A_{\pm} e^{i(k_{\pm}x + i\omega t + n\theta)}$$

Entropy wave. With the proper boundary conditions $p'_e = 0$ and $u'_e = w'_e = 0$ it can be inferred that entropy influences only density (and temperature) perturbations. The conservations equations reduce to:

$$\frac{\partial \rho'_e}{\partial t} + \bar{u} \frac{\partial \rho'_e}{\partial x} = 0 \quad (4.10)$$

$$p'_e = 0 \quad (4.11)$$

$$u'_e = 0 \quad (4.12)$$

$$w'_e = 0 \quad (4.13)$$

and density perturbation turns out to be:

$$\rho'_e(x, \theta, t) = -\frac{1}{\bar{c}^2} A_e e^{i(k_0x + i\omega t + n\theta)}$$

where the axial wave number k_0 is:

$$k_0 = -\frac{\omega}{\bar{u}}$$

Vorticity wave. A vorticity wave is incompressible and isentropic, thus $\nabla \cdot u'_v = 0$ and $p' = \rho' \bar{c}^2$. Writing the continuity equation we get:

$$\frac{D\rho'_v}{Dt} = 0. \quad (4.14)$$

Hence, both density and pressure perturbations generated by vorticity are zero as well as temperature ones. The complete set of equations is:

$$\frac{\partial u'_v}{\partial x} + \frac{1}{r} \frac{\partial w'_v}{\partial \theta} = 0 \quad (4.15)$$

$$\frac{\partial u'_v}{\partial t} + \bar{u} \frac{\partial u'_v}{\partial x} = 0 \quad (4.16)$$

$$\frac{\partial w'_v}{\partial t} + \bar{u} \frac{\partial w'_v}{\partial x} = 0 \quad (4.17)$$

The only quantities influenced by vorticity are the velocity components:

$$u'_v(x, \theta, t) = \frac{n}{\bar{\rho}\bar{c}} A_v e^{i(k_0 x + i\omega t + n\theta)} \quad (4.18)$$

$$w'_v(x, \theta, t) = -\frac{k_0 r}{\bar{\rho}\bar{c}} A_v e^{i(k_0 x + i\omega t + n\theta)} \quad (4.19)$$

The resulting perturbations are then the sum of all previous expressions.

$$p'(x, \theta, t) = [A_+ e^{ik_+ x} + A_- e^{ik_- x}] e^{i(\omega t + n\theta)} \quad (4.20)$$

$$\rho'(x, \theta, t) = -\frac{1}{\bar{c}^2} [A_+ e^{ik_+ x} + A_- e^{ik_- x} - A_e e^{ik_0 x}] e^{i(\omega t + n\theta)} \quad (4.21)$$

$$u'(x, \theta, t) = \left[-\frac{k_+}{\bar{\rho}\alpha_+} A_+ e^{ik_+ x} - \frac{k_-}{\bar{\rho}\alpha_-} A_- e^{ik_- x} + \frac{n}{\bar{\rho}\bar{c}} A_v e^{ik_0 x} \right] e^{i(\omega t + n\theta)} \quad (4.22)$$

$$w'(x, \theta, t) = \left[-\frac{n}{r\bar{\rho}\alpha_+} A_+ e^{ik_+ x} - \frac{n}{r\bar{\rho}\alpha_-} A_- e^{ik_- x} + \frac{k_0 r}{\bar{\rho}\bar{c}} A_v e^{ik_0 x} \right] e^{i(\omega t + n\theta)} \quad (4.23)$$

We are able to write this set of expressions in a more convenient matrix form:

$$\begin{Bmatrix} p' \\ \rho' \\ v' \\ w' \end{Bmatrix} = \Gamma \cdot \mathbf{a}(x, \theta, t) \quad (4.24)$$

where:

$$\Gamma = \begin{bmatrix} 1 & 1 & 0 & 0 \\ 1/\bar{c}^2 & 1/\bar{c}^2 & -1/\bar{c}^2 & 0 \\ -k_+/\bar{\rho}\alpha_+ & -k_-/\bar{\rho}\alpha_- & 0 & n/\bar{\rho}\bar{c} \\ -n/r\bar{\rho}\alpha_+ & -n/r\bar{\rho}\alpha_- & 0 & -k_0 r/\bar{\rho}\bar{c} \end{bmatrix}$$

$$\mathbf{a}(\mathbf{x}, \theta, t) = \begin{Bmatrix} A_+ e^{i(k_+ x + n\theta + \omega t)} \\ A_- e^{i(k_- x + n\theta + \omega t)} \\ A_e e^{i(k_0 x + n\theta + \omega t)} \\ A_v e^{i(k_0 x + n\theta + \omega t)} \end{Bmatrix}$$

In the present model vorticity waves are neglected, reducing the perturbations to the sum of acoustic and entropy contributions. Therefore, considering the pressure perturbation as given in equation (4.9), we get ρ' and T' from the expressions:

$$\begin{aligned} d\rho &= \left(\frac{\partial\rho}{\partial p}\right)_S dp + \left(\frac{\partial\rho}{\partial S}\right)_p dS \\ dT &= \left(\frac{\partial T}{\partial p}\right)_S dp + \left(\frac{\partial T}{\partial S}\right)_p dS \end{aligned}$$

where, writing ds and $d\rho$ as $c_p dT/T$ and $-\rho dT/T$ respectively, we get:

$$\rho' = \frac{1}{c^2} p' - \frac{\bar{\rho}}{c_p} S' \quad (4.25)$$

$$T' = \frac{1}{\bar{\rho} c_p} p' - \frac{c^2}{(\gamma - 1) c_p^2} S'. \quad (4.26)$$

Just to lighten the expressions, the term $\bar{\rho}/c_p$ could be merged into A_e since the values of the amplitudes are arbitrary. The resulting expressions are:

$$\rho' = \frac{1}{c^2} p' - S' \quad (4.27)$$

$$T' = \frac{1}{\bar{\rho} c_p} p' - \frac{c^2}{(\gamma - 1) \rho c_p} S'. \quad (4.28)$$

Finally the effective set of unknowns used is:

$$\begin{Bmatrix} p' \\ \rho' \\ u' \\ w' \\ T' \end{Bmatrix} = \Gamma \cdot \mathbf{a}(x, \theta, t) \quad (4.29)$$

where:

$$\begin{aligned} \Gamma &= \begin{bmatrix} 1 & 1 & 0 \\ 1/\bar{c}^2 & 1/\bar{c}^2 & -1 \\ -k^+/\bar{\rho}\alpha^+ & -k^-/\bar{\rho}\alpha^- & 0 \\ -1/\bar{r}\bar{\rho}\alpha^+ & -1/\bar{r}\bar{\rho}\alpha^- & 0 \\ 1/\bar{\rho}c_p & 1/\bar{\rho}c_p & 1/\bar{\rho}c_p(\gamma - 1) \end{bmatrix} \\ \mathbf{a}(\mathbf{x}, \theta, t) &= \begin{Bmatrix} A_+ e^{i(k_+ x + n\theta + \omega t)} \\ A_- e^{i(k_- x + n\theta + \omega t)} \\ A_e e^{i(k_0 x + n\theta + \omega t)} \end{Bmatrix} \end{aligned}$$

4.3 Coupling between perturbations

Let us consider a model similar to the *AE94.3A* gas turbine geometry, as shown in figure 4.1.

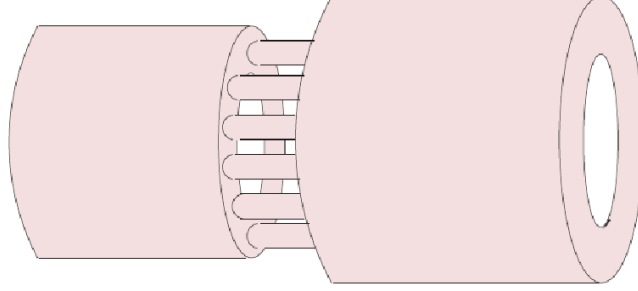


Figure 4.1 - *Geometry used for annular combustor*

In order to damp instabilities some burner could have a sort of additional quasi-cylindrical duct extending in the combustion chamber called *CBO* (Cylindrical Burner Outlet). This yields azimuthal asymmetry and leads to a different expression for the perturbations. We could find an explanation of this fact analyzing the governing PDE:

$$\frac{D^2 p'}{Dt^2} - c_s^2 \nabla^2 p' = \bar{\rho}(\gamma - 1) \frac{Dq'}{Dt}, \quad (4.30)$$

whose solution is (4.31) only if all the coefficients are constant:

$$p'(x, \theta, t) = [A_+ e^{ik_+ x} + A_- e^{ik_- x}] e^{i(\omega t + n\theta)}. \quad (4.31)$$

This implies that the mean flow should be equal in every single burner. But from mean flow calculations the velocities in burners with *CBO*'s are obviously slightly larger than the velocities in other burners. Practically convective terms present in the material derivative ($\mathbf{v} \cdot \nabla$) have non constant values due to these devices. Solution (4.31) no more satisfies equation (4.30) and so a more generic solution $p'(x, t)$ must be written down.

From signal theory we are able to write every function as a series of trigonometric functions, more precisely sinusoidal waves with the proper increasing frequency. Considering a generic annular duct, the pressure perturbations are written as follows.³

$$p'(x, r, \theta, t) = \sum_{n=-\infty}^{\infty} A_n^{\pm} e^{i(k_{\pm} x + \omega t + n\theta)} B_{n,m}(r)$$

where $B_{n,m}(r)$ is the sum of Bessel's functions of first and second kind of order n .

³See chapter 7 for the complete expression.

In the present work plenum and combustion chamber are modelled as thin annular ducts. This assumption allows to ignore radial modes that practically propagate with a small negligible amplitude if compared with axial and azimuthal ones. The effective expression for perturbations is then:

$$p'(x, \theta, t) = \sum_{n=-\infty}^{\infty} A_n^{\pm} e^{i(k_{\pm}x + \omega t + n\theta)}$$

The $e^{in\theta}$ term allows to reproduce both standing and travelling azimuthal waves. Obviously no sum from $-\infty$ to ∞ can be performed but a proper number N_n of coupled modes is chosen and the effective perturbation expression becomes:

$$p'(x, \theta, t) = \sum_{n=-N_n/2+1}^{N_n/2} A_n^{\pm} e^{i(k_{\pm}x + \omega t + n\theta)}$$

Referring to all expressions we get:

$$\begin{Bmatrix} p' \\ \rho' \\ u' \\ w' \\ T' \end{Bmatrix} = \sum_{n=-N_n/2+1}^{N_n/2} \Gamma \cdot \mathbf{a}(x, \theta, t) \quad (4.32)$$

where:

$$\Gamma = \begin{bmatrix} 1 & 1 & 0 \\ 1/\bar{c}_n^2 & 1/\bar{c}_n^2 & -1 \\ -k_n^+/\bar{\rho}_n\alpha_n^+ & -k_n^-/\bar{\rho}_n\alpha_n^- & 0 \\ -n/\bar{r}\bar{\rho}_n\alpha_n^+ & -n/\bar{r}\bar{\rho}_n\alpha_n^- & 0 \\ 1/\bar{\rho}_nc_p & 1/\bar{\rho}_nc_p & 1/\bar{\rho}_nc_p(\gamma - 1) \end{bmatrix}$$

$$\mathbf{a}(\mathbf{x}, \theta, t) = \begin{Bmatrix} A_n^+ e^{i(k_n^+x + n\theta + \omega t)} \\ A_n^- e^{i(k_n^-x + n\theta + \omega t)} \\ A_n^e e^{i(k_n^0x + n\theta + \omega t)} \end{Bmatrix}$$

$$k_n^{\pm} = \frac{\bar{M}_n\omega + \sqrt{\omega^2 - \frac{n^2\bar{c}^2}{\bar{r}_n^2}(1 - \bar{M}_n^2)}}{(1 - \bar{M}_n^2)\bar{c}_n}$$

$$k_n^0 = -\frac{\omega}{\bar{u}_n} \quad \alpha_n^{\pm} = \omega + \bar{u}_nk_n^{\pm}$$

The number N_n of coupled modes is to be chosen according to the number of equations and unknowns. We consider N_n azimuthal modes in the plenum and combustion chamber, and only axial modes in the N_b premixers and in the N_{CBO} CBO's. Neglecting vorticity waves there three unknowns for each mode (A_+ , A_- and A_e) and N_b heat release \bar{Q} (split between the premixers). The total number of unknowns is then:

$$N_{unknowns} = 3(2N_n + N_b + N_{CBO}) + N_b$$

The equation available are:

- $2N_n$ inlet boundary conditions;
- N_n outlet boundary conditions;
- N_b flame transfer functions;
- $3N_b$ interface equations between plenum and premixers;
- $3N_{CBO}$ interface equations between premixers and $CBO's$;
- $3N_{CBO}$ interface equations between $CBO's$ and combustion chamber;
- $3(N_b - N_{CBO})$ interface equations between premixers and combustion chamber.

Thus the total number of equation is:

$$N_{equations} = 3N_n + 7N_b + 3N_{CBO}.$$

Since the number of equations must equalize the number of unknowns, the equation

$$6N_n + 4N_b + 3N_{CBO} = 3N_n + 7N_b + 3N_{CBO}$$

is satisfied for any value of N_{CBO} only if $N_n = N_b$. Thus the number of coupled modes is given once the number of burners is fixed.

As a rule linear coupling between waves requires equal phase velocity and polarization. Thus, vorticity and entropy waves never couple with any other wave because of generically different polarizations. Considering acoustic waves coupling, k_+ must be equal to k_- in order to have the same polarization:

$$\frac{\bar{M}\omega + \sqrt{\omega^2 - \frac{n^2\bar{c}_s^2}{r^2}(1 - \bar{M}^2)}}{(1 - \bar{M}^2)\bar{c}_s} = \frac{\bar{M}\omega - \sqrt{\omega^2 - \frac{n^2\bar{c}_s^2}{r^2}(1 - \bar{M}^2)}}{(1 - \bar{M}^2)\bar{c}_s}$$

$$\omega_c = \pm \frac{n\bar{c}_s}{r} \sqrt{1 - \bar{M}^2}. \quad (4.33)$$

Taking $M = 0.06$, $c_s = 835m/s$, $r = 1.6m$ (that is the case of the combustion chamber), with $n = 1$ we get $\omega_c \simeq 83Hz$ and with $n = 2$ we get $\omega_c \simeq 166Hz$. If $\omega \gg \omega_c$ modal coupling is inhibited.

4.4 Equations for the mean flow computation

4.4.1 Perfect gas equations

A perfect gas equation is written in each duct:

$$p = \rho r T,$$

\rightsquigarrow *i.e.* 4 perfect gas equations.

4.4.2 Mass flux conservation equations

The mass flux conservation, written locally at each premixer inlet, imposes

$$\dot{m}_1 = N_b \dot{m}_2,$$

At the exit of premixers with CBO, we have

$$\dot{m}_2 = \dot{m}_{2b},$$

and in the combustion chamber

$$\dot{m}_1 = \dot{m}_3,$$

\rightsquigarrow *i.e.* 3 mass flux conservation equations.

4.4.3 Energy conservation equations

The energy conservation between the plenum and the premixers gives

$$\dot{m}_1 H_1 = N_b \dot{m}_2 H_2,$$

with H the enthalpy defined as $H = c_p T + U^2/2$. Between the CBOs and their corresponding premixers, we have

$$\dot{m}_2 H_2 = \dot{m}_{2b} H_{2b},$$

and at the combustion chamber inlet:

$$\dot{m}_3 H_3 = \dot{m}_1 H_1 + A_3 Q_T,$$

\rightsquigarrow *i.e.* 3 energy conservation equations.

4.4.4 Isentropic/grid conditions

The turbine configuration includes a grid at each premixer inlet. Its influence is neglected in the present computation, so that the isentropic condition – usual for an area decrease – applies:

$$p_1/p_2 = (\rho_1/\rho_2)^\gamma;$$

if the grid had not been neglected, the following grid-type equation could be used:

$$p_1 - p_2 = \frac{1}{2} k_{12} \rho_2 u_2^2,$$

where k_{12} is a loss parameter,

\rightsquigarrow *i.e.* 1 isentropic/grid equation.

4.4.5 Borda equations

We write a Borda equation at each CBO inlet:

$$\dot{m}_2 u_2 - \dot{m}_{2b} u_{2b} = A_{2b} (p_{2b} - p_2),$$

and a Borda-like equation for the set of premixers/CBOs reaching the combustion chamber:

$$\dot{m}_3 u_3 - \sum_{k=1}^{N_{cbo}} \dot{m}_{2b}^k u_{2b}^k - \sum_l \dot{m}_2^l u_2^l = \frac{A_3}{N_b} \left(\sum_{k=1}^{N_{cbo}} p_{2b}^k + \sum_l p_2^l \right) - A_3 p_3,$$

where $l \leq N_b$ represents the index of the burners without CBO,
 \rightsquigarrow *i.e. 2 Borda equations.*

The total number of equations is then $N_{eq}^{\text{mean}} = 13$. Once a proper number of boundary conditions is known it is possible to solve the non-linear system of equations thank to an optimization tool. The unknowns most suitable to be taken as boundary conditions are the inlet pressure, temperature and mass flow rate and the flame temperature. Since LOMTI is a lumped model the inlet values are exactly the values inside the entire plenum p_1 , T_1 and \dot{m}_1 as well as the flame temperature represents the mean temperature of the entire combustion chamber T_3 .

4.5 Perturbations equations

The set of equations for the perturbations are the linearized equations of the mean flow computations shown before. Let us write them explicitly.

4.5.1 Mass flux conservation equations

As the perturbation in the plenum depends on θ (see figure 6.1), the local mass flux conservation equation at each premixer inlet becomes

$$d_1 R_1 \int_{\theta^i - \pi/N_b}^{\theta^i + \pi/N_b} (\rho_1 u_1)' d\theta = (\dot{m}_2^i)', \quad 1 \leq i \leq N_b.$$

At the exit of premixers with CBO, the mass conservation simply is

$$(\dot{m}_2^i)' = (\dot{m}_{2b}^i)', \quad 1 \leq i \leq N_{cbo},$$

and in the combustion chamber

$$d_3 R_3 \int_{\theta^i - \pi/N_b}^{\theta^i + \pi/N_b} (\rho_3^i u_3^i)' d\theta = (\dot{m}_k^i)', \quad 1 \leq i \leq N_b,$$

where $k = 2$ for the burners without CBO and $k = 2b$ for the burners with *CBO's*. So we have

\rightsquigarrow $(2N_b + N_{cbo})$ *mass flux conservation equations.*

4.5.2 Energy conservation equations

As for the mass flux, we write locally an energy conservation equation at each pre-mixer inlet:

$$d_1 R_1 \int_{\theta^i - \pi/N_b}^{\theta^i + \pi/N_b} (\rho_1 u_1 H_1)' d\theta = (\dot{m}_2^i H_2^i)', \quad 1 \leq i \leq N_b.$$

At the exit of premixers with CBO, the energy equation reads

$$(\dot{m}_2^i H_2^i)' = (\dot{m}_{2b}^i H_{2b}^i)', \quad 1 \leq i \leq N_{cbo},$$

and in the combustion chamber

$$d_3 R_3 \int_{\theta^i - \pi/N_b}^{\theta^i + \pi/N_b} (\rho_3 u_3 H_3)' d\theta = (\dot{m}_k^i H_k^i)' + \frac{A_3}{N_b} (Q^i)', \quad 1 \leq i \leq N_b,$$

i.e. $\rightsquigarrow (2N_b + N_{cbo})$ energy conservation equations.

4.5.3 Isentropic conditions

As for the mean flow, we write for the perturbation a linearized isentropic condition at each pre-mixer inlet:

$$(p_1/p_2^i)' = ((\rho_1/\rho_2^i)^\gamma)', \quad 1 \leq i \leq N_b,$$

\rightsquigarrow *i.e.* N_b isentropic equations.

4.5.4 Borda equations

Similarly, the Borda equations are the linearized form of those used for the mean flow. At each CBO inlet:

$$(\dot{m}_2^i u_2^i)' - (\dot{m}_{2b}^i u_{2b}^i)' = A_{2b}^i [(p_{2b}^i)' - (p_2^i)'], \quad 1 \leq i \leq N_{cbo},$$

and for each duct reaching the chamber:

$$(\dot{m}_k^i u_k^i)' + \frac{A_3}{N_b} p_k' = d_3 R_3 \int_{\theta^i - \pi/N_b}^{\theta^i + \pi/N_b} [(\rho_3 u_3^2)' + p_3'], \quad 1 \leq i \leq N_b,$$

\rightsquigarrow *i.e.* $(N_b + N_{cbo})$ Borda-like equations.

In order to complete the problem the acoustic boundary conditions at the inlet of the plenum and at the outlet of the combustion chamber are required together with a flame model for each burner.

4.5.5 Inlet and outlet conditions

Three kinds of inlet conditions are implemented:

- a closed-end inlet/outlet where $u' = 0$ (infinite impedance);
- an open-end inlet/outlet where $p' = 0$ (zero impedance);
- a choked inlet/outlet where $\dot{m}' = 0$.

In each case, we suppose that the inlet condition is verified independently by each of the N_b modes in the plenum and we have:

$\rightsquigarrow N_b$ inlet conditions;

$\rightsquigarrow N_b$ outlet conditions.

4.5.6 Flame transfer function

Under the hypothesis that flames issuing from neighbouring injectors do not interact, we use the so-called ISAAC (Independence Sector Assumption in Annular Combustor) assumption to define the flame transfer function. It states that

”the heat release fluctuations in a given sector [of the combustion chamber] are only driven by the fluctuating mass flow rates due to the velocity perturbations through its own swirler.”

This means that a local transfer function is written for each of the N_b flames with a specific perturbation in heat release $(Q^j)'$, $1 \leq j \leq N_b$, and with a different reference point each time, chosen at the inlet of its own pre-mixer:

$$\frac{(Q^j)'}{Q} = \sum_g^{N_g} F_g(\omega) \frac{(G^g)'}{G^g} \quad 1 \leq j \leq N_b,$$

where g represents the index related to the N_g quantity G that appears in the flame transfer function.

\rightsquigarrow i.e. N_b equations to define the N_b parts of Q' .

4.6 Flame model

The acoustic of the combustion chamber is strictly correlated with the unsteady heat release. Therefore a correct estimate of the flame dynamics is needed to provide accurate predictions. The actual flame model is based on a transfer function where the perturbations of mass flow rate (or velocity) are linked to the heat release fluctuations at a reference point close to the combustor inlet.

Modelling a flame dynamics is difficult since several mechanisms enter the picture, such as chemical kinetics, convective and diffusion terms, fuel injection, turbulent behaviour and flame anchoring. The theory may become suddenly inextricable [11], and the huge quantity of unknown parameters yields actually to a useless model.

Some assumptions are required in order to obtain a simple and available model. Neglecting the physiological ones (such as homogeneous mixing between species and instantaneous reactions) the main assumption is that we are considering the flame as a thin flat interface separating premixers from combustion chamber. Thus we link unsteady heat release to mass flow rate fluctuations according to the so called κ - τ model:

$$Q' = \bar{Q} \frac{\dot{m}_i'}{\dot{m}_i} \kappa e^{-i\omega\tau}$$

This method needs to gather a priori information coming from numerical simulations or experimental data only for the two parameter κ and τ . The importance of these parameters has been highlighted in chapter 3.

Validity of the model. The time lag τ is, by definition, the convection time between a point i , located upstream of the flame, and the flame itself. Generally the position of this point could vary in practical applications. In actual models the fuel injection point is often used as a reference. Let L_{i-f} be this critical distance; it has been shown [17] that the flame transfer function problem is ill-defined if L_{i-f} is not small enough. Fortunately, it is possible to quantify this limit using the Helmholtz number defined by:

$$H_n = \frac{\omega L_{i-f}}{c_s}$$

This number could be arranged as follows:

$$H_n = \frac{\omega L_{i-f}}{\lambda_s f_s} = \frac{2\pi L_{i-f}}{\lambda_s}$$

Theoretically H_n has to be the smallest possible. In practice, there are problems to perform measurements near the flame, also because of its oscillating position. However values of the Helmholtz number less $H_n = 10^{-2}$ are required to ensure that the estimated parameters κ and τ are independent from the outlet conditions, and are thus intrinsic characteristics of the combustion chamber.

Obviously no measurement is performed since our model is completely numerical. But just for this fact when mass flow perturbation (or velocity one) is evaluated at the beginning of the premixers a numerical error occurs making the Helmholtz number limit a real restriction. An explanation of this statement is shown in figure 4.2 where frequency is evaluated with a 5% of approximation between black and red line. It is clear that significant errors arise only for higher frequency

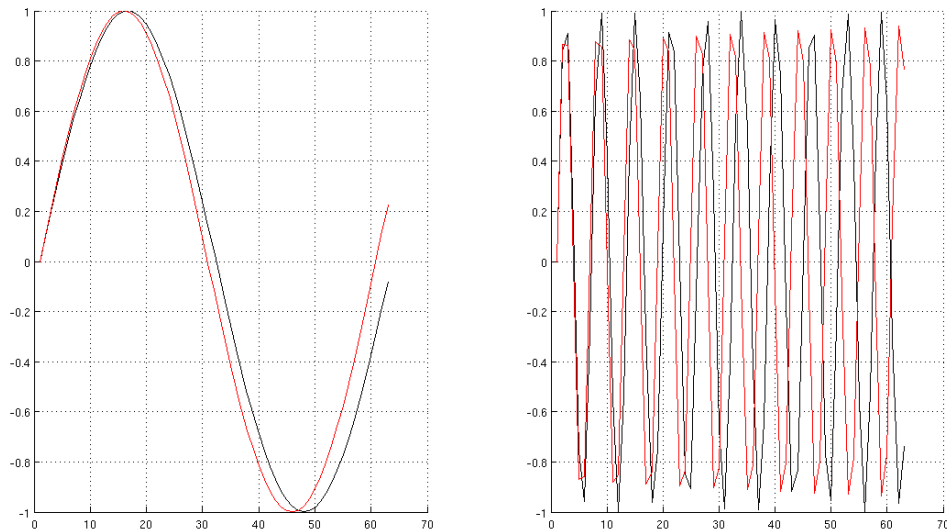


Figure 4.2 - Error for low and higher frequencies.

An important thing to note here is that low values of ω are required to satisfy this criterion. If L_{i-f} is not small enough there will be a limitation on the allowable values of the resonant frequencies, thus restricting the validity of the model to low-frequency modes. In effect considering *AE94.3A* gas turbine L_{i-f} is equal to the length of pre-mixers thus $L_{i-f} = 142\text{ mm}$ and $c_s = 528\text{ m/s}$. Therefore ω should be smaller than 37 rad/s , i.e. $f < 6\text{ Hz}$!

According to these statements κ and τ seems not to be intrinsic parameters of the flame, vanishing all the efforts made to obtain reliable results. A parametric study on L_{i-f} is performed in section 6.4.

Chapter 5

Calibration of LOMTI parameters against a 3D COMSOL simulation

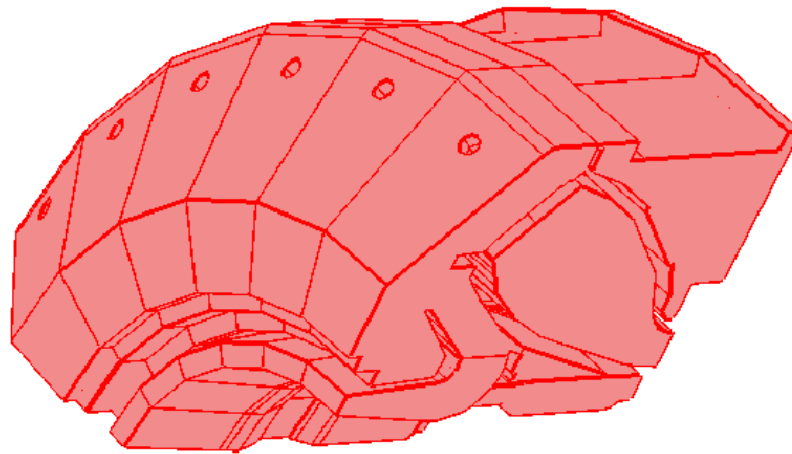


Figure 5.1 - *Geometry for 3D simulation*

Figure 5.2 presents a comparison of the computational domains used in COMSOL (left) and in LOMTI (right). From figure 5.2, it appears that the most complex part to model in LOMTI's lumped parameters approach is the plenum. Only the volume coloured in blue, along which air travels from the compressor exit to the burners inlet, is suitable to be represented in LOMTI. This means that the outer part of the plenum (colored in pink in figure 2.11(a)/LOMTI) will not be modelled. Besides, the real plenum contains some narrow gaps which cannot obviously be included in LOMTI (see also section 5.5). The geometrical parameters chosen for the premixers are those already used in Sesta [16]. Finally, as a first approximation, the combustion chamber is represented by a single annular duct (volume coloured in green in figure 5.2).

The input parameters used for the computation in COMSOL are reported in table 5.1 and the input parameters used in LOMTI should be the same. It is no problem to use the same inlet/outlet boundary conditions and to consider or not the presence of

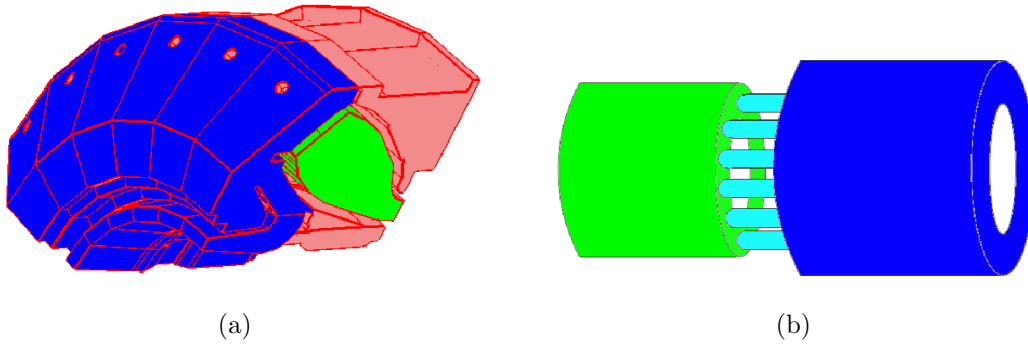


Figure 5.2 - (a) Geometry for COMSOL. (b) Geometry for LOMTI.

flame perturbations. However, for convergence reasons, it is not possible to run LOMTI with a zero Mach number (zero mass flow rate) and alternative mean flow parameters must be computed. Using the procedure described in [32], the mean flow parameters are computed by imposing the pressure and the temperature in the plenum equal to those used in COMSOL and choosing a small inlet mass flow rate equal to 19.85 kg/s . The mean parameters obtained are reproduced in table 5.2 for the calibrated geometry (see section 5.5, tables 5.4 and 5.6). The maximum Mach number obtained is 0.005, and we thus expect it not to influence significantly the solution¹.

Plenum and burners temperature	683.15 K
Plenum and burners pressure	16.43 bar
Flame temperature	1736 K
Mass flow rate	0
Boundary conditions (inlet/outlet)	$u' = 0$
No flame perturbation	$k = 0$

Table 5.1 - Input parameters for the COMSOL computations.

duct	p [bar]	ρ [kg/m^3]	T [K]	u [m/s]	c_s [m/s]	Ma
plenum	16.4300	8.379	683.15	0.51	523.95	0.97×10^{-3}
burners	16.4297	8.379	683.15	2.90	523.95	5.54×10^{-3}
chamber	16.4297	3.297	1736.20	1.741	835.28	2.08×10^{-3}

Table 5.2 - Mean flow parameters used in LOMTI for the calibrated geometry (see section 5.5, tables 5.4 and 5.6). The data in red are those available from COMSOL. The flame mean heat release, $Q = 6074 \text{ kW/m}^2$, has been chosen in order to get the "correct" temperature in the chamber.

¹The Mach number in the premixers in real turbine conditions is about 0.13 so it is here reduced to 3% of its original value.

Several geometrical parameters have to be chosen in order to calibrate LOMTI's geometry: the length, radius and thickness of the plenum and the combustion chamber, and the length and cross sectional area of the premixers, i.e. 8 parameters. This means that the calibration campaign requires plenty of computations – and of computation time – to obtain simply-to-understand information and trends. So, starting from the arbitrary initial geometry used in [32], we have to test the influence of these quantities one by one, assuming that the trends obtained would be similar if any of the other quantities were modified.²

Let us first analyze the results we want to obtain. The 3D COMSOL simulations are carried out initially without flame perturbation and without mean flow; therefore all modes obtained are neutral (i.e. with zero growth rates). Due to the non zero Mach number approximation used in LOMTI, the modes obtained will not be exactly neutral but stable.

With the original geometry from [32], we get the same number of modes in the selected range of frequency as with COMSOL. These modes are shown in figure 5.3 and, as expected, are slightly stable.

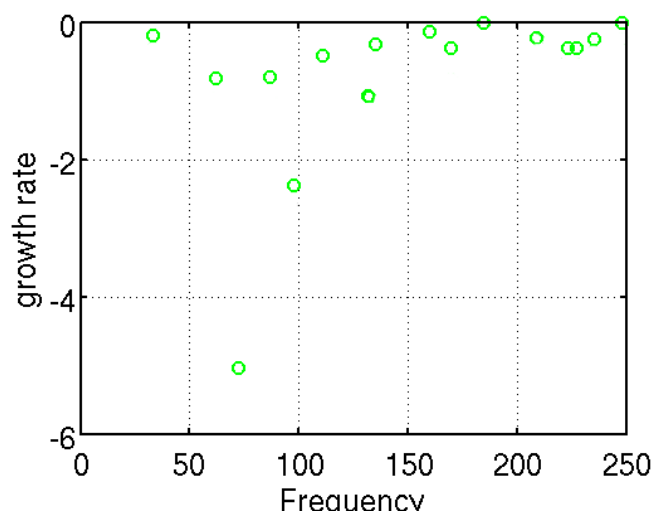


Figure 5.3 - *Frequencies calculated with LOMTI in the initial – non-calibrated– geometry, in the absence of flame disturbances.*

5.1 Influence of the plenum geometry

Starting from 0.8 m, the influence on the frequencies of increasing L_{plenum} is shown in figure 5.5. The frequencies obtained increase with the plenum length, but no monotonic effect is noted on the growth rates.

²Only three tests per parameter run for all the combinations would give 3^8 simulations, which would require more than 10^3 CPU hours.

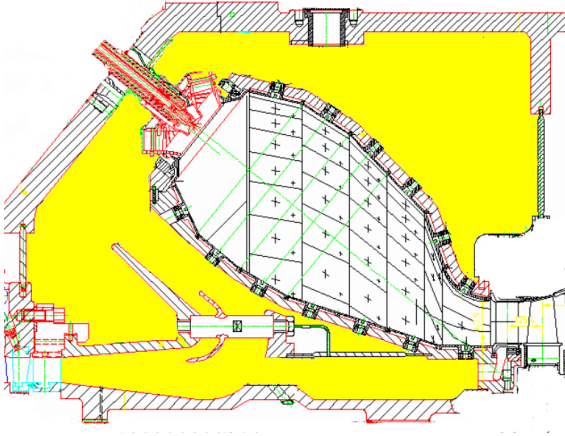


Figure 5.4 - Plenum (yellow area) in AE.95.A gas turbine combustor

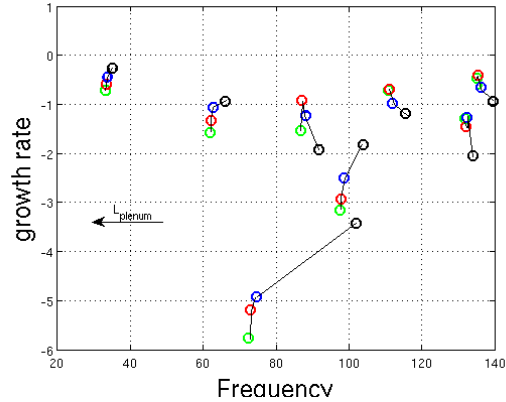


Figure 5.5 - Effect of the variation of plenum "acoustical length" on mode of oscillation. \circ : $L_{plenum} = 1.24 \text{ m}$; \circ : $L_{plenum} = 1.2 \text{ m}$; \circ : $L_{plenum} = 1 \text{ m}$; \circ : $L_{plenum} = 0.8 \text{ m}$;

The plenum radius has been originally arbitrarily set to 3.249 m . However, this value does not correspond to the real geometry, since the maximum radial extension in the plenum is somewhat less than 2 m . The choice of the plenum radius is critical. Our current model considers the plenum (and the combustion chamber) as a thin annular duct. In order to maintain the volume of the duct close to the real one, reducing its radius means increasing its thickness. The real volume is about $V_{real} = 10.692 \text{ m}^3$. Since we have to gain a so called acoustical length that should be smaller than the real one, we could expect that a "proper volume" should be smaller than V_{real} .

	Current Geometry	Modified Geometry
Plenum length L_{plenum}	1.24 m	0.8 m
Plenum radius R_{plenum}	3.249 m	2 m
Plenum thickness d_{plenum}	0.614 m	1.3 m
Plenum volume	14.073 m^3	8.821 m^3
r_{plenum}/d_{plenum}	18%	65%

Table 5.3 - Comparison between possible geometries

In order to obtain correct values for the azimuthal modes, it seems to be important to have a proper value for the radius (that means the circumferential extension through which an azimuthal mode can be established). This observation seems to lead to a sort of deadlock impossible to overcome without taking into account the radial dependency. Let us still analyze the effect of radial extension on the eigenfrequencies. In figure 5.6 it is clear how critical the choice of the radius is. Some frequencies such as those at about 60 Hz and at 135 Hz experience a large alteration, and move out of the window chosen for the parametric study. The effect of varying the plenum thickness is less critical, as shown in figure 5.7.

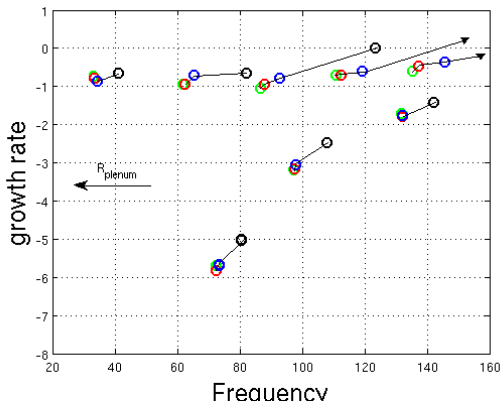


Figure 5.6 - Effect of the variation of plenum radius on mode of oscillation. \circ : $R_{plenum} = 3.249 \text{ m}$; \circ : $R_{plenum} = 3.2 \text{ m}$; \circ : $R_{plenum} = 2.5 \text{ m}$; \circ : $R_{plenum} = 2 \text{ m}$;

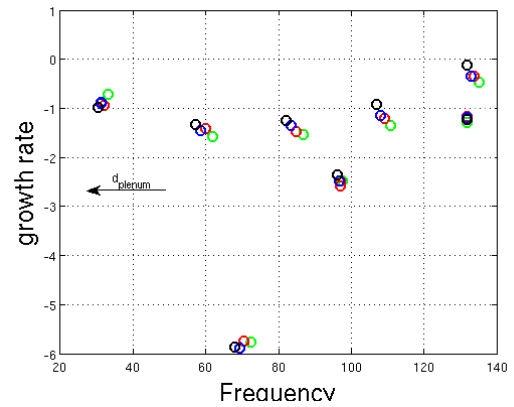


Figure 5.7 - Effect of the variation of plenum thickness on mode of oscillation. \circ : $d_{plenum} = 0.614 \text{ m}$; \circ : $d_{plenum} = 0.8 \text{ m}$; \circ : $d_{plenum} = 1 \text{ m}$; \circ : $d_{plenum} = 1.3 \text{ m}$;

5.2 Influence of the premixers geometry

In the final calibrated geometry, the length and cross-sectional area of the premixers (yellow area in figure 5.8) will remain the original ones already used in the computations for Sesta, i.e. $L_{premixer} = 0.142 \text{ m}$ and $A_{premixer} = 0.034 \text{ m}^2$. However, in order to provide an extensive study of the geometric parameters, the effect of increasing $L_{premixer}$ and $A_{premixer}$ is presented in figures 5.9 and 5.10, respectively. The results are similar to those obtained in the previous section when varying the plenum geometry, i.e. the modes growth rates do not vary monotonically with the length/area of the premixers, whereas the frequencies do: they decrease (increase) when the premixers length (section) increases.

Even if we have decided to keep the original premixers geometry, these figures provide a very important result. The length scales associated to the premixers are very small compared to those of plenum and chamber, so one could expect a minor effect on the frequencies when they vary. However, it appears that doubling the premixers length or cross-sectional area can shift some frequencies by 40% of their original value. This means that it is crucial to choose the premixers geometry correctly to obtain accurate and reliable results.

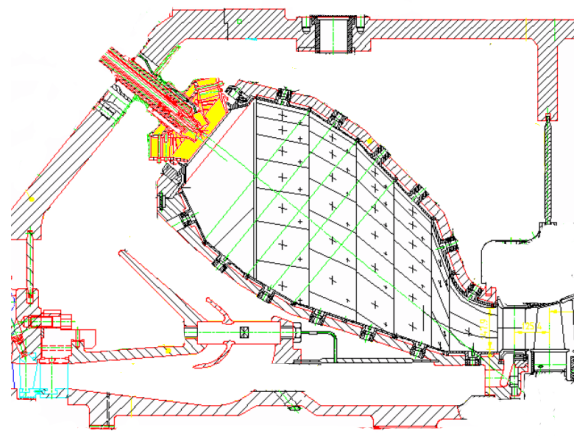


Figure 5.8 - A premixer (yellow area) in the AE.95.A gas turbine combustor

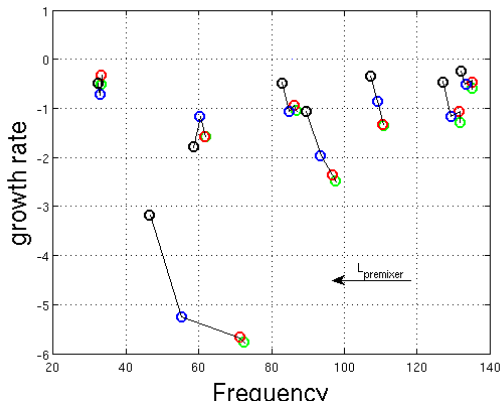


Figure 5.9 - Effect on the frequencies of varying the premixers length. \circ : $L_{premixer} = 0.142$ m; \circ : $L_{premixer} = 0.15$ m; \circ : $L_{premixer} = 0.2$ m; \circ : $L_{premixer} = 0.3$ m.

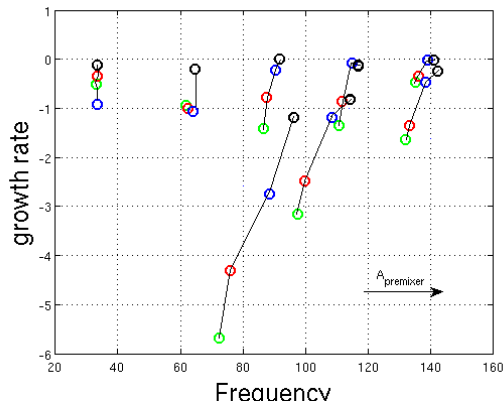


Figure 5.10 - Effect on the frequencies of varying the premixers cross section area. \circ : $A_{premixer} = 0.034$ m²; \circ : $A_{premixer} = 0.04$ m²; \circ : $A_{premixer} = 0.07$ m²; \circ : $A_{premixer} = 0.1$ m².

5.3 Influence of the combustion chamber geometry

The combustion chamber (colored in yellow in figure 5.11) is modelled as a single thin annular duct; this appears to be a more reasonable approximation than in the case of the plenum. Varying the annulus length has little influence on the frequencies (see figure 5.12); decreasing the length by 30% modifies the frequencies only by 15% in the worst case. The conclusion is the same for the annulus width, whose variations only slightly modify the results, as shown in figure 5.14.

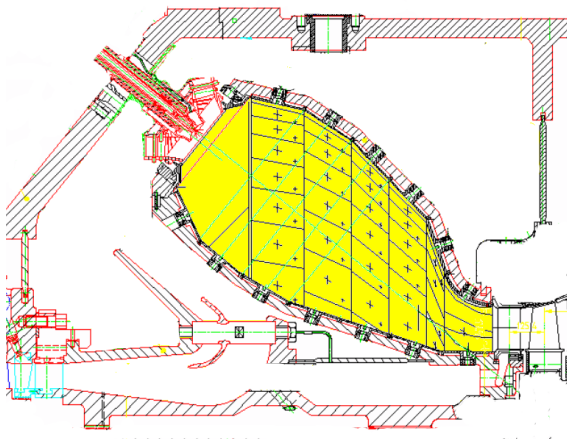


Figure 5.11 - Combustion chamber (yellow area) in AE.95.A gas turbine combustor

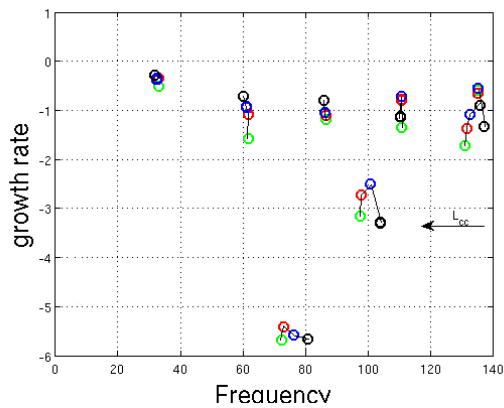


Figure 5.12 - Effect of the variation of combustion chamber length on mode of oscillation. \circ : $L_{cc} = 1.24$ m; \circ : $L_{cc} = 1.2$ m; \circ : $L_{cc} = 1$ m; \circ : $L_{cc} = 0.8$ m;

As in the plenum case, the most influential geometric parameter is the chamber radius R_{cc} . It appears in figure 5.13 that some frequencies strongly decrease when R_{cc}

increases. The frequency shift can be larger than 40% when R_{cc} decreases by 35%.

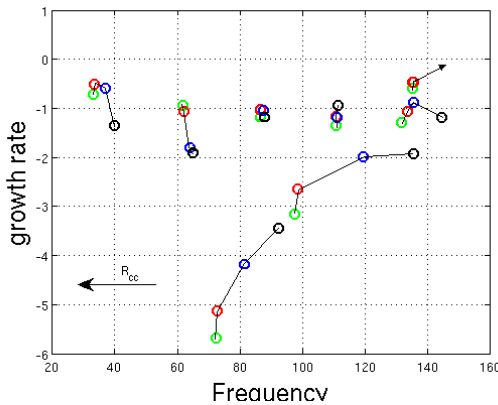


Figure 5.13 - Effect of the variation of combustion chamber radius on mode of oscillation. \circ : $R_{cc} = 3.249$ m; \circ : $R_{cc} = 3.2$ m; \circ : $R_{cc} = 2.5$ m; \circ : $R_{cc} = 2$ m;

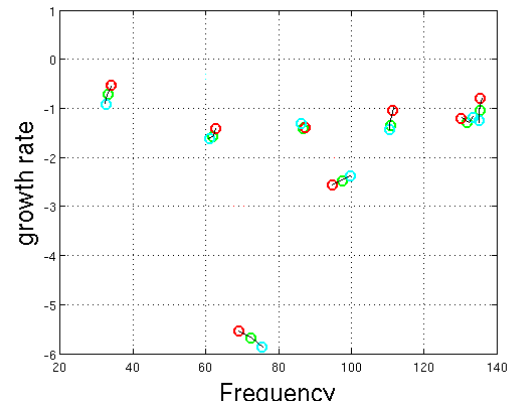


Figure 5.14 - Effect of the variation of combustion chamber thickness on mode of oscillation. \circ : $d_{cc} = 0.614$ m; \circ : $d_{cc} = 0.8$ m; \circ : $d_{cc} = 0.5$ m;

5.4 Calibration of the geometry

The parametric study of the previous sections now allows us to calibrate the geometric parameters in order to fit as much as possible COMSOL results. As already stated, we do not modify the premixers original geometry so that only the plenum and chamber parameters have to be chosen. Besides, considering the slight influence of the plenum/chamber thickness on the frequencies, we choose not to use them for calibration: they will be calculated as functions of the length/radius of the annuli in order to remain close to the real plenum/chamber volumes. The only restriction is that the chosen thickness remains small compared to the duct radius so that the thin annulus approximation holds and radial dependence can be neglected.

Choosing the plenum length is tricky, since internal reflections can create additional paths for the waves. Consequently, additional characteristic lengths are created, as for instance the one displayed in figure 5.15. Going on with this analysis, the plenum radius should be smaller than the real one, or better, than the maximum radius. This is because no obstruction seems to modify the circumferential path available. This deduction leads us to take a plenum radius close to 2 m.

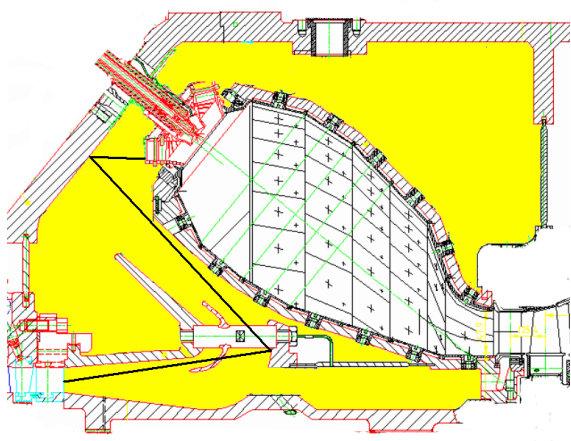


Figure 5.15 - A possible path for waves in the plenum, shown with a black segmented line.

As the model of the combustion chamber is relatively close to the real one, its length L_{cc} can be fixed to be equal to the real one. As in the plenum case, the combustion chamber radius chosen is smaller than the real one, i.e. smaller than 1.7 m , as a first approximation. Starting from these preliminary considerations, and knowing from the last sections the influence of each parameter, a – long and extensive– test campaign has been run in order to fix the geometry for LOMTI. The final results are presented in the next section, for the case $\kappa = 0$ (i.e. no flame perturbation).

5.5 Mode shape analysis

This section presents a comparison of the shape of the pressure perturbation for the frequencies obtained with COMSOL and with LOMTI in the final calibrated geometry. The geometric parameters chosen for the plenum and the chamber are presented in tables 5.4 and 5.6 respectively. The modes obtained with COMSOL are displayed in figures 5.16-5.28, and compared to those obtained with LOMTI when relevant.

To better understand the results, we recall the expression of a general pressure perturbation in LOMTI [32]:

$$p'(x, \theta, t) = \sum_{n=-N_n/2+1}^{N_n/2} A_n^\pm e^{i(k_\pm x + \omega t + n\theta)}.$$

Since the configuration is axisymmetric, no coupling between modes arises [15], which means that pure modes are easily recognizable in the mode shape visualization. It is thus possible to clearly identify for instance a " $n=2$ mode" in the combustion chamber or a " $n=4$ mode" in the plenum where " n " is the number of maxima (or minima) along the circumference.

In COMSOL results, modes at 105, 150.1, 150.4, 150.5, 196, and 202 Hz have been identified as characteristic of the plenum configuration. The geometric parameters in table 5.4 have been chosen in order to fit LOMTI results with these modes; the plenum thickness has been chosen in order to have the correct volume in the plenum.

A similar analysis has been developed for the combustion chamber geometry, considering the chamber modes at 116 and 193 Hz . Since both modes are azimuthal, they are strongly influenced by the radius value. Unfortunately, no radius value allowing to match both frequencies has been detected. The explanation probably resides in

LOMTI current lumped parameter approximation: only one characteristic radius is defined for the combustion chamber, whereas the real chamber geometry is of course more complex. This mismatch could possibly be overcome by splitting the combustion chamber into several ducts, with different adequate characteristic geometries. The final geometry in table 5.6 has been chosen to fit the frequency at 193 Hz .

Optimal Geometry	
Plenum length L_{plenum}	2.3 m
Plenum radius R_{plenum}	1.7 m
Plenum thickness d_{plenum}	0.435 m
Plenum volume V_{plenum}	10.68 m ³

Table 5.4 - *Final calibrated geometry for the plenum.*

Optimal Geometry	
Premixers length $L_{premixer}$	0.142 m
Premixers area $A_{premixer}$	0.034 m ²

Table 5.5 - *Final calibrated geometry for the premixers.*

Optimal Geometry	
Combustion chamber length L_{cc}	1.3 m
Combustion chamber radius R_{cc}	1.55 m
Combustion chamber thickness d_{cc}	0.355 m
Combustion chamber volume V_{cc}	4.495 m ³

Table 5.6 - *Final calibrated geometry for the combustion chamber.*

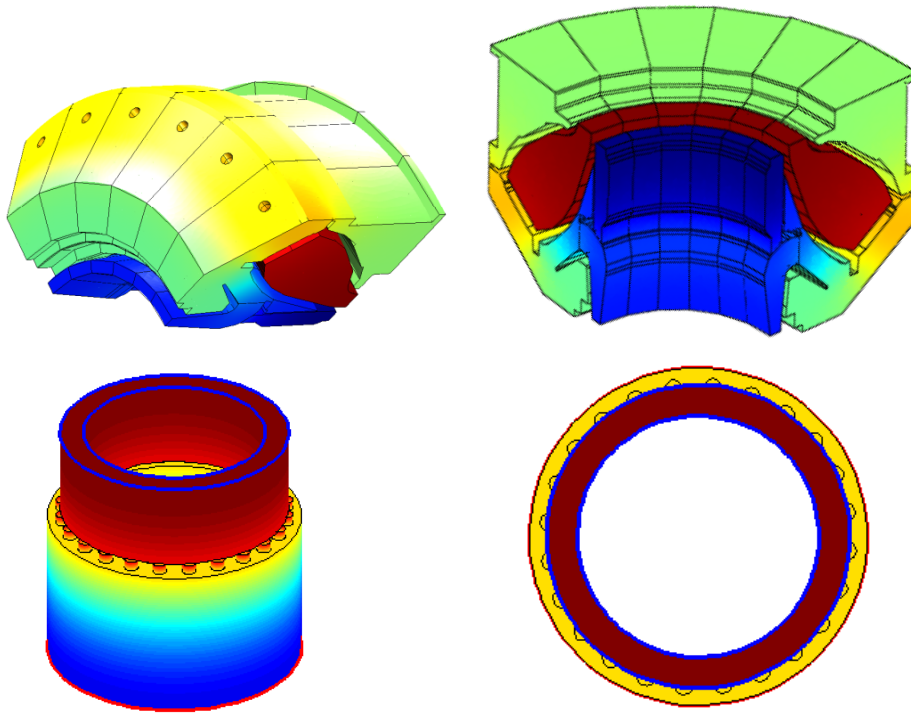


Figure 5.16 - Mode shape for the mode $n = 0$, obtained at 72 Hz with COMSOL (top) and 70 Hz with LOMTI (bottom).

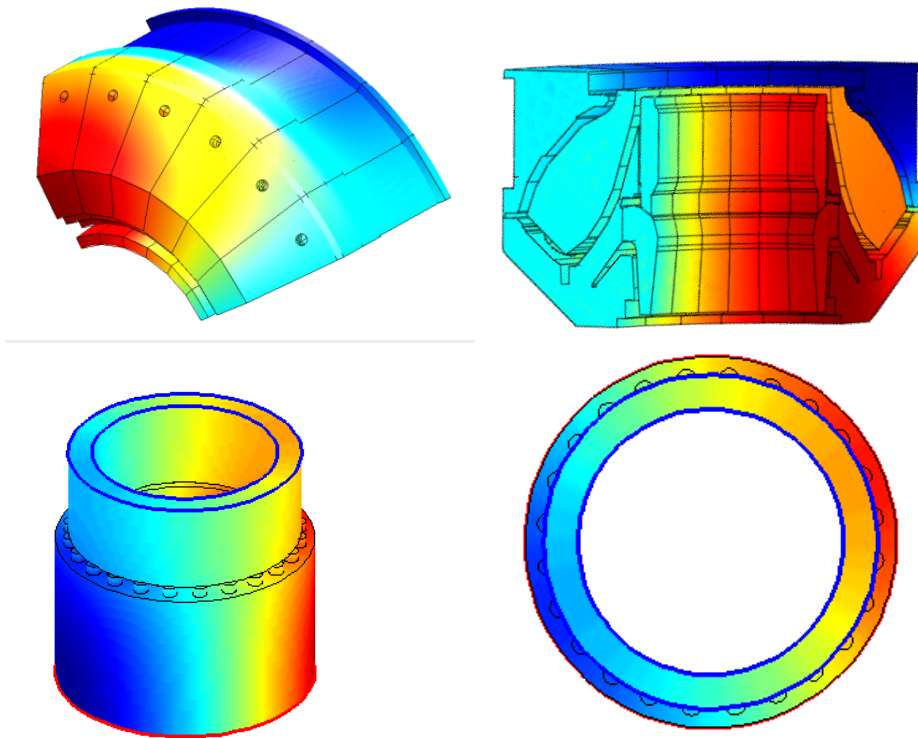


Figure 5.17 - Mode shape for the mode $n = 1$, obtained at 88 Hz with COMSOL (top) and 56 Hz with LOMTI (bottom).

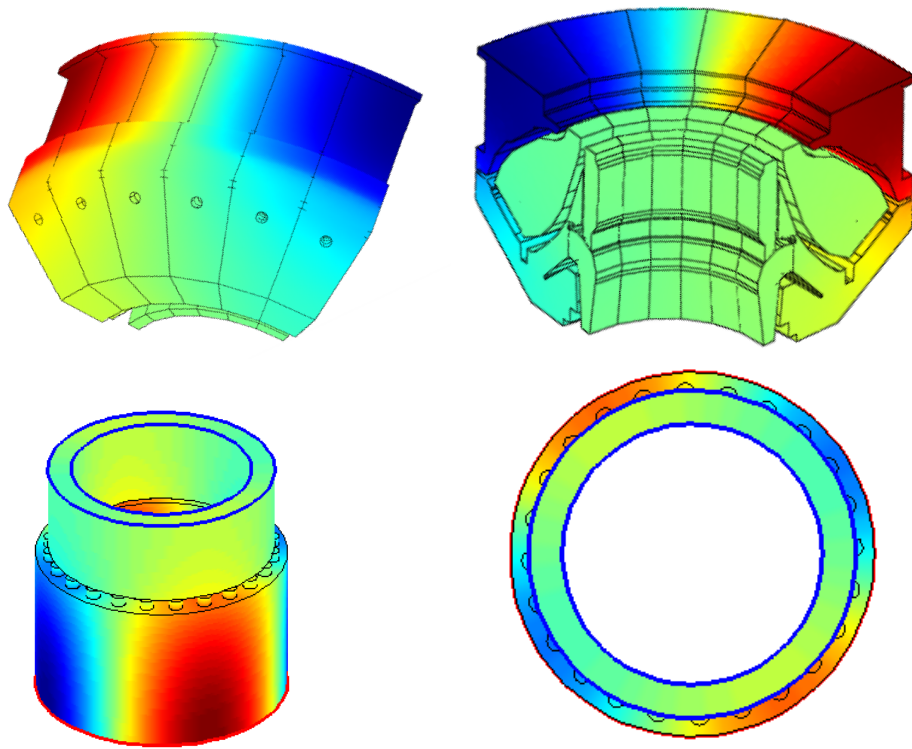


Figure 5.18 - Mode shape for the mode $n = 2$, obtained at 105 Hz with COMSOL (top) and 105 Hz with LOMTI (bottom).

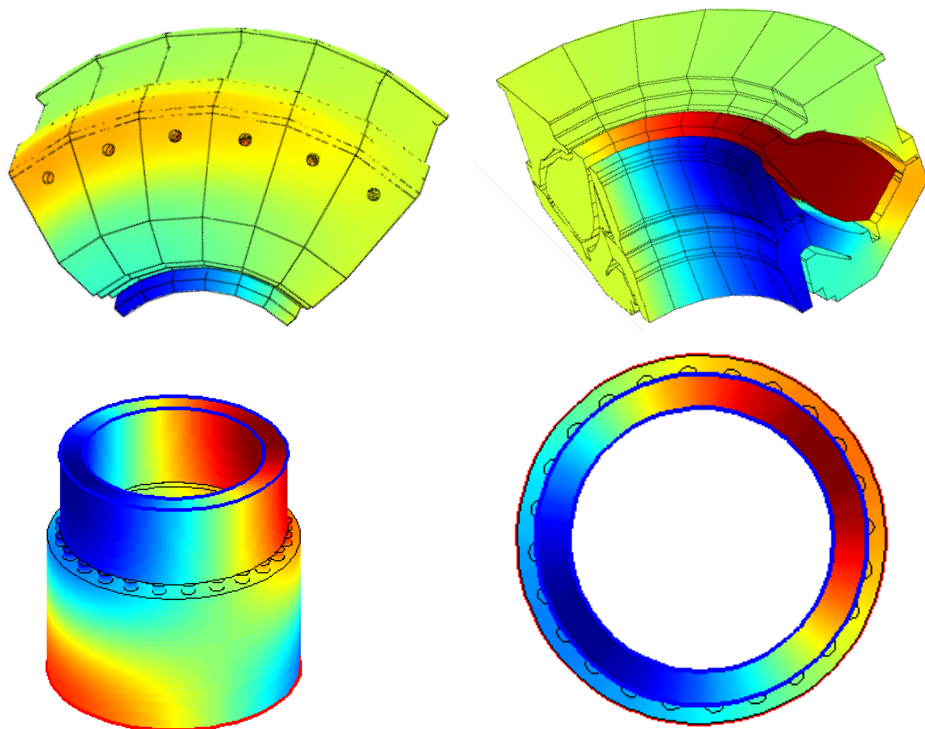


Figure 5.19 - Mode shape for the mode $n = 1$, obtained at 116 Hz with COMSOL (top) and 102 Hz with LOMTI (bottom).

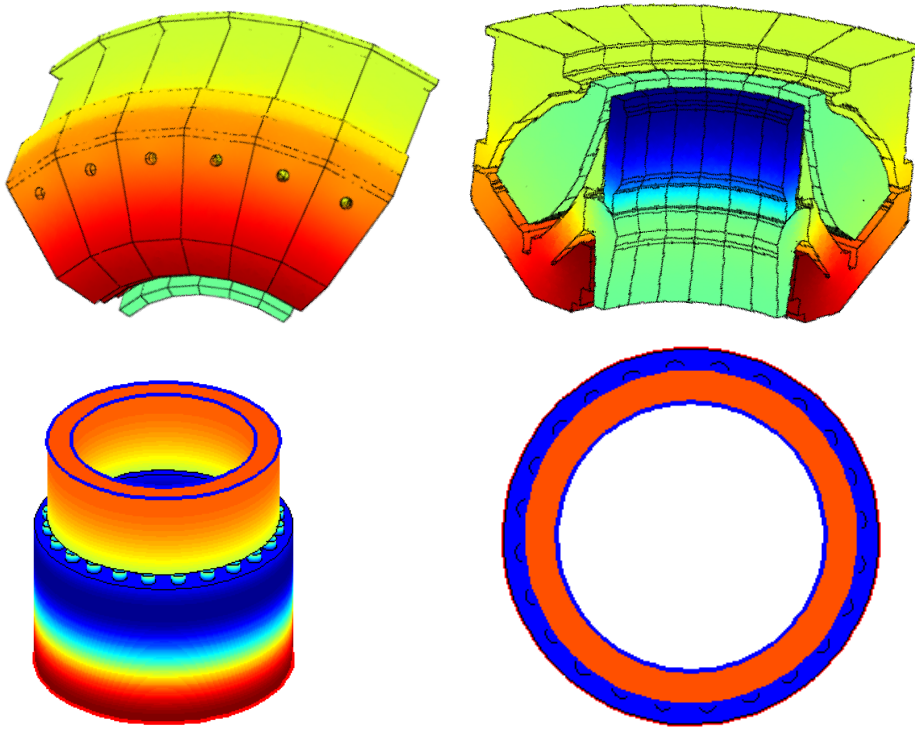


Figure 5.20 - Mode shape for the mode $n = 0$, obtained at 125 Hz with COMSOL (top) and 139 Hz with LOMTI (bottom).

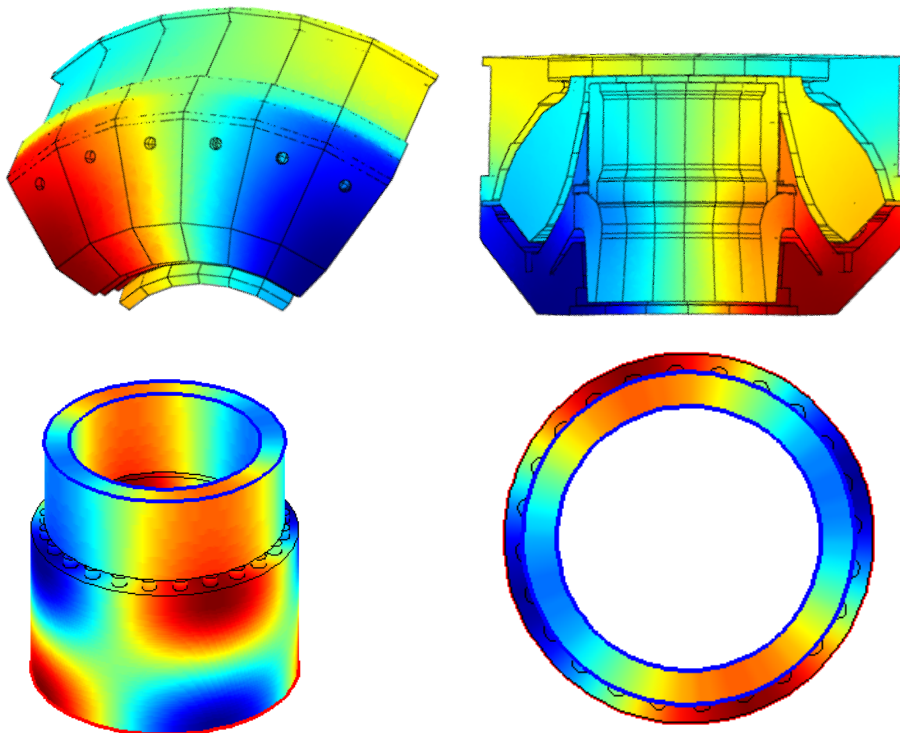


Figure 5.21 - Mode shape for the mode $n = 2$, obtained at 150.1 Hz with COMSOL (top) and 156 Hz with LOMTI (bottom).

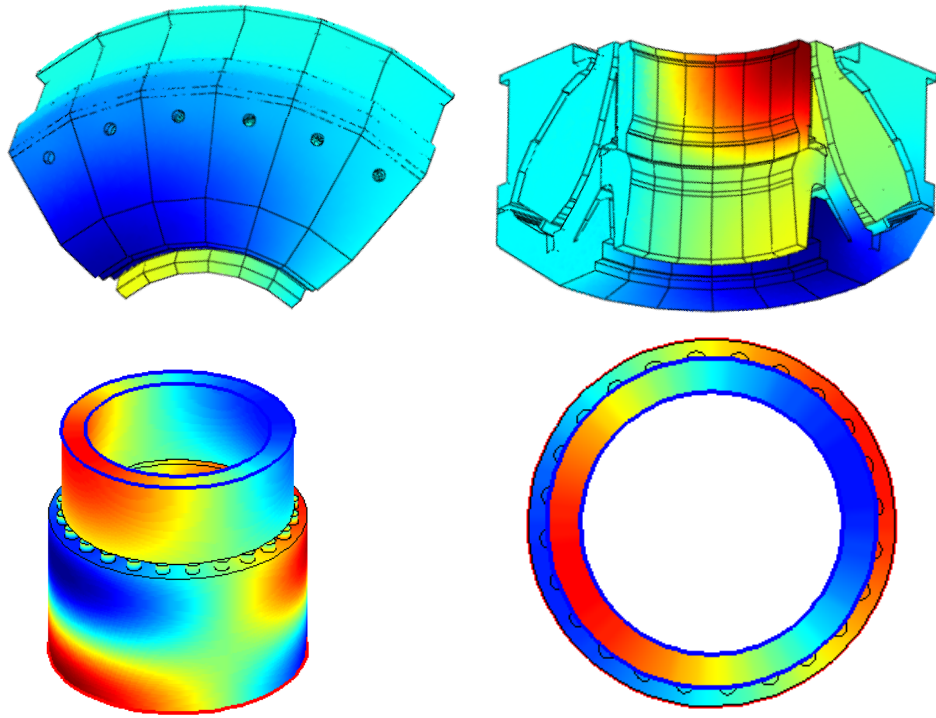


Figure 5.22 - Mode shape for the mode $n = 1$, obtained at 150.4 Hz with COMSOL (top) and 150 Hz with LOMTI (bottom).

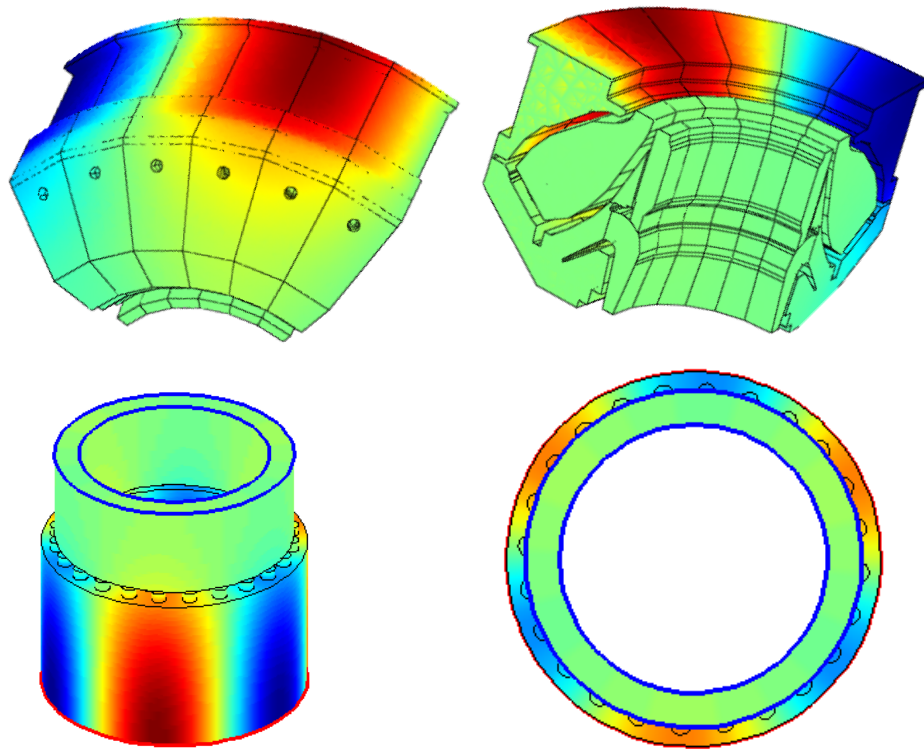


Figure 5.23 - Mode shape for the mode $n = 3$, obtained at 150.5 Hz with COMSOL (top) and 152 Hz with LOMTI (bottom).

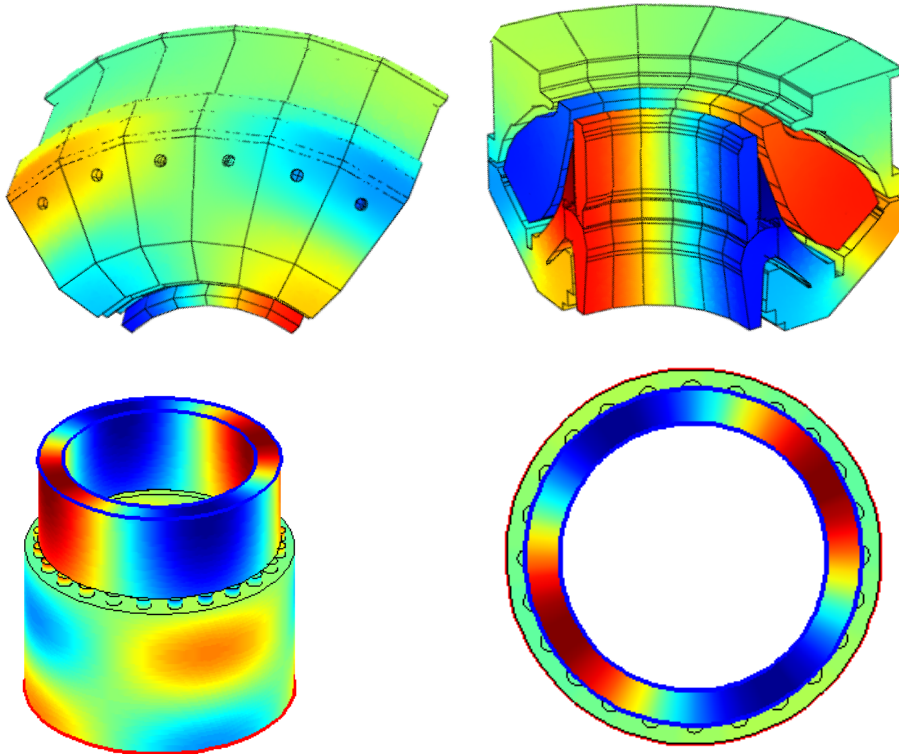


Figure 5.24 - Mode shape for the mode $n = 2$, obtained at 193 Hz with COMSOL (top) and 191 Hz with LOMTI (bottom).

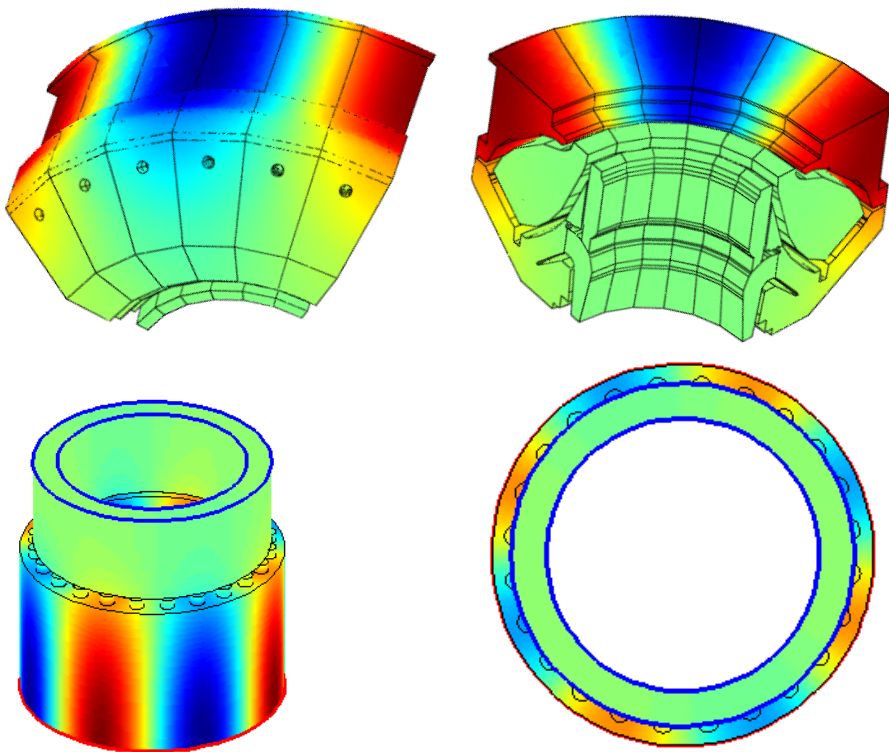


Figure 5.25 - Mode shape for the mode $n = 4$, obtained at 196 Hz with COMSOL (top) and 200 Hz with LOMTI (bottom).

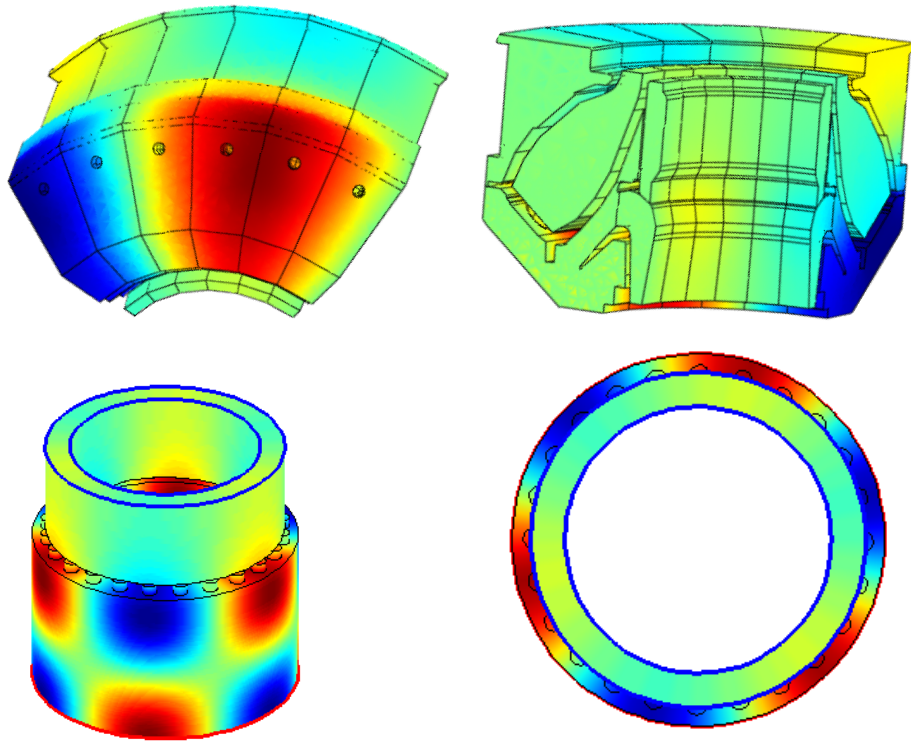


Figure 5.26 - Mode shape for the mode $n = 3$, obtained at 202 Hz with COMSOL (top) and 196 Hz with LOMTI (bottom).

All in all, 11 of the 16 modes obtained with COMSOL have been found with LOMTI, for frequencies close to those obtained with COMSOL. This means that 5 of the COMSOL modes have not been detected. Their mode shapes are displayed in figures 5.27 and 5.28. Examining the 3 modes in figure 5.27, it is clear why LOMTI has not detected them.

These modes are indeed confined in a very small corner of the plenum, at a very small length-scale, so they could not – and should not – have a correspondent mode in the lumped parameter approximation. Considering their location in the plenum, they are anyway very unlikely to yield humming. It is less clear why the 2 modes in figure 5.28 have not been found. These two modes are clearly plenum modes and there is no obvious reason why these modes should not be detected when the other plenum modes are. A solution could be to divide the plenum in LOMTI in several ducts, as explained above for the chamber, in the hope that these modes would thus emerge. It is very significant, nonetheless, that all the combustion chamber modes are present in LOMTI's computations.

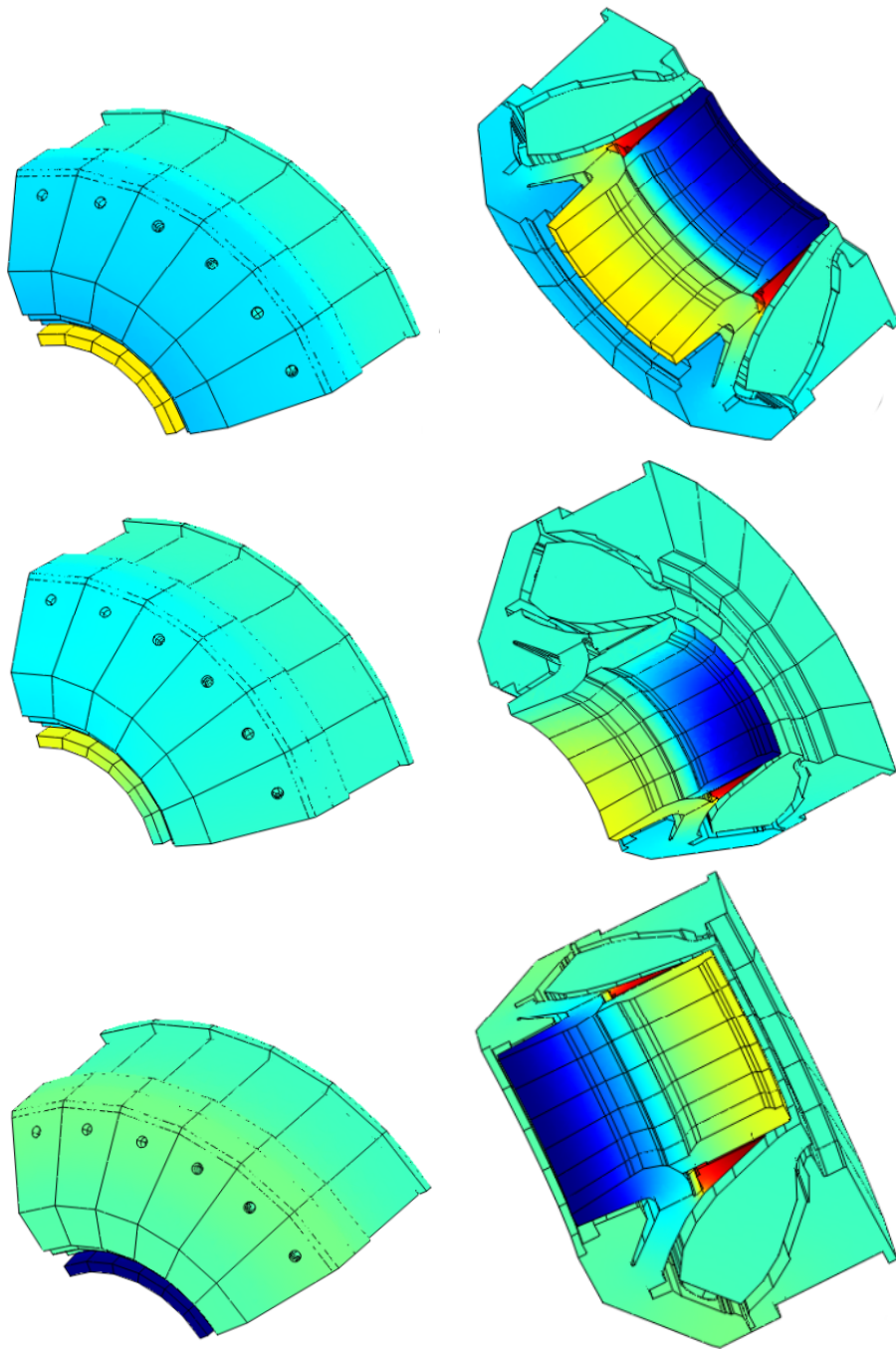


Figure 5.27 - Mode shape of the modes obtained with COMSOL at 165, 188 and 206, and not detected with LOMTI.

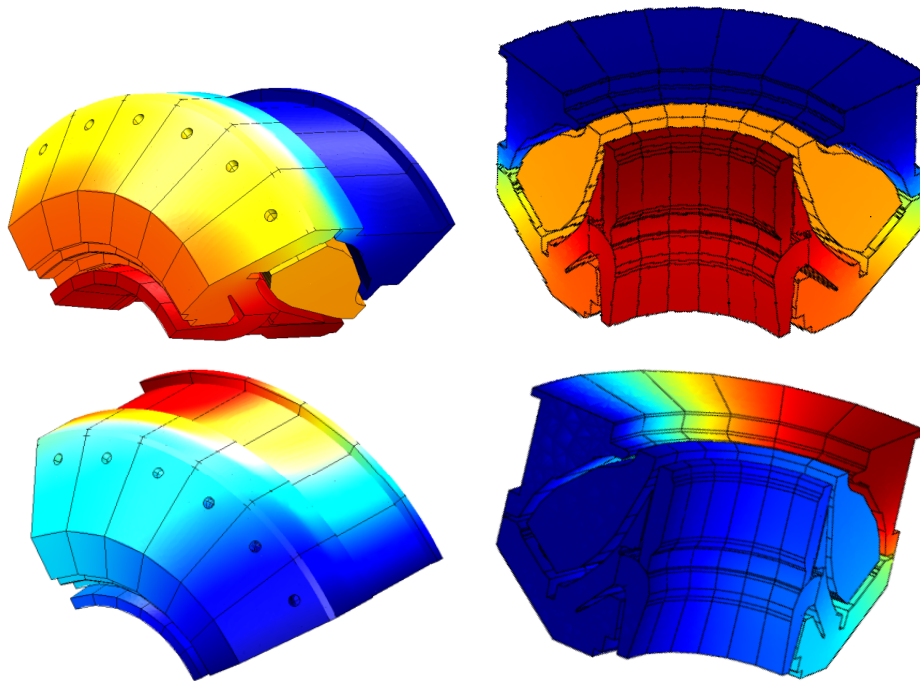


Figure 5.28 - Mode shape of the modes obtained with COMSOL at 53 and 60, and not detected with LOMTI.

Figure 5.29 summarizes the results, highlighting the frequencies obtained/not obtained with LOMTI in the optimal configuration.

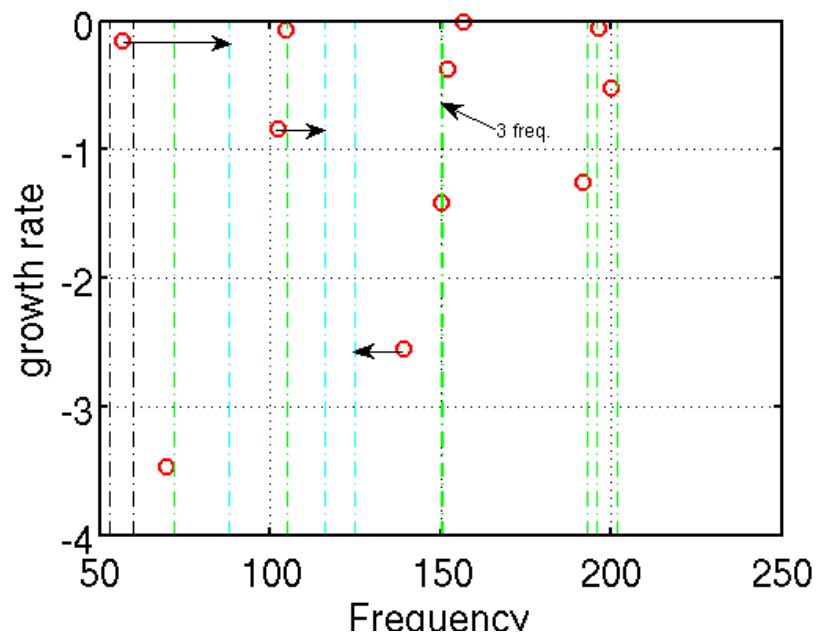


Figure 5.29 - \circ : LOMTI modes in the optimal configuration; $- \cdot - \cdot -$ COMSOL modes with very good agreement; $- \cdot - \cdot -$ COMSOL modes with worse agreement; $- \cdot - \cdot -$ COMSOL modes undetected

5.6 Comparison between COMSOL and LOMTI with a switched on flame

Once the geometry is fixed we are able to perform a further comparison with a switched on flame with reasonable confidence. Again we have to set the same boundary conditions and operating parameters between the two approaches. Moreover the same flame transfer function is to be used in order to compare results. Differing from the usual approach the reference point for this equation is now chosen at the beginning of the combustion chamber. This does not imply that the reference is placed just at the flame because in COMSOL the flame is not modelled as a flat sheet but it is a three-dimensional surface evolving into the combustion chamber. The κ - τ model reads:

$$Q'(t) = -\frac{\beta \bar{\rho} c^2}{\gamma - 1} u_3'(t - \tau), \quad (5.1)$$

where the $\kappa - \beta$ relation is:

$$\kappa = \frac{\beta \bar{\rho} c^2 \bar{Q}}{\bar{u}(\gamma - 1)}.$$

In the present settings, a value of $\beta = 0.2$ is equivalent to $\kappa = 1$. The effective value of the coefficient in the transfer function is significantly affected by \bar{Q} that has to be tuned with the Mach number in order to obtain the proper flame temperature. Therefore it is not strictly required that the value of κ in LOMTI equalize the value of $-\beta \bar{\rho} c^2 \bar{Q} / [\bar{u}(\gamma - 1)]$ present in COMSOL. On the contrary the value of τ has a different meaning because it represents the time the perturbations take to travel from the beginning of the combustion chamber to the flame located in a position internal to the chamber itself. In previous work the time lag represented only the time necessary to travel through a premixer.

We have just argued that the approach used in COMSOL is very different from LOMTI's. Furthermore the temperature field is not uniform in each duct and thus it is possible to model a three dimensional flame front with COMSOL as shown in figure 5.30. Even though the flame obtained from a RANS simulation is not completely reliable since turbulence affects significantly the reaction rate, the difference from the thin flat flame used in LOMTI and the spatially distributed temperature field used in COMSOL is evident.

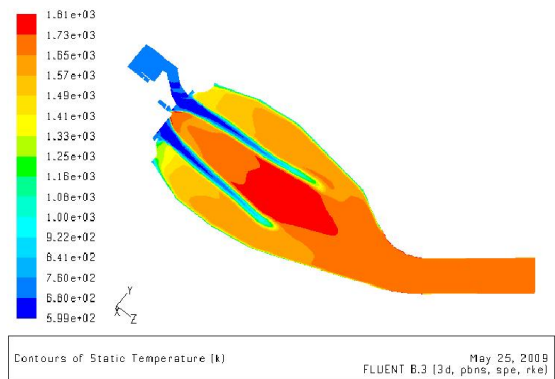


Figure 5.30 - Temperature field from a RANS simulation.

In table 5.7 results obtained matching all the parameters present in LOMTI and COMSOL are shown.

Number	COMSOL	LOMTI	Agreement without flame
1	52+i	-	undetected
2	58+i	-	undetected
3	84+i	54-130i	good
4	90	48+45i	bad
5	102+5i	103-27i	good
6	112-48i	142+42i	bad
7	121-i	118+45i	bad
8	147+3i	149+2i	good
9	144+9i	150+4i	good
10	155-16i	157+16i	good
11	164+3i	-	undetectable
12	187+2i	-	undetectable
13	192	188-85i	good
14	198+20i	201+18i	good
15	201-i	186+44i	good
16	206+i	-	undetectable

Table 5.7 - Comparison between LOMTI and COMSOL. The first column contains COMSOL results from [25]. The second one shows LOMTI results with $\beta = 1$. The last column describes the agreement obtained that particular modes in the case without flame of the previous section. Blue values are those likely to have an agreement between the two different tools even with a switched on flame.

Computational time required is very high at low Mach number since the values of the determinant become very large or very small, far from zero growth rate. A campaign looking for the best value of β would be very time consuming since very small frequency domains should be explored in many successive steps. From preliminary studies it is known that this problem is due to the low value of the Mach number. As already done for simpler geometries let us analyze the influence of the Mach number on eigenfrequencies. Results in figure ?? show that the mean flow could be neglected as a first approximation. On the other hand the presence of mean flow generates a significant speed up in the computations, and, given the fact that the results are but mildly affected by the presence of a mean flow, it becomes advantageous to include it, in any case.

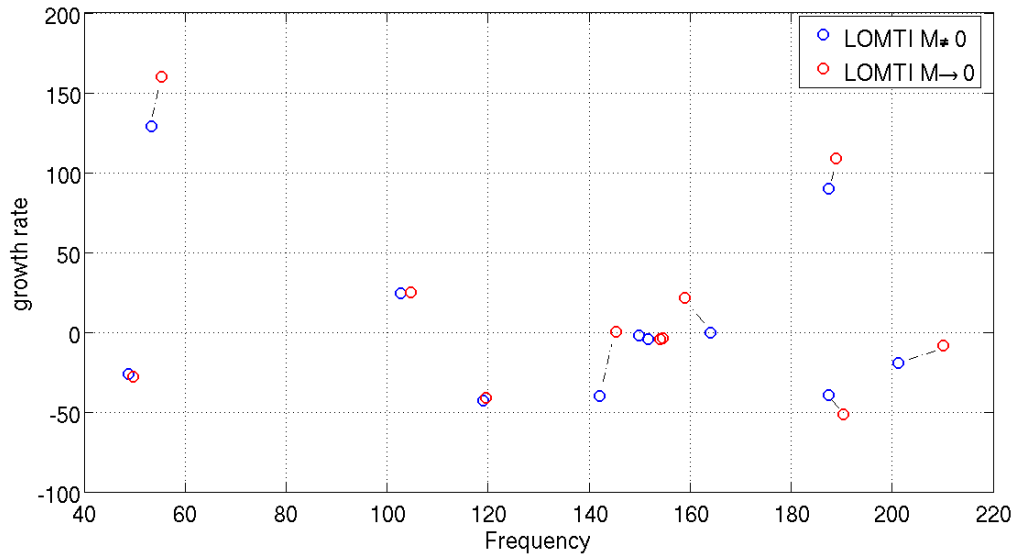


Figure 5.31 - Comparison between low Mach number and non zero mean flow ($\tau = 7ms$, $\beta = 1$, no CBO's).

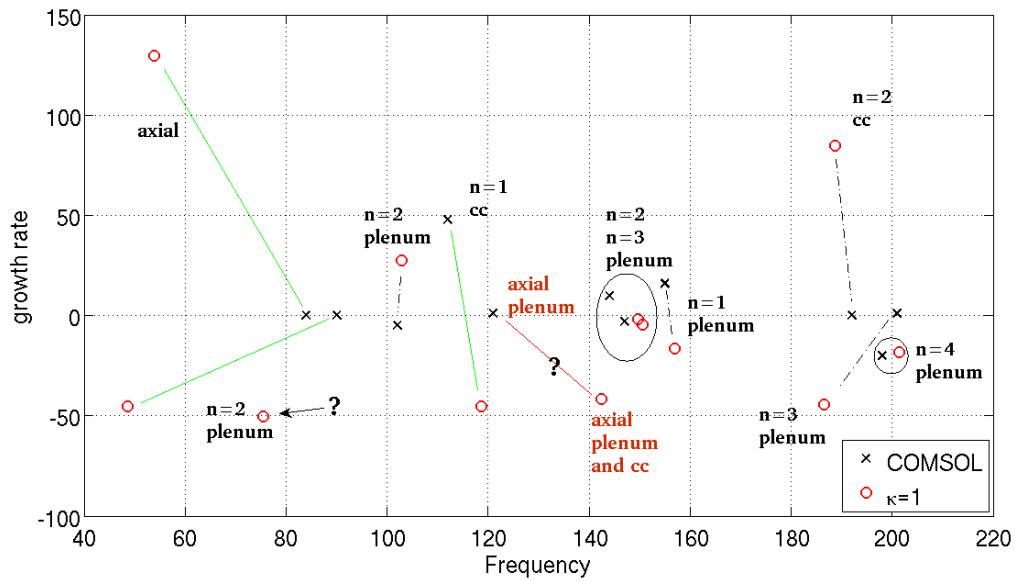


Figure 5.32 - Comparison between LOMTI ($\tau = 7ms$, $\beta = 1$, no CBO's, non zero mean flow) and COMSOL [25]. Some of the azimuthal modes have also an axial component.

It is now possible to search for the best value of β which provides the best match between the two approaches. Since the flame is located in two different points and have different thickness in the two models, the value of κ should not be the same. In fact the best agreement shown in figure 5.33 is obtained for a value of $\beta = 0.2$ (LOMTI) instead of $\beta = 1$ (COMSOL).

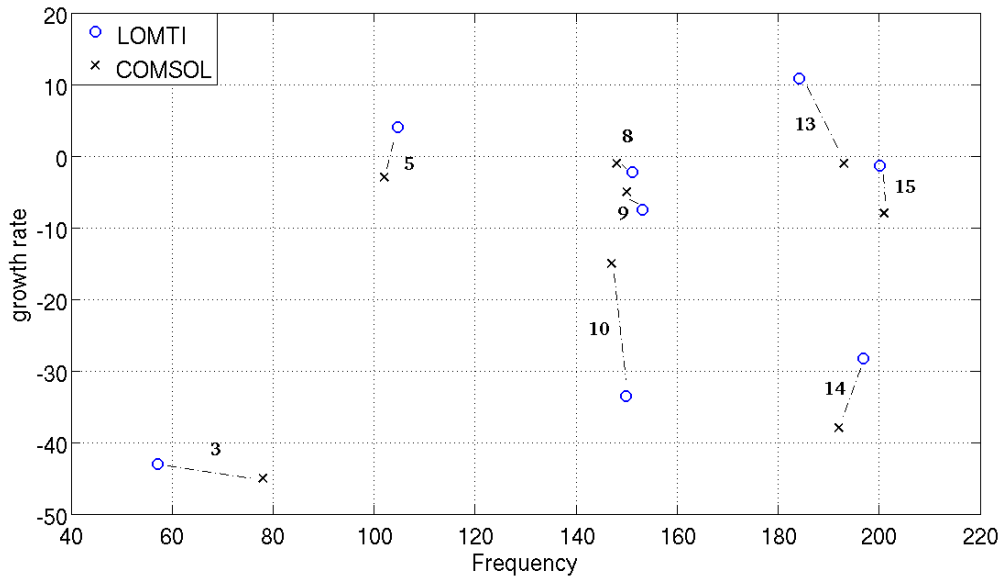


Figure 5.33 - Comparison between COMSOL results obtained in [25] with $\tau = 7ms$ and LOMTI ($\tau = 7ms$, $\beta = 0.2$, no CBO's, non zero mean flow).

Moreover, small variations of β and τ significantly modify several eigenfrequencies. We are forced to infer that such a transfer function is too weak to represent a complex configuration like a gas turbine combustor because the still arbitrary choice of flame parameters strongly affects results making them fairly unreliable. Things could be possibly improved if we could consider τ and β (or κ) as a function of ω , possibly using LES results from CERFACS. See section 6.5 for more on this point.

Chapter 6

Parametric studies

Once the geometry is fixed we are able to take advantage of LOMTI's features. Let us try to assess the effect of important parameters present in the model. These parameters are:

- combustion chamber size (length and radius),
- flame model's parameters κ - τ ,
- flame model's reference point,
- flame model itself.



Simulations are performed with the real gas turbine geometry and switched on flame perturbations. The configuration used is shown in figure 6.1. This set up has been experimentally proven to be the best configuration concerning the appearance of thermoacoustic instabilities.

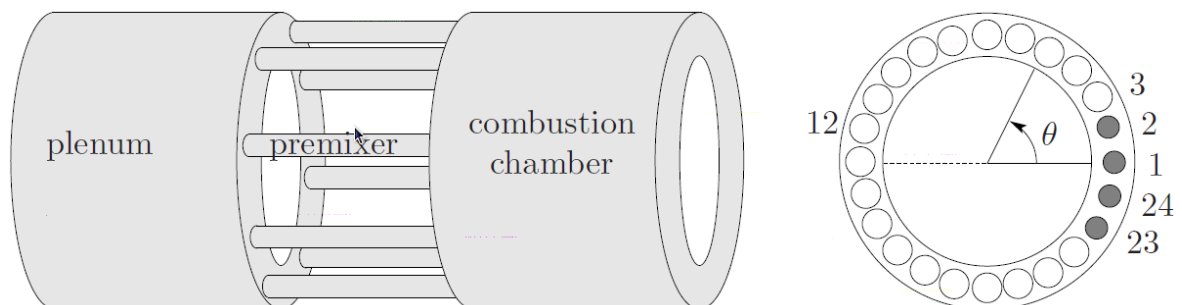


Figure 6.1 - CBO's configuration in AE94.3A gas turbine (not to scale).
Burners 1, 2, 23, 24 are without CBO's.

6.1 Combustion chamber size

Even if there is no real possibility to straightforwardly change the entire geometry of the annular combustor, the influence of general geometrical values, such as plenum length and radius, has just been detected in chapter 5 while calibrating the model on COMSOL's results. However for real configuration (20 *CBO's* and flame perturbations) the influence of combustion chamber geometry is analyzed in figure 6.3 and 6.4. This study has been performed in order to gain information about future developments of the combustion chamber geometry.

Analyzing figure 6.2, the new model of combustion chamber (A5) is longer than the previous one (A4) and its mean radius is smaller. Concerning its thickness no sensible differences are detected. Furthermore, the thickness d affects significantly only the mean flow parameters; in the eigenmodes' evaluation d is always multiplied by the pertinent radius so that its effect can be incorporated in the variations of the chamber mean radius.

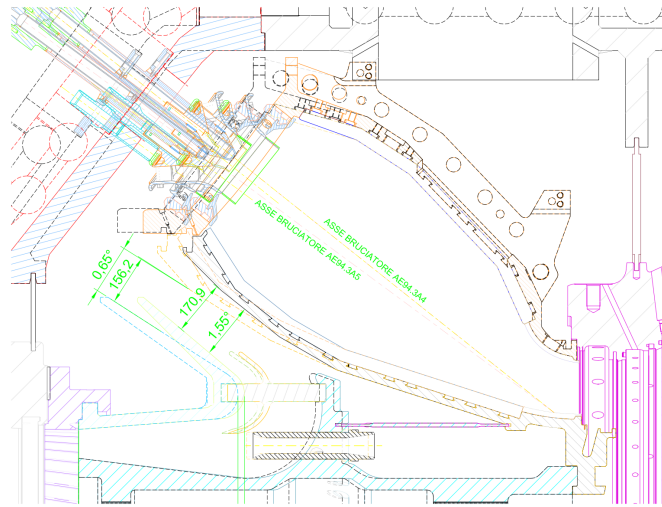


Figure 6.2 - Comparison between A4 and A5 combustion chambers.

In order to obtain sensible variations of the eigenmodes, the length and radius of the chamber have been modified beyond the real possibilities to change the real geometry. The results for varying lengths and radii of the combustion chamber are shown in figures 6.3 and 6.4 respectively.

Zooms for 'a', 'b', 'c', 'd' areas are shown in figures 6.5 and 6.6.

Modes shown with a black circle are exactly neutral and hardly detectable by our graphical approach; thus the possibility that they are only numerical singularities should be taken into account. In figure 6.7 contours of real and imaginary part of the determinant are shown: probably some numerical approximation lead to a perturbation in some regions of the complex plane that are recognized by the graphical solver as eigenmodes.

Nevertheless, even if they were real solutions, their zero growth rate allows to disregard them due to the presence of viscous forces not modelled in LOMTI that would possibly force them into the stable half-plane. Two couples of eigenmodes must be carefully tracked: one is found close to 70 Hz and the other is in the vicinity of 187 Hz . The first one seems to have only benefits with the modified geometry. The latter has

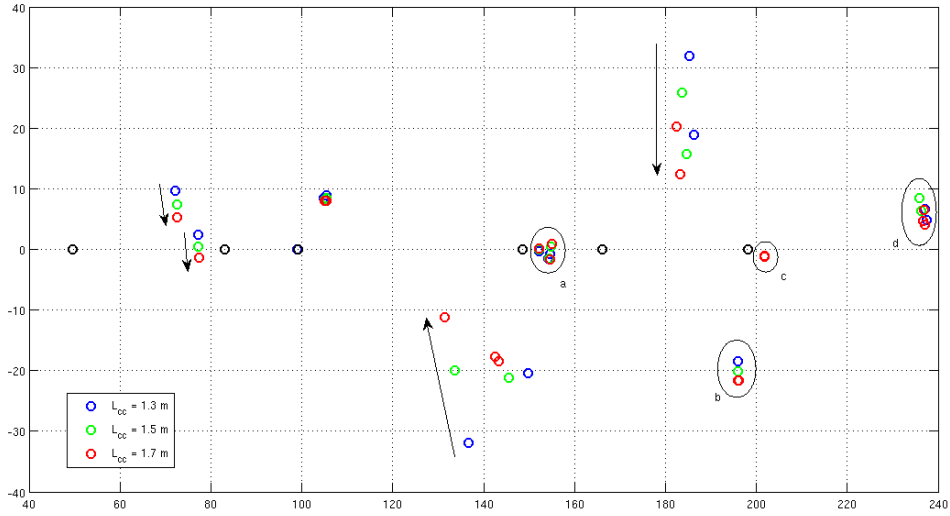


Figure 6.3 - \bullet : $L_{cc} = 1.3m$; \circ : $L_{cc} = 1.5m$; \circ : $L_{cc} = 1.7m$;

different responses for independent variations of the length and radius, thus no trend is easy to detect. A further study has been performed considering only this mode, and by varying simultaneously length and radius. In figure 6.8 it is shown that a reduction in radius together with an increase of length yield an enhancement of the amplification factor of this unstable mode.

This parametric analysis has been carried out to infer trends. Since there are only small changes from the A4 to the A5 gas turbine models, we expect that the effects on thermoacoustic stability modes are minor. Unstable modes are too far from zero growth rate to be damped only thanks to an increase of 4% of the combustion chamber length.

6.2 Flame parameter τ

It has already been stated how critical could be the flame model chosen. The closure equation that describes the interactions between heat release and perturbations has been discussed in chapter 4. In this section we want to point out its importance and consistency focusing on the κ - τ model used so far.

Simulations for the complete complex plane would be highly time expensive and probably would not yield remarkable results. Thus only the $n = 2$ mode at $187 Hz$ will be tracked during τ variation. The choice of this mode is due to its relevance in limited experimental data at disposal. In fact it is known that instabilities arise in the combustion chamber in azimuthal direction at frequency not far from $170 Hz$, therefore this mode is the most suitable to fit the vibrations noticed in real gas turbine.

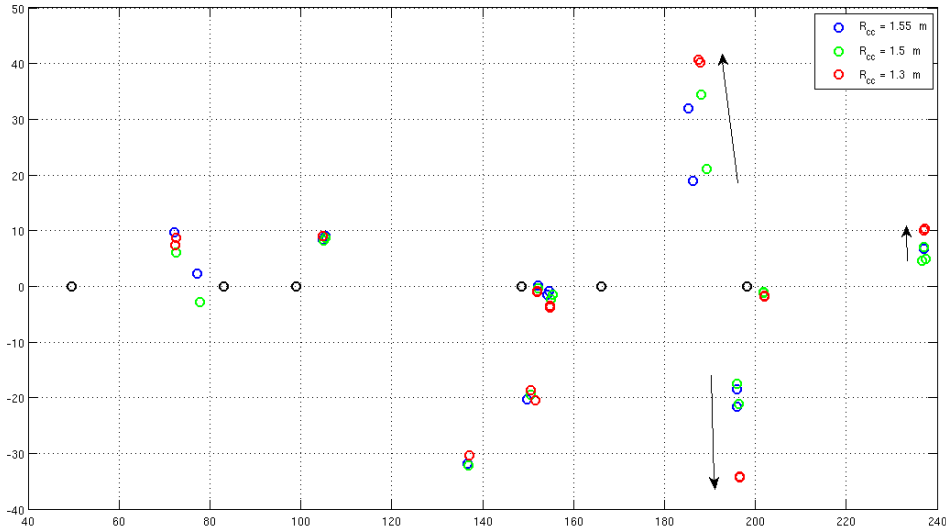


Figure 6.4 - \circ : $R_{cc} = 1.55m$; \circ : $R_{cc} = 1.5m$; \circ : $R_{cc} = 1.3m$;

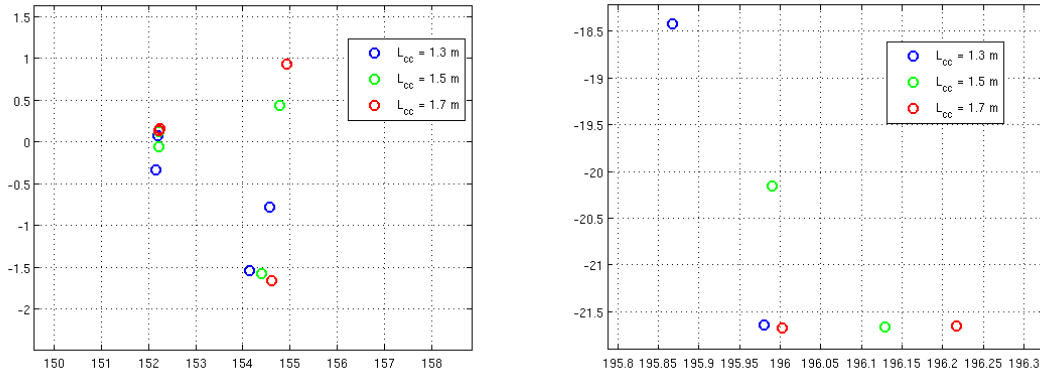


Figure 6.5 - Zoom for area 'a' and 'b'

The way to choose the time lag is a very hard task. Simulations run at CERFACS on premixers used in *AE94.3A* gas turbine have provided a value for an acoustical τ close to 1 *ms*. The value used so far is 7 *ms*. This was evaluated from:

$$\tau = \frac{L_{premixer} + L_{CBO}}{U_{premixer}} = \frac{0.142m + 0.054m}{68m/s} \approx 3ms;$$

however, since swirl is very high in the premixers, the flow take more time to reach the flame's surface, that already is not located at the end of *CBO's* but a little downstream. Thus time lag was chosen higher then 3 *ms* in order to represent this highly swirled flow.

In figure 6.10 the influence of τ is shown. A singular result occurs: indeed there are two couples of eigenmodes for each value of τ . Mode shapes are so similar that they can be easily confused with one another (in effect from a previous analysis modes for

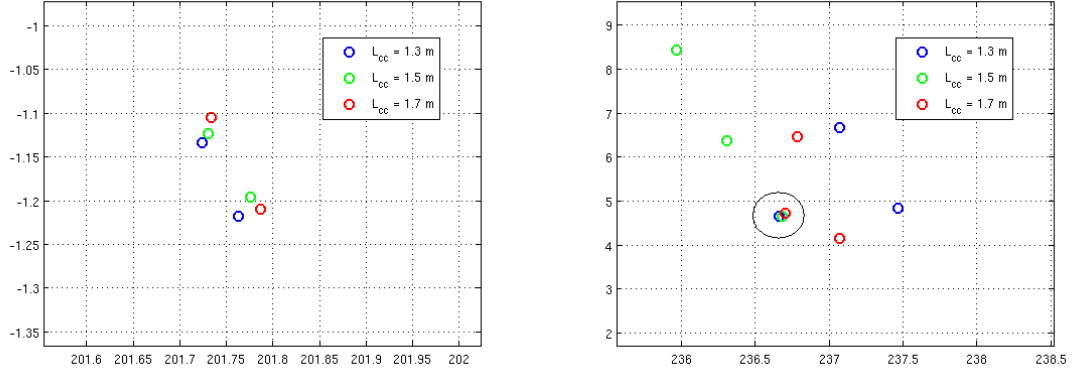
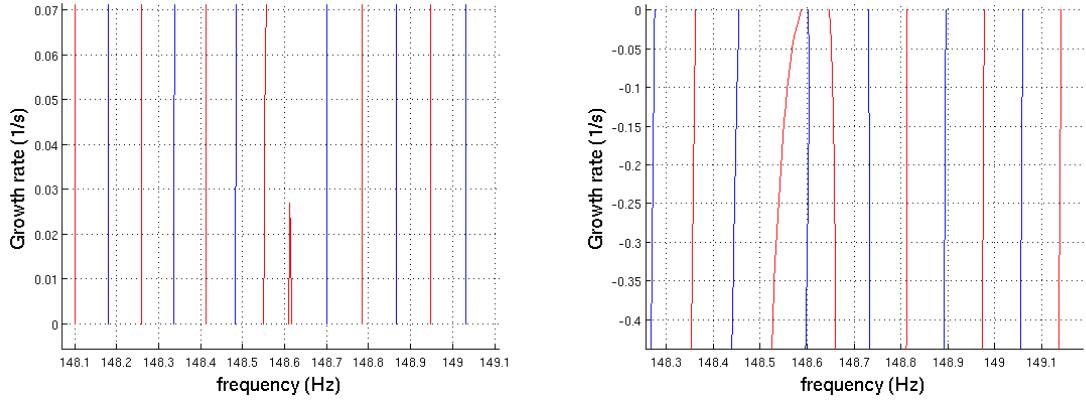


Figure 6.6 - Zoom for area 'c' and 'd'

Figure 6.7 - —: $real\{det(X)\}$. —: $imag\{det(X)\}$. Positive and negative half-plane

$\tau = 7\text{ ms}$ and $\tau = 1\text{ ms}$ were recognized as being the same). This fact generates further doubts on the consistency of the thin flame approximation.

We could be induced to think that the value of a specific eigenfrequency $\omega = \omega_r + i\omega_i$ should be unchanged if we choose two values of τ shifted only by the period of that eigenfrequency, i.e. $T = 2\pi/\omega_r$. Performing some easy algebraic passages it becomes clear that this statement has no mathematical confirmation when modes are not neutral. Imposing $\tau_1 = \tau$ and $\tau_2 = \tau - 2\pi/\omega_r$ we seek for the condition that allows to write:

$$e^{i\omega(t-\tau_1)} = e^{i\omega(t-\tau_2)}$$

$$e^{i\omega(t-\tau)} = e^{i\omega(t-\tau)} \cdot e^{i\omega \frac{2\pi}{\omega_r}}$$

This expression becomes an identity only if $\omega = \omega_r + i\omega_i = k\omega_r$ where we have defined $k \in \{0, 1, -1, 2, -2, \dots\}$. Thus ω_i must be zero and modes must be neutral in order to assert that τ could be shifted by the specific period in order to recover the same eigenmode.

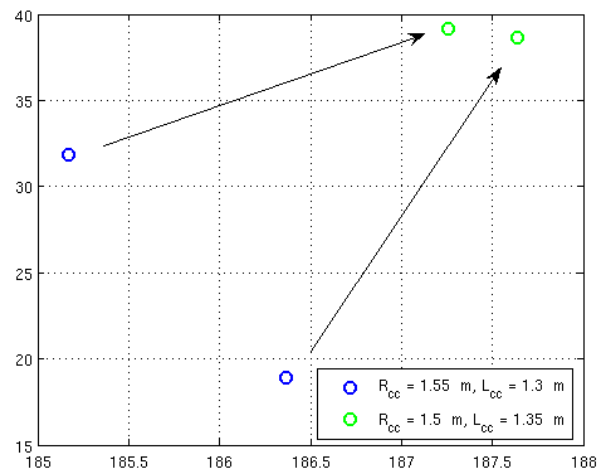


Figure 6.8 - Mode at 187Hz with length and radius simultaneously varying.

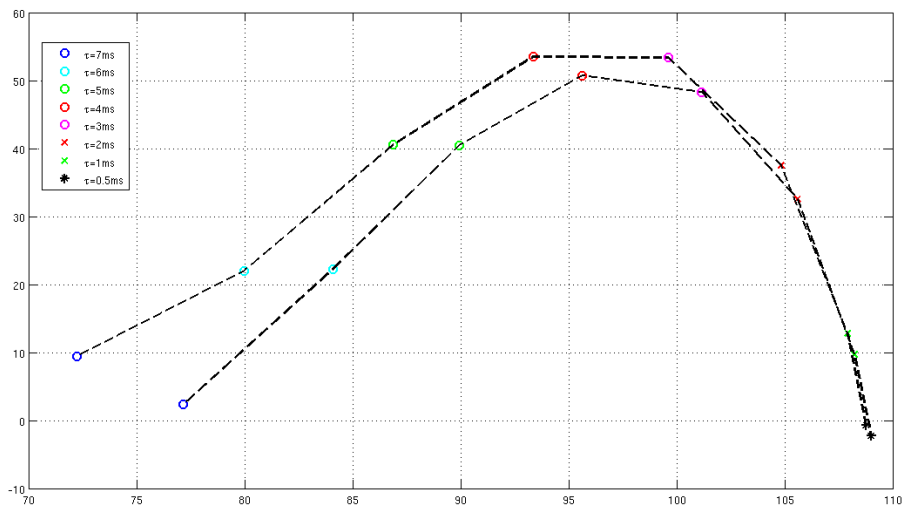


Figure 6.9 - Modes near 90Hz.

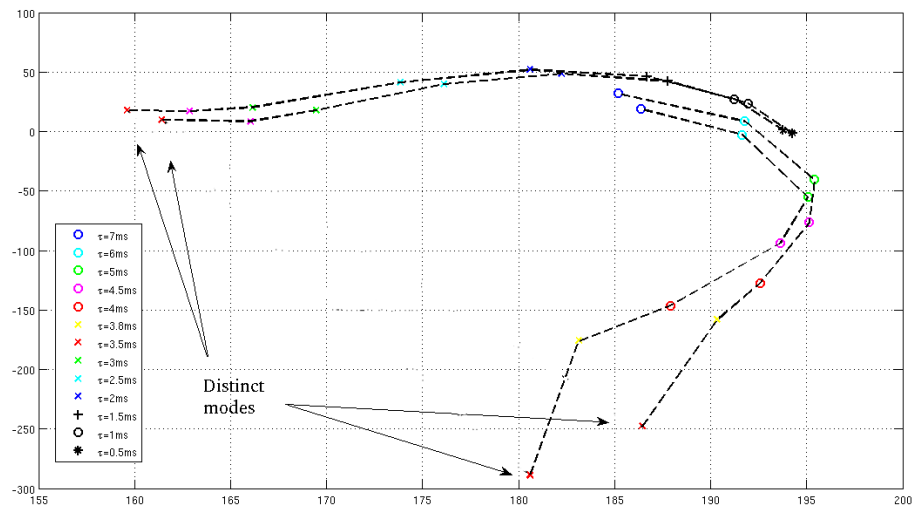
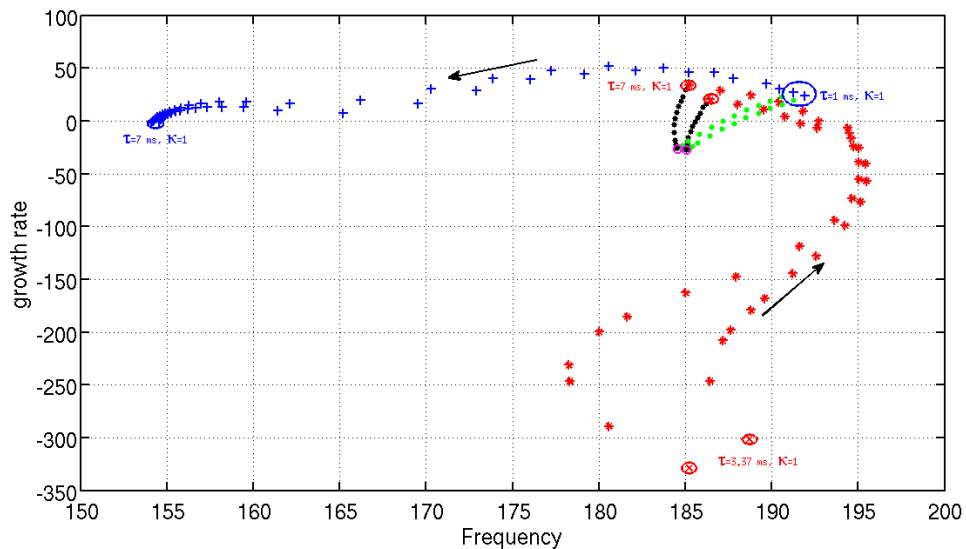


Figure 6.10 - Modes near 170Hz.

Further simulations have been done for different values of κ demonstrating that for $\kappa = 0$ and $\tau = 1 \text{ ms}$ or $\tau = 7 \text{ ms}$ these couple of modes meet in a single place: this results does not allow to state that this splitting is due only to the flame transfer function chosen because for $\tau = 4.5 \text{ ms}$ this fact does not occur. The strong sensitivity of eigenmodes to the flame parameters does not allow to rely on any results obtained in terms of frequency and growth rate but only to infer trends.

Figure 6.11 - Modes near 170Hz for different values of κ .

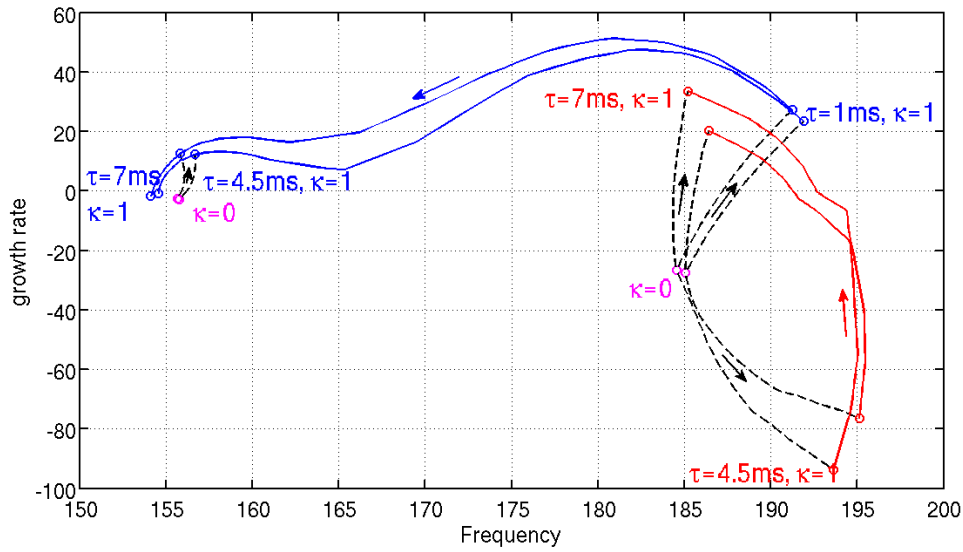


Figure 6.12 - Modes near 170Hz for different values of κ tracked from different values of τ .

6.3 Flame parameter κ

The influence of κ is evaluated in the following. No general trend arises from these results. Modes near 150 Hz ($n = 1, 2, 3$ located in the plenum) are weakly dependent on the flame transfer function parameters.

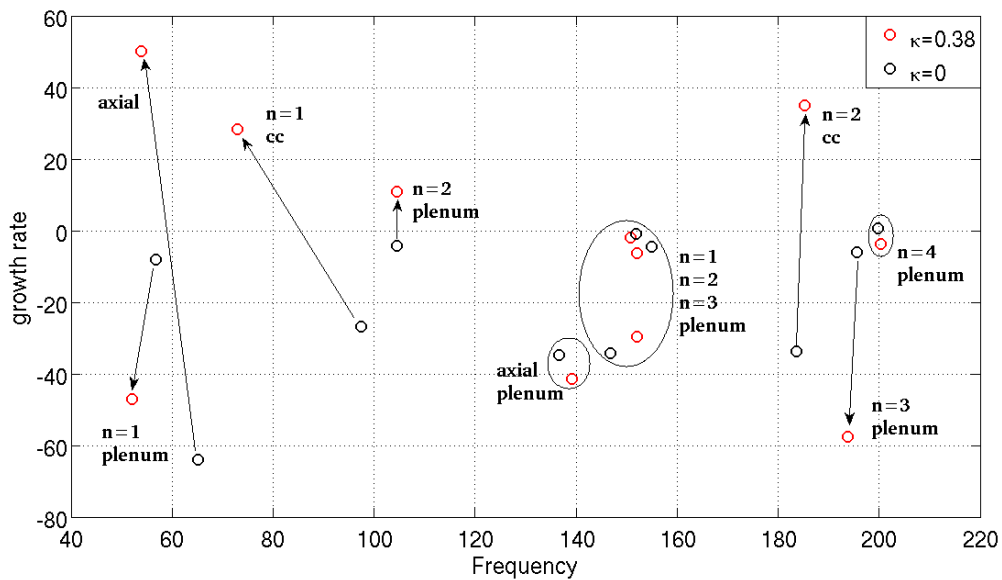


Figure 6.13 - κ .

6.4 Transfer function's reference point

To achieve information about the problem discussed in section 4.6, we have also performed a parametric study on the distance L_{i-f} between the flame and the reference point where perturbations present in the transfer function are evaluated. Only three different eigenmodes are tracked from a reference point located exactly at the flame (end of premixers) and another one located at the premixer entry. These modes are chosen according to their representativeness. Both axial and azimuthal modes are present and the latter have been chosen among two different classes: the first is strictly dependent on flame transfer function parameters and the second seems to be quite independent from these ones. Surprisingly, no difference results from very different reference points. This is a good news since it demonstrates that the choice of the reference point does not influence so much the results. This is probably due to the fact that pressure mode shapes in the premixers do not undergo great changes in their amplitude along the duct.

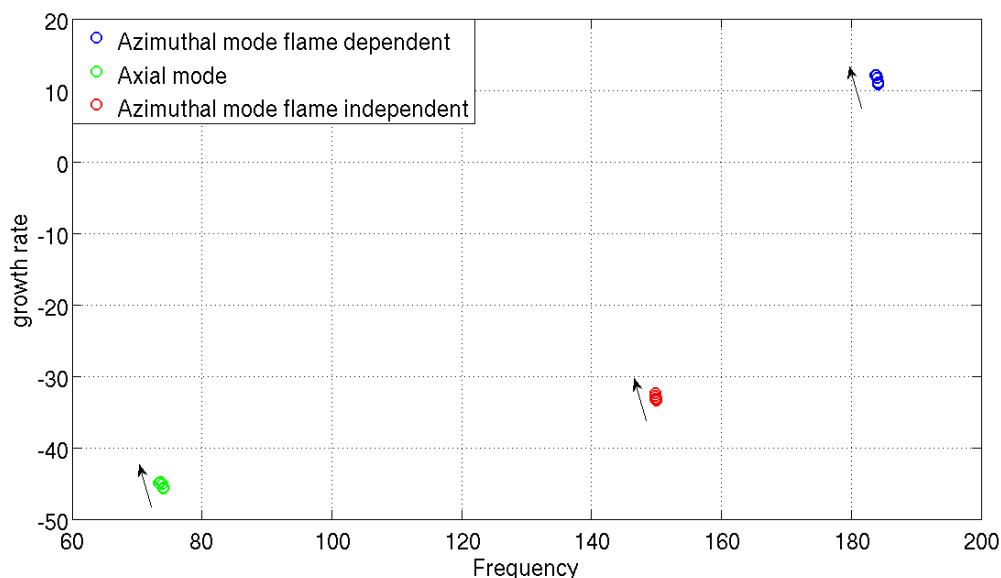


Figure 6.14 - *Eigenfrequencies for increasing L_{i-f} from zero to the entire premixer's length.*

6.5 Influence of the transfer functions

Finally, a comparison between different transfer functions is carried out. Let us first analyze the differences between equation (6.1) and (6.2). Again, only three representative eigenmodes are chosen. The frequency at 150 Hz is clearly not much influenced by flame transfer function choice as shown in figure 6.15. Since in every simulation it has been noticed to not vary significantly its position we are induced to consider it as a geometrical mode. The same consideration is valid also for all the other sub-stable modes.

$$\frac{Q'}{Q} = \kappa \frac{\dot{m}'}{\dot{m}} e^{-i\omega\tau} \quad (6.1)$$

$$\frac{Q'}{Q} = \kappa \frac{u'}{u} e^{-i\omega\tau} \quad (6.2)$$

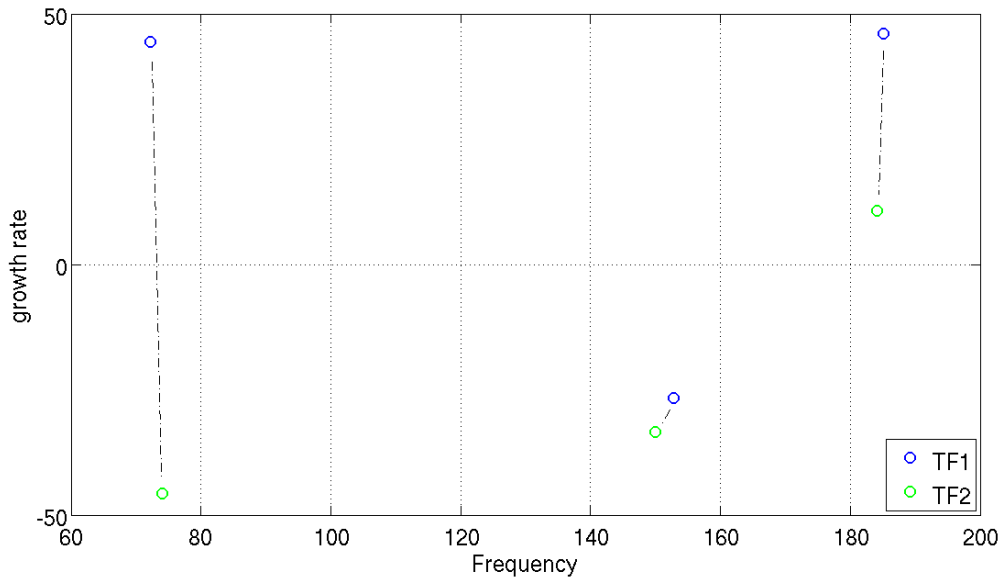


Figure 6.15 - *TF1: equation (6.1); TF2: equation (6.2).*

The evaluation of the proper κ and τ is a challenging task. LES simulations performed at CERFACS provide values of these parameters depending on the frequency.

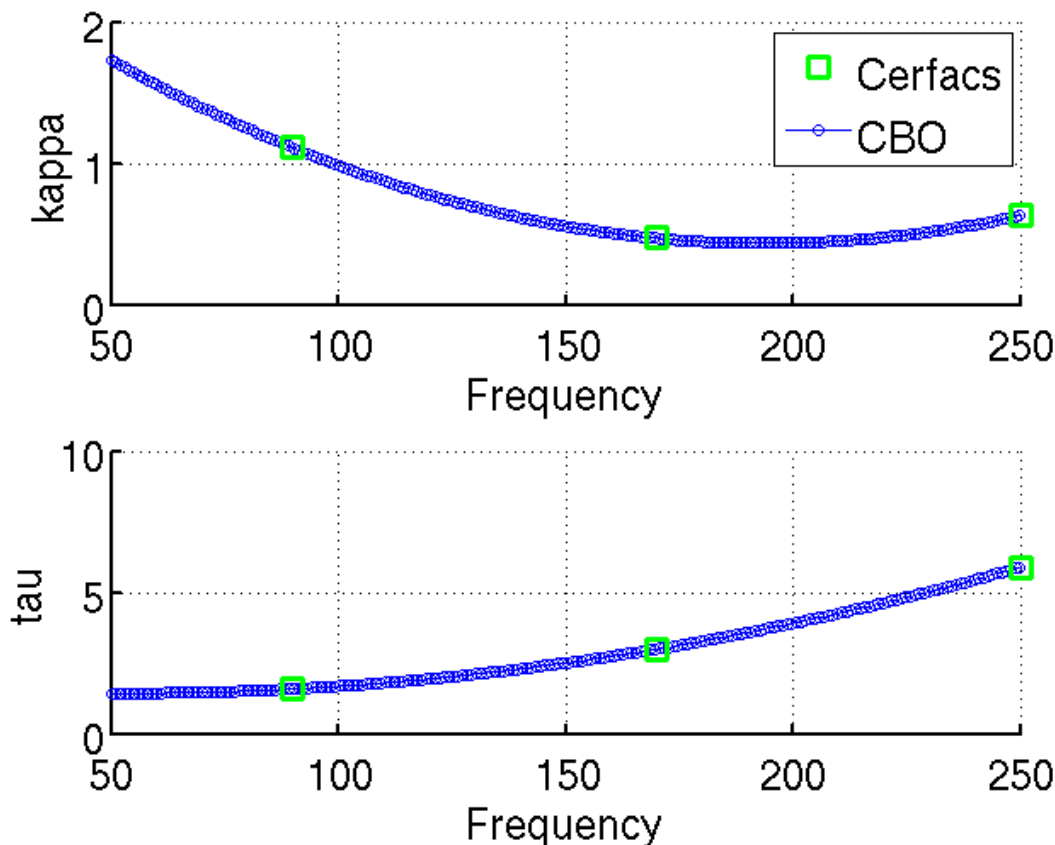


Figure 6.16 - $\kappa - \tau$ values calculated at CERFACS for burners with CBO's. Green squares are numerically computed values and the blue line is a parabola fitted on these values.

This different approach inevitably leads to a new aspect of spectra. Let us first consider figure 6.10. When τ varies the eigenfrequency shifts in the frequency-growth rate plane. Let us impose that when $\tau = \tau_1$ or $\tau = \tau_2$ the eigenfrequencies obtained are respectively f_1 and f_2 (let us not account for the amplification factor for the time being). If the values of $\tau = \tau(f)$ obtained at CERFACS for f_1 and f_2 are similar to τ_1 and τ_2 then two simultaneous eigenfrequencies will be detected at the same time. Since we know from experience that small τ variations imply small frequency variations this situation is not a useless but a real case that leads to something like a continuous spectrum.

This must not induce us to think that varying the value of τ could generate a sort of closed loop following one eigenfrequency. If τ varies and the eigenmode shifts somewhere the solution could generate an open path as shown in figure 6.18.

Sesta. A preliminary test was done on a different geometrical configuration. A code based on an experimental plant located in Sesta has already been implemented. This plant has the purpose to test different type of burners and gives also informations on their thermoacoustic behaviour. A scheme of this plant is shown in figure 6.17.

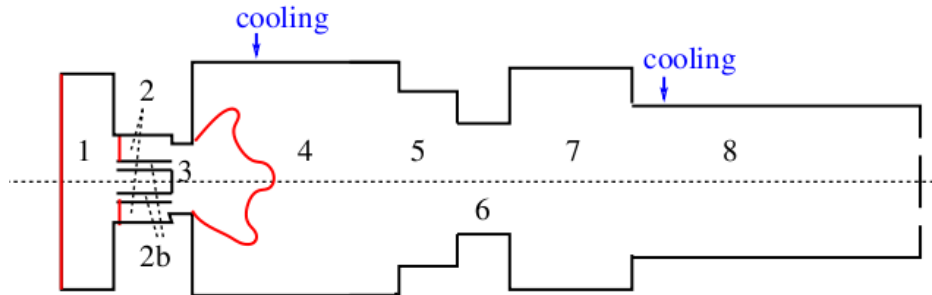


Figure 6.17 - Modelled geometry of the burner in Sesta used in LOMTI.

Considerations on continuous spectra are confirmed by results in figure 6.18 where a single eigenmode goes through the domain outlining three peaks at 65 Hz , 98 Hz and 141 Hz . During its movement, the mode shape varies continuously as confirmed by figures 6.20 to 6.22.

It could be interesting the fact that a mode at 141 Hz has just been detected in a previous test with a fixed value of $\tau = 1.59\text{ ms}$ (figure 6.19). In this test only this eigenmode was found and thus the relative continuous spectrum is easy recognizable.

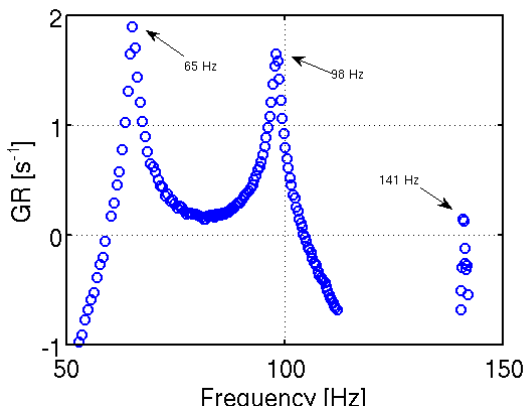


Figure 6.18 - Eigenmodes for $\kappa - \tau$ evaluated from fitting values obtained at CERFACS.

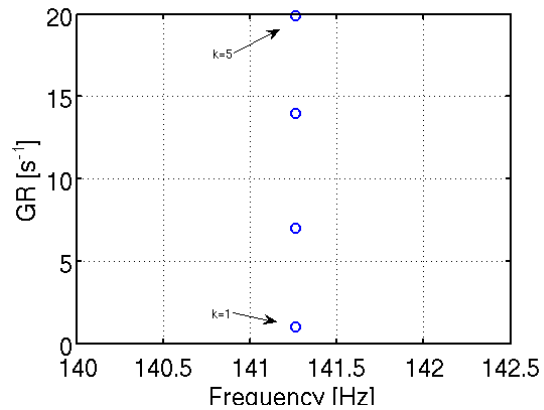


Figure 6.19 - AE94.3A eigenmodes for different values of κ and $\tau = 1.59$ from [31].

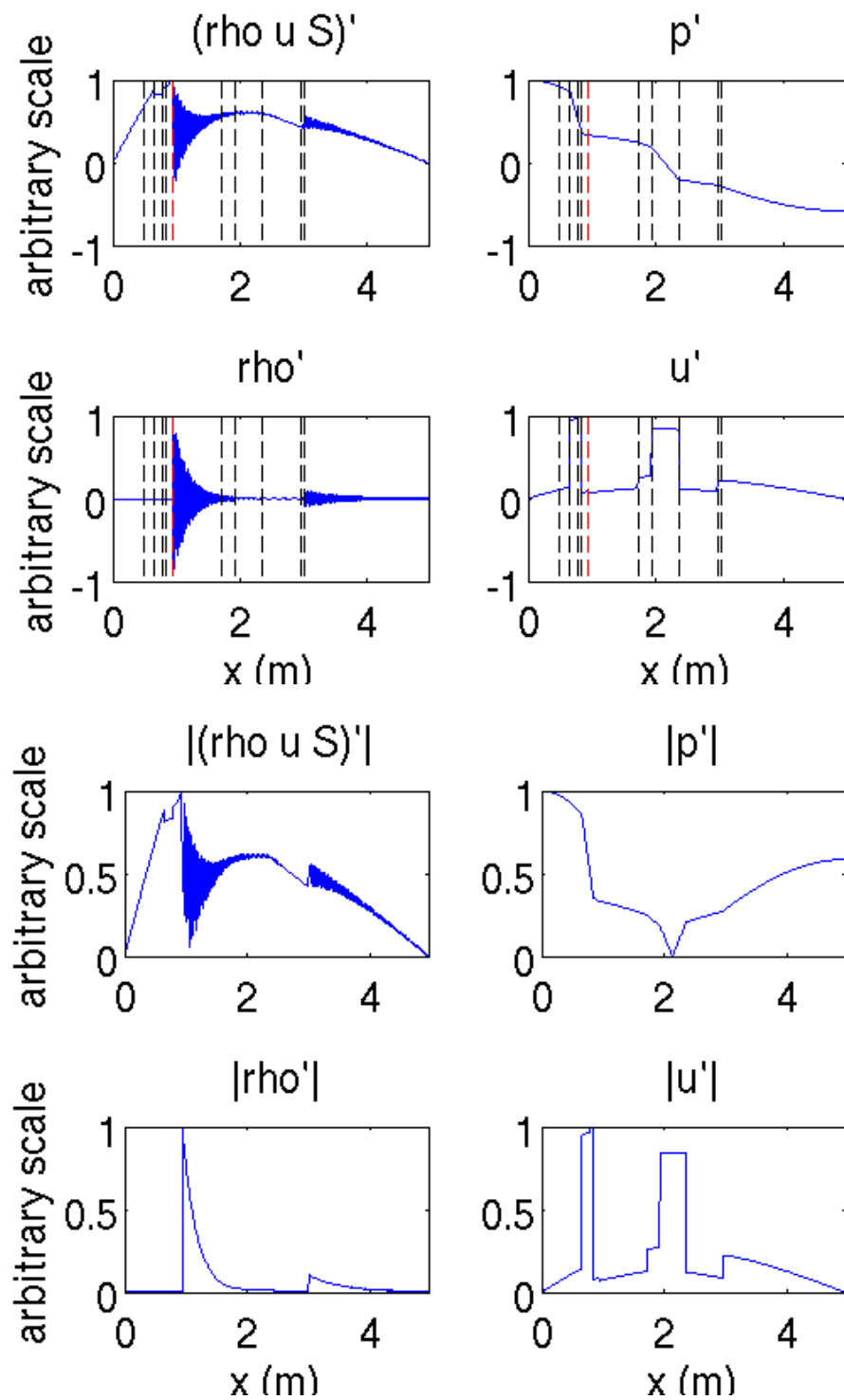


Figure 6.20 - Mode shapes for the peak at 65 Hz.

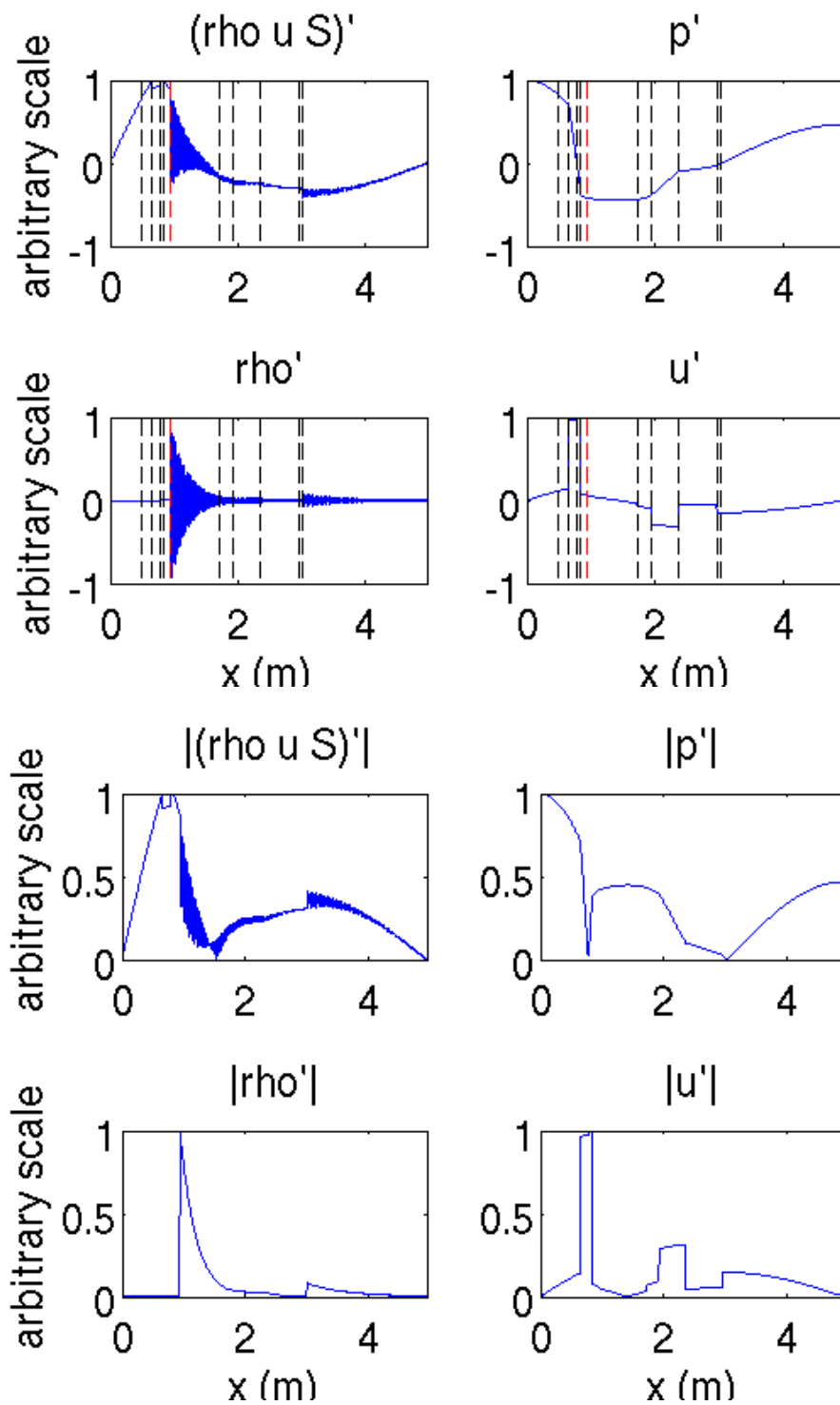


Figure 6.21 - Mode shapes for the peak at 98 Hz.

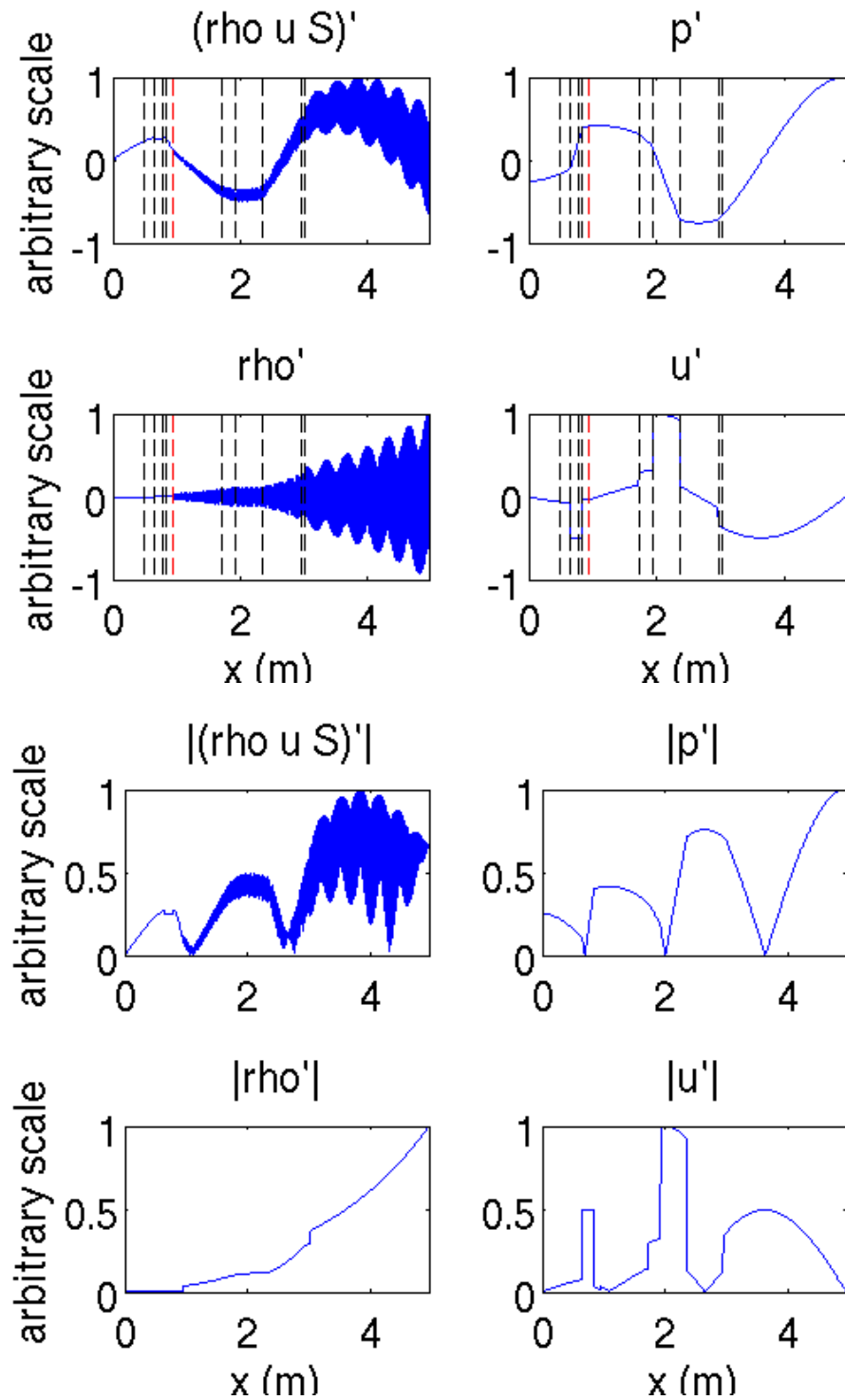


Figure 6.22 - Mode shapes for the peak at 141 Hz.

Turbine. Let us now apply the results from CERFACS shown in figure 6.16 to the present configuration of the AE95.3A turbine. The resulting spectrum is shown in figure 6.23.

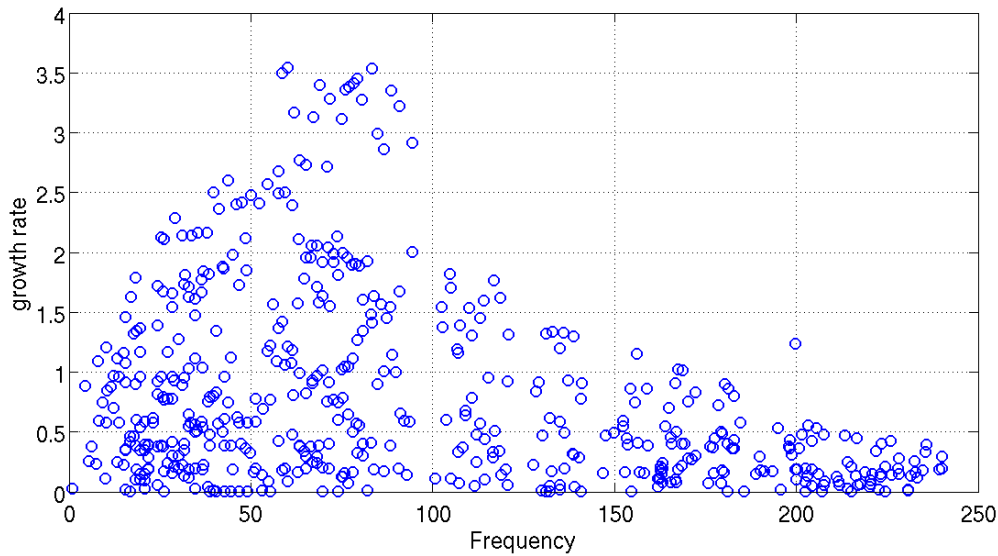


Figure 6.23 - *AE94.3A eigenmodes for $\kappa - \tau$ evaluated from fitting values obtained at CERFACS.*

Since eleven modes are present in this configuration it is clear how difficult it is to recognize continuous spectra like those observed in figure 6.18. Even if they were effectively present, the discrete computation results in a cloud of modes. Trying to plot mode shapes of some of these eigenfrequencies we are able to reproduce those observed in previous calibrations. For example, let us evaluate mode shapes for peaks at 56 Hz or at 200 Hz. They are shown in figure 6.24 and 6.25. These mode shapes are very similar to figures 5.17 and 5.25. But actually we are able to plot mode shapes for every eigenfrequency, even if it is not an eigenfrequency that renders the determinant zero; therefore in the great quantity of modes found, probably we are able to find out every mode shape we want. So we have to recognize a path for each mode in the domain in order to develop some confidence in the results.

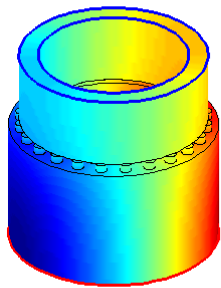


Figure 6.24 - *Mode shape for mode at 56 Hz ($\kappa - \tau$ evaluated from fitting values obtained at CERFACS).*

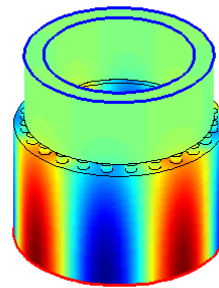


Figure 6.25 - *Mode shape for mode at 200 Hz ($\kappa - \tau$ evaluated from fitting values obtained at CERFACS).*

In figure 6.26 is plotted a comparison between results obtained with two different transfer functions. TF_2 is the usual transfer function used at CERFACS; TF_4 is the transfer function used at PoliBa for COMSOL simulations.

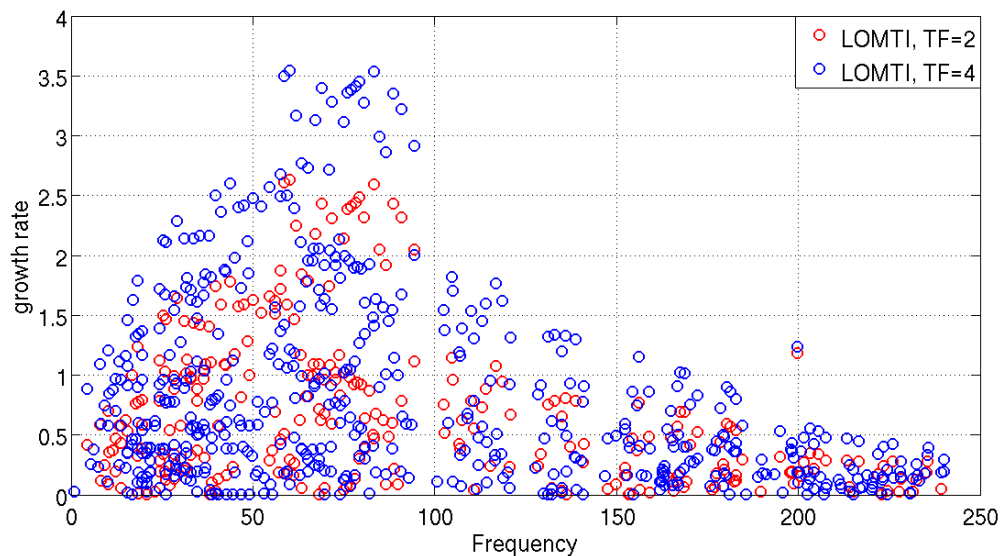


Figure 6.26 - *AE94.3A* eigenmodes for $\kappa - \tau$ evaluated from fitting values obtained at CERFACS. $TF = 2$: $Q'/\bar{Q} = \kappa \frac{u'}{u} e^{i\omega\tau}$. $TF = 4$: $Q'/\bar{Q} = -\frac{\beta \bar{\rho} c^2}{\gamma - 1} u'_3(t - \tau)$

Also in this case a cloud of modes appears rendering the identification of interesting disturbance shapes extremely difficult. The result of this study is that employing κ and τ function of ω in the code complicates things rather than clarify them.

Chapter 7

Annular ducts with non-negligible thickness

Let us consider a cylindrical duct of radius R and thickness $d < R$. The mean flow is assumed to have only axial direction ($\bar{u} \neq 0$ and $\bar{v} = \bar{w} = 0$). The expression for a generic perturbation will be:

$$G'(x, r, \theta, t) = X(x)B(r)\Theta(\theta)e^{i\omega t}$$

Acoustic waves Considering the homogeneous equation for pressure perturbation:

$$\frac{1}{c^2} \frac{D^2 p'}{Dt} - \nabla^2 p' = 0$$

separating variables (assuming $X(x) = A_{\pm} e^{ik_{\pm}x}$ and $\Theta(\theta) = e^{in\theta}$) we get the so called Bessel's equation:

$$r^2 B'' + rB + (\lambda^2 r^2 - n^2)B = 0 \tag{7.1}$$

The general solution for equation (7.1) is:

$$B(r) = c_1 J_n(\lambda r) + c_2 Y_n(\lambda r)$$

where J_n and Y_n are the Bessel functions of order n of first and second kind, shown in figure 7.1 and 7.2. Considering an annular duct, the radius never assumes values equal to zero, so both Bessel's functions have to be taken into account (c_1 and c_2 are generally non-zero).

Imposing boundary conditions in $r = R$ and $r = (R - d)$ where the radial velocity must be zero, we get an expression for the pressure perturbation:

$$p'_a(x, r, \theta, t) = A_{\pm} e^{i(k_{\pm}x + n\theta + \omega t)} B_{n,m}(r)$$

where

$$B_{n,m}(r) = \frac{dY_n}{dr}(\lambda_{n,m}R)J_n(\lambda_{n,m}r) - \frac{dJ_n}{dr}(\lambda_{n,m}R)Y_n(\lambda_{n,m}r)$$

$$k_{\pm} = \frac{\bar{M}\omega \pm \sqrt{\omega^2 - \bar{c}^2 \lambda_{n,m}^2 (1 - \bar{M}^2)}}{\bar{c}(1 - \bar{M}^2)}$$

Applying respectively the condition of isentropicity, the momentum equation and irrotationality (twice) we get:

$$\begin{aligned} \rho'(x, r, \theta, t) &= \frac{1}{\bar{c}^2} p'_a(x, r, \theta, t) \\ u'_a(x, r, \theta, t) &= -\frac{k_{\pm}}{\bar{\rho}\alpha_{\pm}} p'_a(x, r, \theta, t) \\ w'_a(x, r, \theta, t) &= -\frac{n}{r\bar{\rho}\alpha_{\pm}} p'_a(x, r, \theta, t) \\ v'_a(x, r, \theta, t) &= -\frac{i}{\bar{\rho}\alpha_{\pm}} A_{\pm} e^{i(k_{\pm}x + n\theta + \omega t)} \frac{dB_{n,m}(r)}{dr} \end{aligned}$$

Entropy waves Entropy waves generates only density (and temperature) perturbations:

$$\rho'_e(x, r, \theta, t) = \frac{1}{\bar{c}^2} A_e e^{i(k_0x + n\theta + \omega t)} E(r)$$

where $k_0 = -\omega/\bar{u}$ and $E(r)$ is an arbitrary function of the radius.

Neglecting azimuthal and radial velocity perturbations w' and v' and setting $E(r)$ equal to $B_{n,m}$ we could factorize the Bessel function $B_{n,m}$, excluding it from the computation of the determinant. Thus eigenfrequencies would not be modified, unlike the mode shapes. These assumptions are useful to avoid a radial discretization, required in order to take into account the explicit radial dependency as $1/r$ in w' .

A final code involving radial dependency has been implemented in order to check the effective influence of radial modes. From [30] we know that radial modal coupling could be neglected since it is numerically found that, while each individual resonant frequency is slightly influenced by the other modes, the overall trends are virtually unaffected: the envelopes of solutions and hence the most unstable frequencies are unaltered. Therefore, each time we search for a mode, we have to impose its radial wave number m . A simple analytical preview forces us to expect a perfect concordance between results obtained with small radial thickness and those with radial dependency imposing $m = 0$, i.e. no radial dependency. This fact is validated by the results shown in figure 7.3.

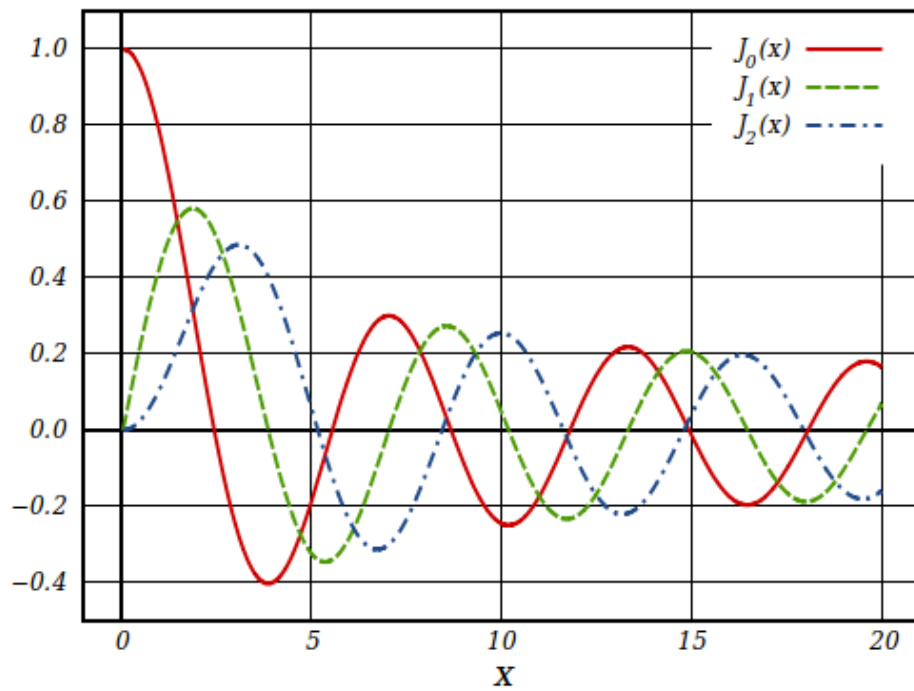


Figure 7.1 - Bessel function of the first kind.

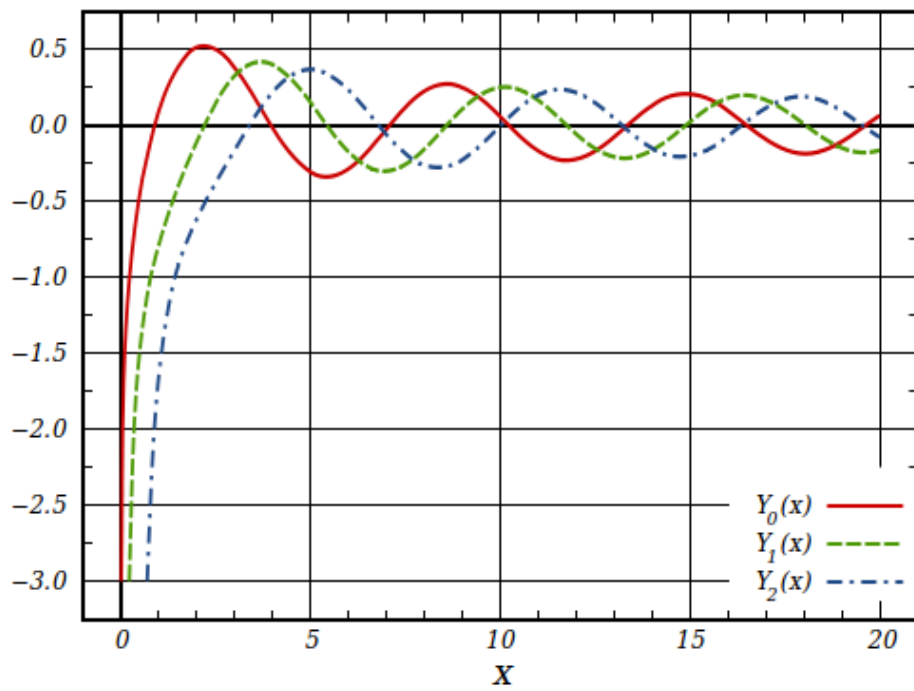


Figure 7.2 - Bessel function of the second kind.

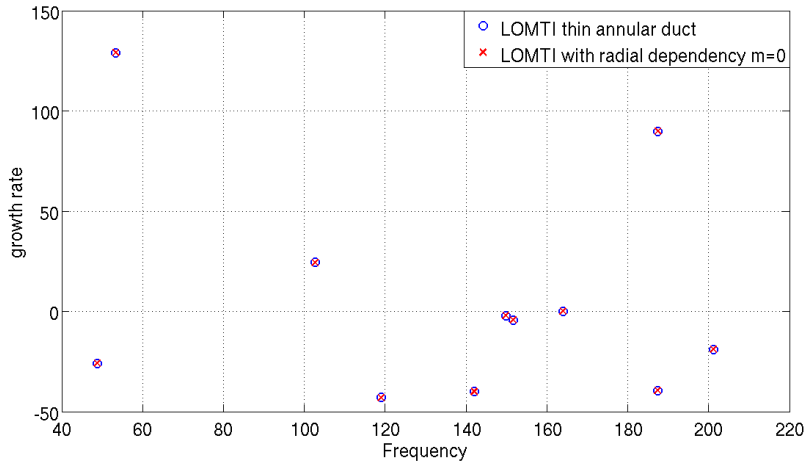


Figure 7.3 - Perfect concordance between duct with negligible thickness and $m = 0$ modes for $\kappa = 1$ and $\tau = 7$ ms, no CBO's and transfer function (5.1).

It is well known the effect of duct dimensions on waves propagating inside it. Thus no frequency larger than the cut-off frequency $f_c = \frac{\bar{c}}{2\pi} \lambda_{m,n} \sqrt{1 - M^2}$ can propagate when $m > 0$, where $\lambda_{m,n}$ is obtained from $\frac{dJ_n}{dr}(\lambda_{m,n}R) = 0$. These cut-off frequencies have been calculated in [33], and are given in table ??.

n	plenum	chamber
0	602.57 Hz	1126.97 Hz
± 1	604.60 Hz	1130.02 Hz
± 2	610.72 Hz	1139.22 Hz

Table 7.1 - Cut-off frequencies in function of azimuthal wave number n for radial mode $m = 1$.

Results for $m > 0$ confirm the damping phenomenon of the duct. For example in figures from 7.4 to 7.6 the lowest frequencies of oscillation in the plenum for $n = 0, 1, 2$ and $m = 1$ are shown.

It is remarkable the fact that all these modes are slightly higher than the relative cutoff frequency. This is very comfortable since it implies that they could be safely disregarded due to their very high frequency and their consequent absence of relation to the humming phenomena. On the other hand, it is important to be able to account for them, since they are very likely related to a phenomenon known as screech [34].

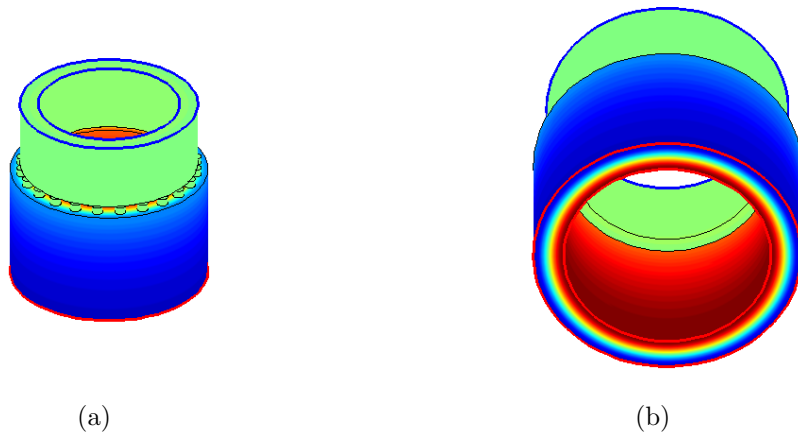


Figure 7.4 - Mode shape for $m = 1$ and $n = 0$ at 603.8 Hz , $GR = 1.7s^{-1}$.

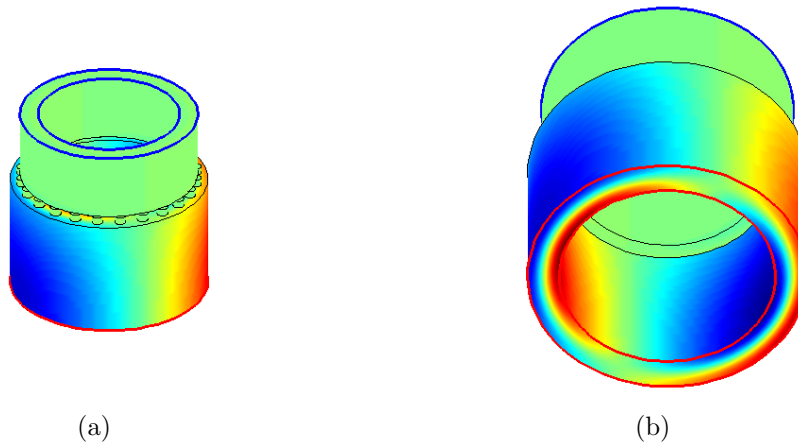


Figure 7.5 - Mode shape for $m = 1$ and $n = 1$ at 605.8 Hz , $GR = 1.75s^{-1}$.

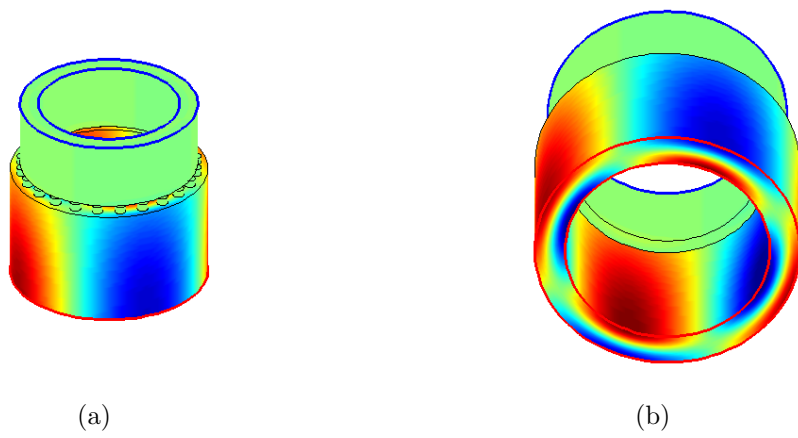


Figure 7.6 - Mode shape for $m = 1$ and $n = 2$ at 612.1 Hz , $GR = 1.8s^{-1}$.

Chapter 8

Proposal for a new transfer function

Since the only weakness of this lumped approach seems to be the flame model perhaps a new transfer function based on empirical data should be developed based on known physical principles. Previous models have already been analyzed in subsection 2.3.1 and the influence of different transfer functions has been evaluated in section 6.5.

8.1 Deducing the expression

As just stated we try to derive a new transfer function based on consolidated principles. The heat release per unit of area Q [W/m^2] is well known from equation (8.1):

$$Q = \frac{\dot{m}_F H_i}{A}. \quad (8.1)$$

where \dot{m}_F is the fuel mass flow rate, A is the flame area and H_i is the lower heat of combustion.

Since in the lumped approximation the flame is actually located at the combustion chamber interfaces with each burner and the thermodynamic variable of the combustion chamber are tuned in order to match the empirical flame temperature we assume that A is equal to $A_{flame} = A_{cc}$ at the combustion chamber inlet section. This is a strong hypothesis which does not match with the effective flame shape; despite this, it certainly represents the exact flame model that the lumped approximation has imposed.

Imposing $\dot{m}_{flame} = \dot{m}_{air} + \dot{m}_F = \rho_{flame} u_{flame} A_{cc}$, and defining the air/fuel ratio $\alpha = \dot{m}_{air}/\dot{m}_F$ we get the expression:

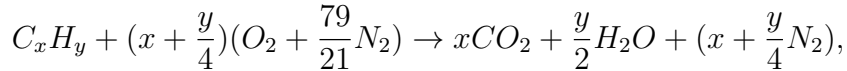
$$Q = \frac{H_i \rho_{flame} u_{cc}}{\alpha_{flame} + 1}. \quad (8.2)$$

We remark the fact that all the quantities are calculated at the combustion chamber inlet where the flame is actually located in the present model. Operating the usual decomposition, simplifying the proper terms and linearizing the lower order ones we get the expression where no direct influence of H_i appears (and thus the features of the fuel are not significant):

$$\frac{Q'}{\bar{Q}} = \frac{\rho'_{flame}}{\bar{\rho}_{flame}} + \frac{u'_{flame}}{\bar{u}_{flame}} - \frac{\alpha'_{flame}}{\bar{\alpha}_{flame} + 1} \quad (8.3)$$

Density and velocity are already present in LOMTI. This can not be said for the air/fuel ratio at the combustion chamber inlet. Analyzing the physics of the phenomenon it is clear that the fluctuation of this quantity is driven by the pressure fluctuations at the fuel injectors that are located in the middle of each diagonal swirler.¹ The idea is to relate the air/fuel ratio perturbation at the flame to the pressure perturbation at the orifice of each injector (with or without *CBO's*). It is clear that this value has to be shifted by the time it spends to travel from the injectors to the flame ($e^{-i\omega\tau(f)}$).² Indeed the pressure of the fuel supply ducts could be assumed constant and independent from outer pressure perturbations of the air flux. Therefore, the air/fuel ratio at the injectors is linked with the fuel and air pressures according to Dalton's law of partial pressures that states: *the total pressure exerted by a gaseous mixture is equal to the sum of the partial pressures of each individual component in a gas mixture*. In mathematical terms, for fuel and air only, it reads: $p_{total} = p_F + p_{air}$, or $y_F = p_F/p_{total}$ where p_{total} is the mean pressure at the injector itself, i.e. the mean pressure in each premixer duct (p_2).

Since the thermal power produced by the flame is, more or less, all converted in enthalpy of the mixture, we can write, neglecting the kinetic energy, that $\dot{m}_F H_i = \dot{m} \Delta H_0 \simeq \dot{m}_F (\alpha + 1) c_P (T_{cc} - T_{premixer})$.³ Since the methane heat of combustion is approximately $50 MJ/Kg$ and the temperatures are known, a value of $\alpha \approx 35$ is unequivocally obtained. This value confirms the chemical approach that imposes a lean combustion where the equivalence ratio is set approximately to $\phi \simeq 0.53$. In this case Φ is defined as α_{ST}/α where, for a reaction like



a stoichiometric air/fuel ratio like

$$\alpha_{ST} = \left(x + \frac{y}{4}\right) \frac{100}{21} \frac{PM_{air}}{PM_{C_x H_y}},$$

results. For the combustion of methane in air $\alpha_{ST} \simeq 17.167$, thus

$$\alpha = \frac{\dot{m}_{air}}{\dot{m}_F} = \frac{\alpha_{ST}}{\Phi} = \frac{17.167}{0.53} \simeq 32.$$

From the value of α we are able to unequivocally define the value of p_F that is considered unaffected by any fluctuation; then in its expression all the values could be replaced with their mean quantity:

¹The possible influence of the pilot diffusion flame sustained by the axial swirler is disregarded.

²Note that this represents only a phase displacement since $e^{i\omega t} \cdot e^{-i\omega\tau} = e^{i\omega(t-\tau)}$.

³ $T_{cc} = T_{flame}$.

$$\alpha = \frac{m_{air}}{m_F} = \frac{n_{air}}{n_F} \frac{PM_{air}}{PM_F} = \frac{p_{air}}{p_F} \frac{PM_{air}}{PM_F} = \frac{p_{total} - p_F}{p_F} \frac{PM_{air}}{PM_F} = \left(\frac{p_2}{p_F} - 1 \right) \frac{PM_{air}}{PM_F}.$$

Imposing $PM_{air}/PM_F = \chi = 28.84/16 = 1.8025$ for methane we get the expression:

$$p_F = \bar{p}_2 \frac{\chi}{\chi + \bar{\alpha}}.$$

Then we have to relate the pressure fluctuations at the injector with the air/fuel ratio fluctuations. Again from the expression of α we get:

$$\alpha = \left(\frac{p_2}{p_F} - 1 \right) \chi.$$

After the usual decomposition it becomes:

$$\bar{\alpha} + \alpha' = \left(\frac{\bar{p}_2'}{p_F} + \frac{p'_{inj}}{p_F} - \chi \right) \chi.$$

where the value of p_F has to be replaced with its expression. The expression for $\alpha' = f(p'_{inj})$ becomes:

$$\alpha' = (\chi + \bar{\alpha}) \frac{p'_{inj}}{\bar{p}_2}. \quad (8.4)$$

We can briefly discuss on its physical meaning arguing that a positive value for p' , i.e. a pressure increase of the mixture in the premixer, yields a minor fuel mass flow rate and then an augmented air/fuel ratio or rather a positive value for α' . The value of α' already obtained reaches the flame, i.e. the combustion chamber inlet, after a convective delay time represented by the usual function $e^{-i\omega\tau}$. The final expression for the proposed transfer function is then:

$$\frac{Q'}{Q} = \frac{\rho'_{flame}}{\bar{\rho}_3} + \frac{u'_{flame}}{\bar{u}_3} - \frac{\bar{\alpha} + \chi}{\bar{\alpha} + 1} \cdot \frac{p'_{inj}}{\bar{p}_2} e^{-i\omega\tau}, \quad (8.5)$$

here subscripts 2 and 3 stand for premixers and combustion chamber respectively while *flame* and *inj* mean the combustion chamber inlet and the injection point. It is remarkable the fact that $(\bar{\alpha} + \chi)/(\bar{\alpha} + 1)$ is approximately equal to unit in the case of lean combustion of methane and air, thus its contribution must be taken into account. Let us further analyze this term: it practically takes the place of the unknown κ parameter that is so no longer unknown. Replacing α with α_{ST}/Φ let us plot this term as a function of Φ .

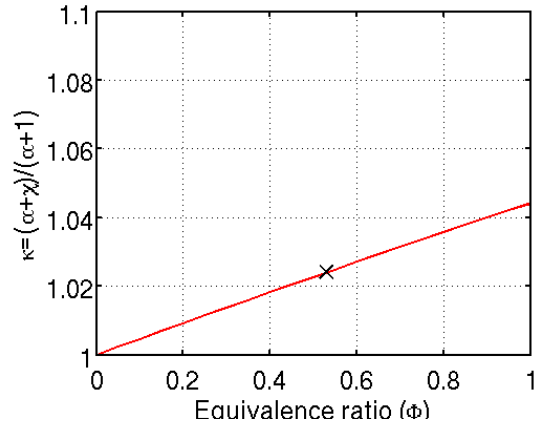


Figure 8.1 - Influence of Φ on the transfer function term containing multiplying p' . The black cross denotes the value of $\kappa = 1.024$ for $\Phi = 0.53$ used for the lean combustion.

From figure 8.1 it is clear that the evaluation of Φ is not a critical issue since the value of $(\bar{\alpha} + \chi)/(\bar{\alpha} + 1)$ remains very close to one even if the value of Φ varies from zero (no fuel) to one (stoichiometric combustion). It seems to be a linear trend but actually $\lim_{\Phi \rightarrow +\infty} = \chi$ (note that the validity of the model breaks off for $\Phi > 1$) thus it is a bounded set. Nevertheless we have just argued that its value is always near to one, forcing us to take it into account for every possible load.

This new flame transfer function has the aim to overcome some inconsistencies with previous models. Although there is no unknown multiplying factor such as κ , the presence of the delay time τ is not avoided. Stressing the fact that we are trying to represent the "lumped flat flame" this value of τ should be exactly equal to the ratio between the distance of the fuel injectors from the flame and the mean flow velocity in each pre-mixer duct. In this case τ assumes clearly only a convective meaning, therefore the best way to determine it is by evaluating the time a particle employs to travel from the injection to the flame surface where the rate of reaction is maximum as we can see in figure 8.2. Since there are more pathlines that can be evaluated a mean value of this times should be considered.

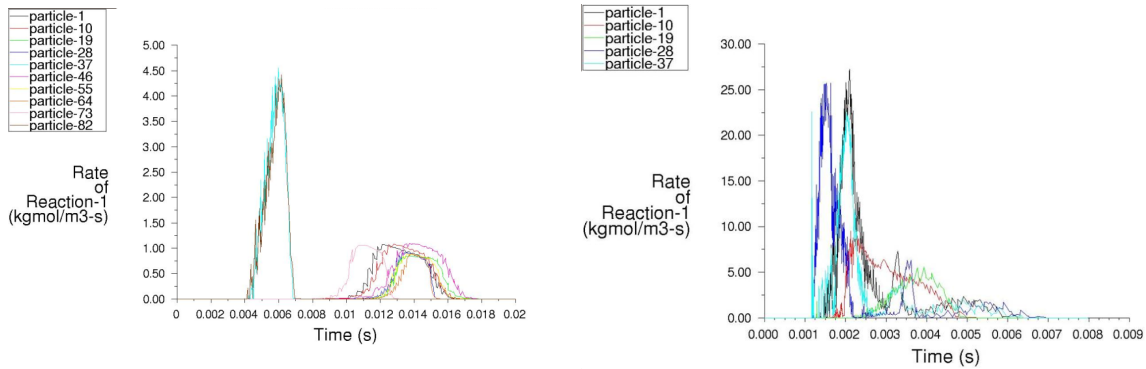


Figure 8.2 - Results from pathlines computation for particles released in the diagonal (left) and in the axial (right) swirler. The peaks denote the time when a particle experienced the maximum rate of reaction, i.e. when it pass through the flame front.

In the calibration phase not much importance was ascribed to the premixers' dimensions. In such a model, where the delay time is calculated from geometrical values, the length of the premixers assumes a new importance. Furthermore, it is well known that the mixture flux in these ducts is considerably swirled, thus a correction that takes into account this feature could be required in order to obtain reliable results.⁴

The eventual weaknesses of this flame model are the same encountered in the lumped approach that inevitably considers a flat region of heat release confined in a thin sheet at the premixers/combustion chamber interface. The fluctuating quantities are always calculated at the flame itself when possible or related to other physical variables according to well known principles. The only further hypothesis is to consider the fuel pressure independent from the unsteady flow field at the injectors. Nevertheless this seems to be a good approximation considering the mechanism of fuel supply that consists in a rotating valve modulating the mass flow rate of fuel injected in the diagonal swirlers. Therefore no further hypothesis is done to obtain this flame transfer function.

If it would be possible to control the value of p_F rendering it time dependent, this approach could give information on the design of active control that modulate fuel injection in order to get a negative value of the $p'(\vec{x}, t) \cdot q'(\vec{x}, t)$ term in the Rayleigh's criterion for all regimes.

⁴The swirl number $Sw = (Moment\ of\ momentum)/(Momentum \cdot Radius) \simeq 0.5$ thus the value of the convective delay time should be approximately doubled.

8.2 Results for the turbine configuration

In figure 8.3 results for transfer function (8.5) are shown. Only two unstable eigenmodes are found at 106 and 195 Hz (shown in figure 8.4). Furthermore they seem not to be greatly influenced by τ variations.

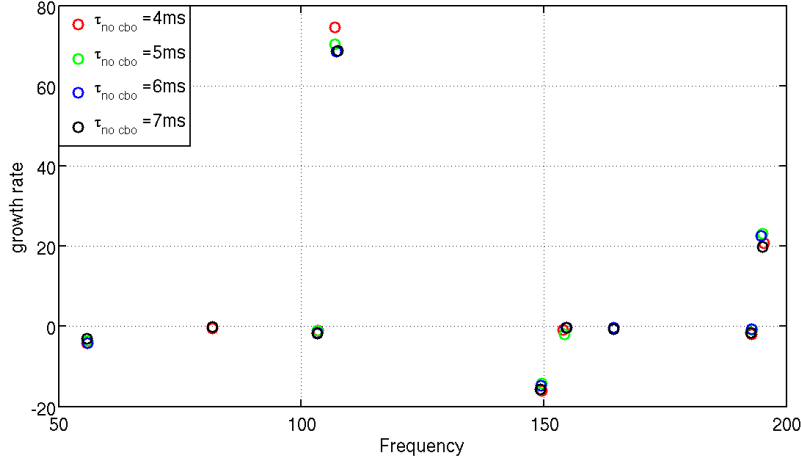


Figure 8.3 - Results for $d_{ref} = \frac{1}{2}L_{premixer}$. The typical configuration of AE94.3A gas turbine with 20 CBO's is chosen. The acoustic boundary conditions are $u' = 0$.

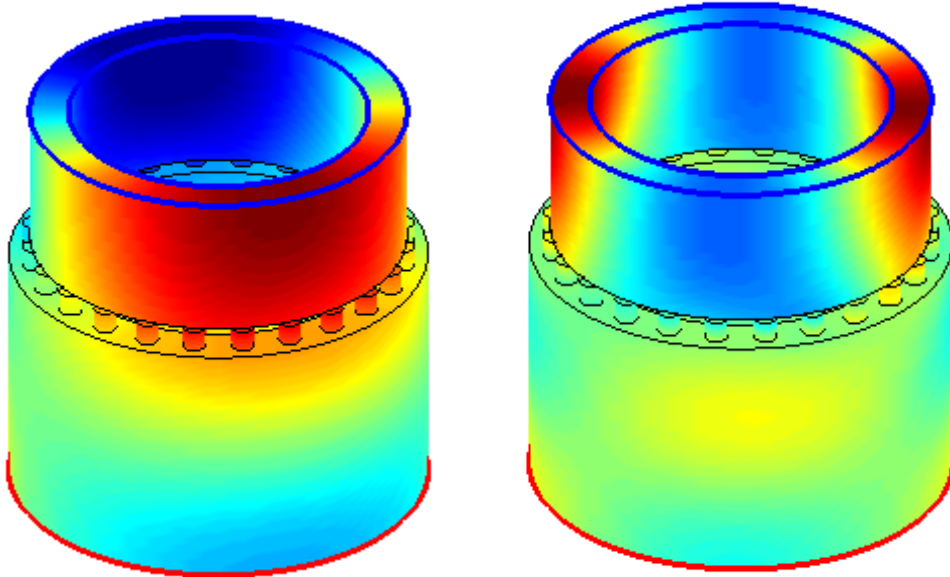


Figure 8.4 - Mode shape for $106 \text{ Hz} + i70 \text{ s}^{-1}$ and $195 \text{ Hz} + i23 \text{ s}^{-1}$ eigenmodes respectively.

Further analysis varying the reference point confirm its weak influence as just deduced from the previous study shown in figure 6.14. An explanation could be found analyzing the pressure mode shape in each premixer: actually p' does not vary significantly along the ducts, hence a reference point located in the middle of the duct

experiences very similar pressure oscillations if compared to another one at any other location (in particular if we are primarily interested in their phase).

It is remarkable the fact that we obtain only two unstable modes as we expect from experimental results. Nevertheless these modes seem not to be greatly influenced by the parameter τ that should be related to the appearance of the humming phenomenon. At first, we could assume that this fact finds an explanation in the pressure mode shapes in the premixers. Performing a time-space equivalence we go back to the statement done for the reference point influence. But this argument should be valid also for the commonly employed transfer function, and this is not true. Therefore we are forced to conclude that p'_2 has a lower order of magnitude than \dot{m}'_3 . According to this, the leading term seems to be the mass flow rate perturbation in the combustion chamber itself. Even if pressure perturbations at the injectors modify the equivalence ratio of the mixture, the fuel mass flow rate at the flame is primarily influenced by the overall mass flow rate at the flame itself. Finally the heat release rate is due only to the fuel reaching the flame front. We are forced to conclude that the relation between Φ and p'_2 is only a refinement of the model. The resulting simplified transfer function where pressure influence at the injectors is neglected is:

$$\frac{Q'}{\bar{Q}} = \frac{\rho'_{flame}}{\bar{\rho}_3} + \frac{u'_{flame}}{\bar{u}_3}, \quad (8.6)$$

and results are shown in figure 8.5. The unstable modes are only slightly influenced by this simplification. This results confirm the hypothesis just outlined. Nevertheless transfer function (8.6) does not ensure any speed-up in the computation of the eigenvalues, therefore equation (8.5) should be preferred.

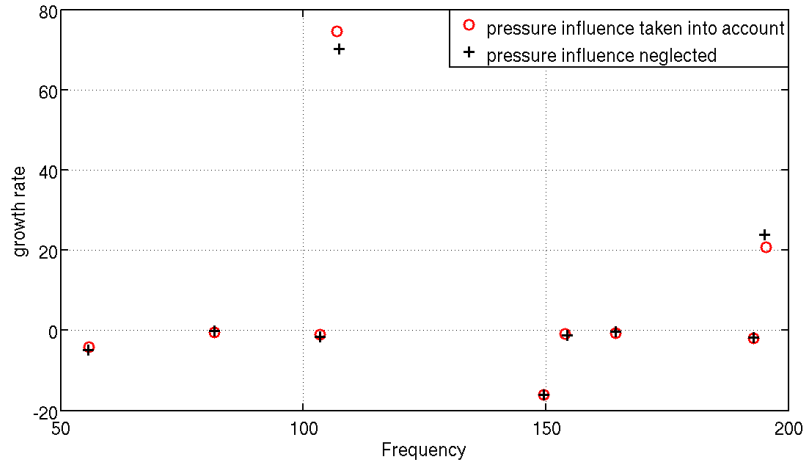


Figure 8.5 - Comparison between results for $\tau = 4ms$ in figure 8.3 and the simplified transfer function (8.6).

Chapter 9

Conclusions and future developments

9.1 Conclusions

The geometric parameters used in LOMTI to represent an ANSALDO turbine configuration have been calibrated in order to reproduce results obtained with COMSOL in a 3D sector of the turbine, without a meanflow.

Considering the drastic geometric approximations used in LOMTI, the matching of LOMTI results with COMSOLs' is very good, both with and without flame and the capacity of LOMTI's simple model to obtain analogous results with a much smaller computational time is doubtless satisfying. Further development could be done by increasing the number of ducts representing plenum and combustion chamber in order to improve the match with the real geometry as shown in figure 9.1.

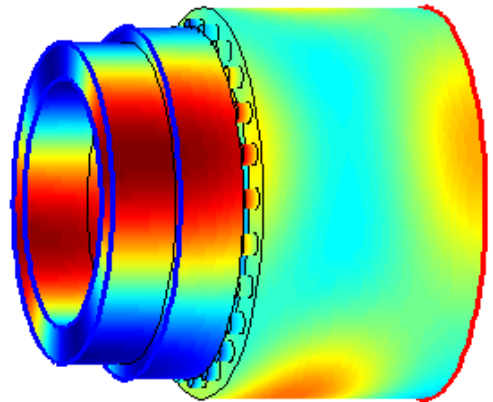


Figure 9.1 - *Two pieces configuration for the combustion chamber.*

Several parametric studies have been carried out. The influence of combustion chamber size has been checked in order to provide informations on new developments of the AE94.3A gas turbine. The influence of κ and τ parameters has been evaluated, also with frequency dependence. Different FTF have been tested with different reference points.

Constant specific heats approximation has been removed in order to obtain a more accurate model. c_p and c_v are now functions of temperature and chemical composition in each duct. Finally the thin duct approximation has been removed to demonstrate

that it provides an accurate representation because of the presence of cutoff frequencies that allow to disregard high radial frequencies.

9.2 Future developments

9.2.1 Further development of the FTF

In order to overcome the flat flame approximation it will be necessary to develop a refined flame transfer function from equation (8.5). In that model the surface of the flame is approximated by the cross sectional area of the combustion chamber applying the well known relationship $\dot{m} = \rho_u A$. However the flame surface itself is influenced by acoustics, so that the relation below is more appropriate since it takes into account these variations:

$$\dot{m} = \rho_u S_T A_{flame}. \quad (9.1)$$

Since ρ_u is the density of unburned gas in the premixers we have to deal only with the turbulent flame speed S_T . Unfortunately, the relationships available are full of empirical parameters [39] or contain unknown terms such as \dot{m}_F''' in equation (9.2) that is the "negative production of fuel" inside the flame volume, defined as $\dot{m}_F/(\delta A_{flame})$:

$$\begin{aligned} \frac{S_T}{S_L} &= 1 + \frac{u'_{rms}}{S_L}, \\ S_L &= \sqrt{-\frac{2\lambda_T}{\rho_u^2 c_P} (\alpha + 1) \dot{m}_F'''.} \end{aligned} \quad (9.2)$$

A model [40] that relates the flame surface variations to the supply velocity u can be used to define an oscillating flame. However this model requires the evaluation of the characteristic time τ^* that represents the average time for gas exiting the burner to be consumed by the flame. For clarity in equation (9.3), the notation τ^* is used to make distinction with the usual time lag τ .

$$\frac{A'_{flame}}{\bar{A}_{flame}} = \frac{1}{1 + i\omega\tau^*} \frac{u'}{\bar{u}}. \quad (9.3)$$

Imposing $\kappa e^{-i\omega\tau} = (1 + i\omega\tau^*)^{-1}$ we can write equation (9.3) according to the usual expressions for the transfer functions:

$$\frac{A'_{flame}}{\bar{A}_{flame}} = \frac{1}{\sqrt{1 + \omega^2\tau^{*2}}} \frac{u'}{\bar{u}} e^{i \cdot atan(\omega\tau^*)}. \quad (9.4)$$

Directly linearizing the equation (8.1) we obtain the expression:

$$\frac{Q'}{\bar{Q}} = \frac{\dot{m}'_2}{\dot{m}_2} - \frac{A'_{flame}}{\bar{A}_{flame}} - \frac{\alpha'_{flame}}{\bar{\alpha}_{flame} + 1}. \quad (9.5)$$

In this expression \dot{m}_2 is no longer evaluated at the flame front but it represents a mass flow rate upstream, hence a multiplying term $e^{-i\omega\tau}$ is required. Combining the equations (8.4), (9.3) and (9.5) we get the complete expression:

$$\frac{Q'}{\bar{Q}} = \left(\frac{\dot{m}'_{ref}}{\dot{m}_2} - \frac{\bar{\alpha} + \chi p'_{inj}}{\bar{\alpha} + 1 \bar{p}_2} \right) e^{i\omega\tau} - \frac{1}{\sqrt{1 + \omega^2\tau^{*2}}} \frac{u'}{\bar{u}} e^{i \cdot atan(\omega\tau^*)}.$$

It is immediately evident that the number of parameters has grown since both τ^* and τ are to be evaluated, and the reference point must be chosen. Ultimately, a careful study of equation (9.3) should be carried out in order to determine its range of applicability.

9.2.2 Computational time

For simple configurations there are no inconveniences with the Matlab environment: the determinant of the matrix generated from the set of equations can be calculated for each $\omega = \omega_r + \omega_i$ in a very short time. The code runs in a few seconds and no problems concerning speed up arise. The computational time required could become no longer negligible in more complicated configurations. Since more than 60% of elapsed time is spent computing the determinant, the code could be upgraded to a MEX File that uses a compiled program (C++, FORTRAN) for calculating the determinant for each value of ω in order to obtain a significant speed up.

9.2.3 Passive controls

Several solutions for damping instabilities without designing active control techniques have been tested in recent years. Disrupting axisymmetry adding *CBO's* has been mentioned in section 4.3. This is the easiest and less intrusive way to damp the instabilities. Other devices focus on a single resonant frequency such as Helmholtz resonators.

Helmholtz resonators are studied to damp standing waves occurring inside the combustion chamber. The characteristic frequency, such as a mass-spring system, is:

$$\omega_R = 2\pi f_R = c_s \sqrt{\frac{A_n}{V \cdot L_n}}$$

where A_n and L_n are respectively the cross sectional area and the length of the neck of the Helmholtz resonator, and V is the volume of the entire cavity.



Figure 9.2 - *Academical Helmholtz resonators.*

We now rapidly comment on the effect of adding Helmholtz resonators to the geometry. Helmholtz resonators are damping devices consisting of a large volume connected to the combustor via a short neck.¹ Attaching a Helmholtz resonator destroys the axisymmetry of the geometry, leading to modal coupling.² Furthermore the resonator

¹Problems in placing Helmholtz resonators in the combustion chamber could arise because of film cooling, assembling and maintenance.

²The interruption of axisymmetry has already been noticed adding *CBO's* to some burner.

itself is able to modify the pressure field at its neck connection damping the characteristic frequency f_R .

The location of the Helmholtz resonators has a major influence on their effectiveness. A single Helmholtz resonator does not absorb energy from a circumferential wave but only reflect an equal and opposite wave, generating a pressure node at the neck connection. Thus, in order to damp dangerous azimuthal waves multiple resonators distributed in optimal locations are required. The optimal placement is:

$$\theta_j = \frac{\pi}{n} \left(\frac{j-1}{N} + P \right)$$

where j is the index of the $N > 1$ resonators, n is the circumferential wave number and P an arbitrary positive integer. The main problem with Helmholtz resonators is the dimension of the cavity required to damp typical low frequency instabilities. Considering a 100 Hz instability the volume required would be approximately 3 dm^3 that could be unsuited for the combustor's design.

A specific resonator is able to damp only a single frequency f_R . Thus it could be very difficult to capture the exact frequency since the ideal resonator works with no tolerance. Implementing the presence of such an Helmholtz resonator in a model (COMSOL or LOMTI) means to impose a specific impedance I as boundary condition. This impedance would be composed only by a reactive term iX where $i^2 = -1$ and X proceeds from algebraic relationship with f_R and further parameters. But the effective physics of the phenomenon must also take into account viscosity. A viscous term is always present and it extends the field of frequencies where the resonator works. Whereas an ideal resonator has the capability to completely damp its characteristic frequency, a real resonator has a minor effect as viscosity is stronger but its range is expanded. If a major viscous term is desired, a grid could be placed at the resonator neck that can amplify the effective viscous term. The equivalent impedance is now composed by an additional dissipative term R depending on ν and on the geometrical values of the perforated plate (such as the number of holes and their diameter). It is not trivial to choose the optimal arrangement concerning the effective values of the resonator's dimensions (only ratios between A_n , L_n and V are given) and the optimal perforated plate.

Appendix A

Combustion processes and related emissions

Combustion processes can be classified according to different aspects that characterize them. The most interesting classification concerns the initial conditions of mixing between air and fuel, i.e. premixed or diffusion flames.

A flame is premixed when, prior to combustion, fuel and oxidizer are mixed together. Combustion occurs in a homogeneous environment, with a flame front which separates the reactants from products and ignition in one or more points. A flame is defined a diffusion flame when the mixing between fuel and oxidizer occurs in the same area in which it develops combustion.

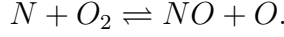
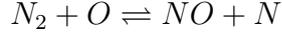
The conditions of mixing of reagents have many repercussions both on the combustion processes and the formation of pollutants. We are particularly interested in the effect on the formation of NO_X . Let us briefly analyze why NO_X are generated. The formation of NO (approximately 90% of NO_X) is strongly affected by temperature. In fact, oxygen and nitrogen are present, without giving rise to reactions of any kind, in the atmosphere, but formation of NO occurs when $T > 1600K$.

Temperature [$^{\circ}C$]	Equilibrium concentration [ppm]	Time to get 500 ppm [s]
27	$1.1 \cdot 10^{-10}$	—
527	0.77	—
1316	550	1370
1538	1380	162
1760	2600	1.10
1980	4150	0.117

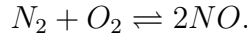
Table A.1 - *Time of formation for NO from N_2 and O_2 .*

NO_X formation processes are quite complex and are developed through many chemical equilibrium and non-equilibrium reactions that occur in processes of pre, post-combustion and combustion. Considering only balance reactions, the main mechanism

of formation of NO is proposed by Zeldovich [38]. It is based on two basic reactions of balance:



The rates of these two steps are known accurately, and the second is fast compared with the first. Hence the rate at which NO is produced depends strongly on the concentration of O atoms which in turn is highly sensitive to the kinetics of the combustion process. They give rise to a chain reaction which can be so synthesized:



At low temperatures, equilibrium is strongly shifted to the left according to table A.1. But the kinetics is strongly affected by temperature as shown in Arrhenius' equation:

$$\frac{\partial}{\partial t}[NO] = 6 \cdot 10^{16} \cdot T_{eq}^{-0.5} \cdot e^{-\frac{E_a}{R_u T_{eq}}} \cdot [O_{2eq}]^{0.5} \cdot [N_{2eq}]$$

where E_a is the activation energy equal to $19.8 \frac{MJ}{Kg}$ in this case.

In Zeldovich's reaction, temperature and residence time of gas at that temperature play a fundamental role. Indeed, if the gas temperature drops quickly after fuel combustion (eg. for their expansion in the first stage of TG), the equilibrium achieved at high temperature is frozen and NO_X do not have time to return to molecular nitrogen and oxygen. Therefore the attainment of the equilibrium concentration at lower temperatures (which corresponds to a decreased concentration of NO) is not possible. It is therefore evident that it is not the average temperature to greatly influence the formation of pollutants but its peaks, governed by the local equivalence ratio Φ . In diffusion flames the physiological inhomogeneous mixing of the reagents leads to local equivalence ratio values very far from the conditions of a lean mixture, producing local peaks of temperature. Hence this amount of pollutant are called thermal NO_X . Another mechanism that may be of importance is $HCN + O \rightarrow CH + NO$, the HCN having been produced either by $CH + N_2 \rightarrow HCN + N$ or from the fuel itself if the fuel contains sufficient amounts of bound nitrogen. This mechanism of production of the so called prompt NO is not directly dependent by the temperature and is not avoided with lean combustion. Nevertheless this amount is significantly lower than thermal one.

These high local values of temperature were damped in older gas turbine through a water-steam injection system in the combustion chamber. This method no longer satisfies the recent regulations on emissions forcing manufacturers to shift to a different type of combustion i.e. premixed one despite its inclination to instability. The *Low NO_X Lean Premix System* acts both on the local temperature and on the equivalence ratio. For stability reasons about 10% of the combustion is still provided by a diffusion pilot flame.

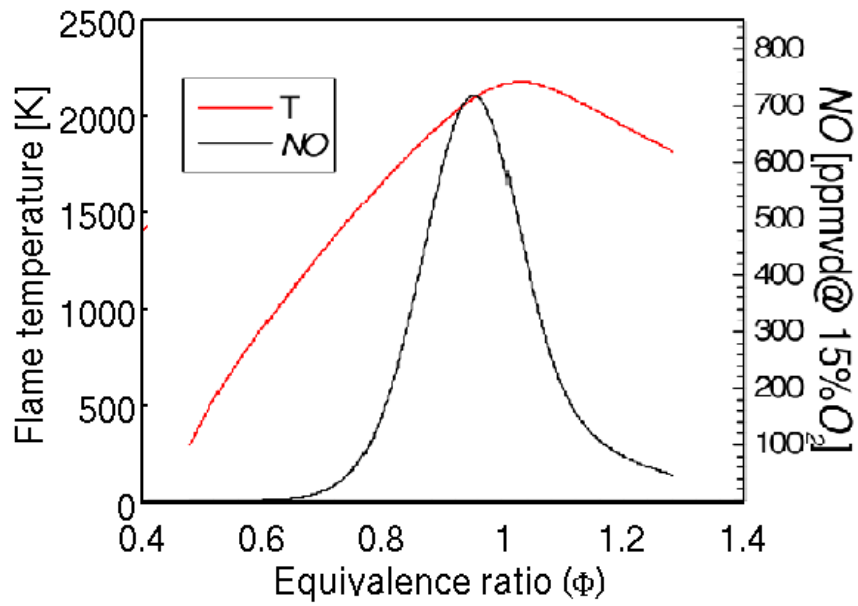


Figure A.1 - Flame temperature and NO_X formation related to the equivalence ratio.

Oxidation of NO in the atmosphere gives rise to NO_2 and NO_3 ions which can aggregate in small particles with other compounds. NO_X can also react with rainwater generating nitric acid (HNO_3) responsible, along with sulfuric acid, of the phenomenon of "acid rain" and of photochemical smog. The direct effects of NO_X on man are mainly diseases affecting the respiratory system. In figure A.2 the values of rain pH in USA, in 1985 are shown.

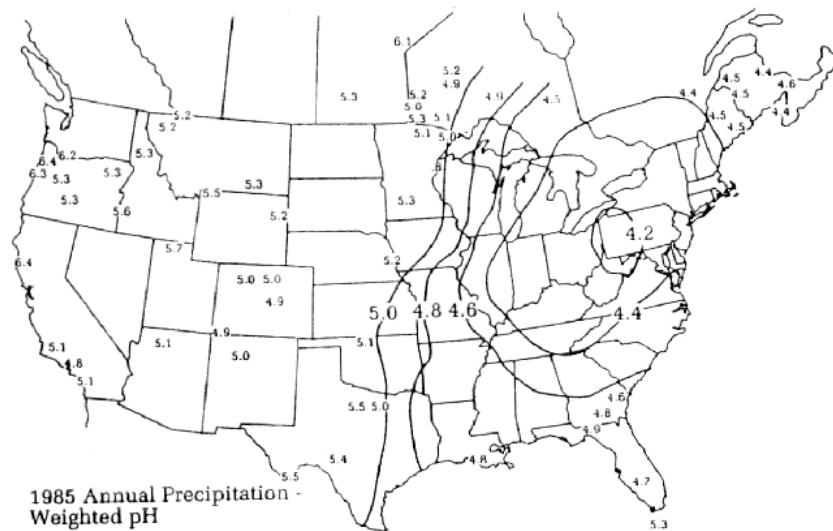


Figure A.2 - pH level in rain

Photochemical oxidizers and ozone are associated with secondary pollution (reactions of primary pollutants with substances in the atmosphere under the influence of

solar radiation). They can not be strictly attributed to anthropogenic sources. The main product of photochemical reactions is ozone, whose formation is usually attributed to the photolytic cycle of nitrogen dioxide NO_2 .

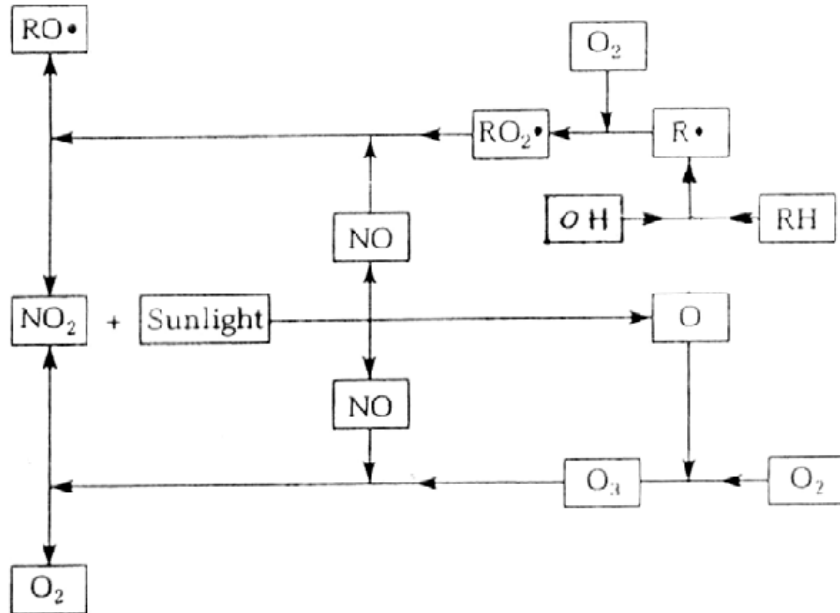
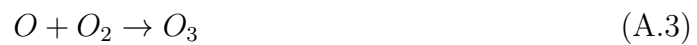


Figure A.3 - Ozone cycle

Under normal conditions the "cycle of ozone" is composed by the following reactions (lower cycle) where $h\nu$ represents a the energy carried by a photon of frequency ν :¹



Reactions (A.2) to (A.4) constitute a system in equilibrium in which the ozone produced is a function of the concentrations of NO_2 and NO , and the intensity of solar radiation. In this cycle the hydrocarbons present in the atmosphere (radical hydrogenated RH) play a role, in generating highly active RO_2 , that replace ozone in the reaction (A.4) to oxidize NO to NO_2 . The result of this process is an increase in the concentration of ozone and nitrogen dioxide in the atmosphere.

¹ $h = 6.62606896(33)1034J \cdot s$ is the Planck constant.

Appendix B

The function determinant

Just to understand the code and its results it is useful to understand the object of our investigation, i.e. the determinant of the matrix M representing the analyzed system. Since every component of the matrix is something like $p'(\omega_r, \omega_i) \simeq e^{ikx}$, where k is a function of ω_r and ω_i , let us first understand its shape in figure B.1. Here we can visualize an exponential behaviour in the imaginary axis and a oscillatory one in the real axis.

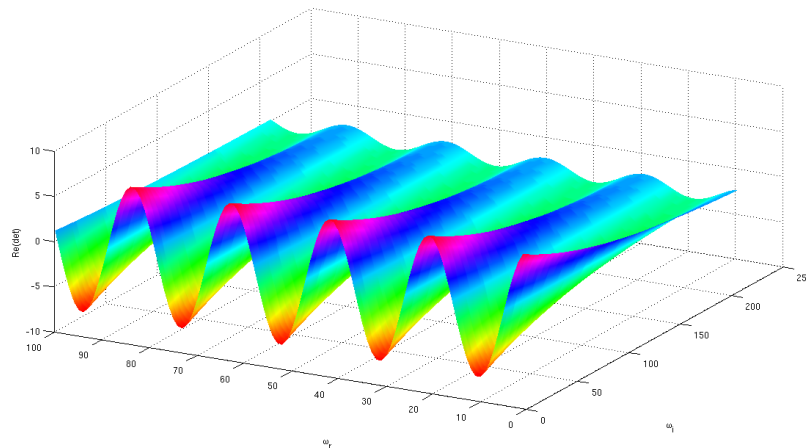


Figure B.1 - *Perturbation shape.*

Since the determinant is something deriving from the product of these perturbations, its shape will be very similar. In figure B.2 a three dimensional visualization for the contours in figure 3.4 is shown.

It is clear that increasing the complexity of the model (increasing the number of equations) leads to very variable values of the determinant. Going far away from neutral modes ($\omega_i = 0$) we get very small $\det(M)$ for negative ω_i and very high $\det(M)$ for positive ω_i . Moreover oscillations in the real axis have higher and higher frequency. These facts have not negligible implications.

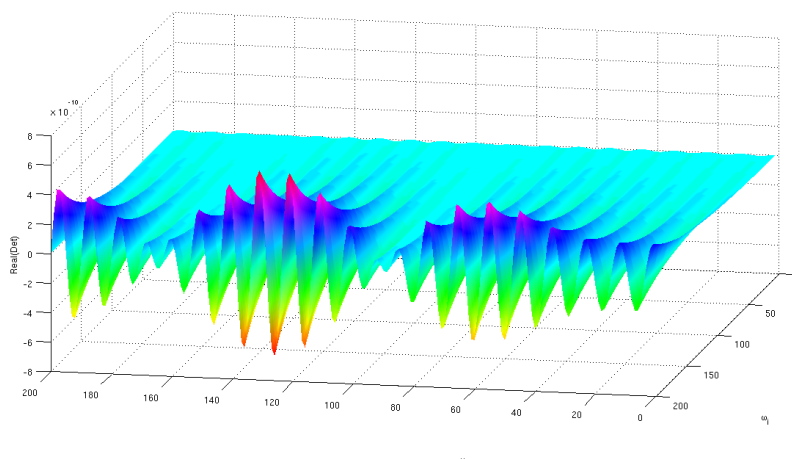


Figure B.2 - Real part of the determinant shape.

First of all a large discrepancy in the values of the determinant lead to a numerical problem in computing ω that render $\det(M)$ equal to zero. This problem could be overcome splitting the computational domain in several windows where the determinant assumes values of comparable orders of magnitude.

During the calibration phase, we have encountered another numerical problem due to the low Mach number approximation. Considering $p'(\omega) \simeq e^{ikx}$ and evaluating the expression¹

$$\lim_{M \rightarrow 0} p'(\omega) \simeq e^{\pm i|\omega|}$$

we obtain that the the determinant is strongly dependent on ω_i , thus, just for ω slightly far from neutral modes, we obtain values of $\det(M)$ very small and very high that exceed machine precision giving zero or NaN (Not a Number) values without matrix scaling.

Hence, in terms of computational time, the choice of a proper size of interrogation window is critical. It could be logical that a smaller window would give more accurate results, but according to the shape of the determinant there is always a threshold that cut off the higher frequency of oscillation along the ω_r axis providing the same results with a significantly smaller computational time (even five times faster). Unfortunately, no fixed value for the size of the window has been evaluated since it depends strongly on the mean flow values. For this reason it is difficult to guess a size without some preliminary trial and error attempts.

Double modes. While evaluating modes of oscillation in the calibration phase, double solutions have been detected. Indeed several modes are found to be double beyond any doubt. An example is shown in figure B.3.

¹Entropy waves are neglected since $\lim_{M \rightarrow 0} p'_e = 0$

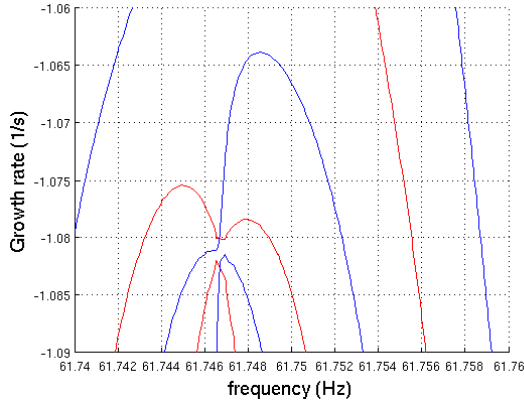


Figure B.3 - *Example of a double mode.*

The reason of this result must be searched in the absence of *CBO's*, that, breaking axisymmetry, would shift the modes. COMSOL results show only single modes since the simulation was performed over a quarter of the domain in order to identify unambiguously every mode. Three tests are performed in order to achieve this conclusion:

- higher Mach number in figure B.4
- non zero value of the flame parameter κ in figure B.5
- adding a simple *CBO* in figure B.6

Indeed double eigenfrequencies occur only for azimuthal modes in the absence of *CBO's*. Axial modes always display a single eigenfrequency since they are not influenced by axisymmetry.

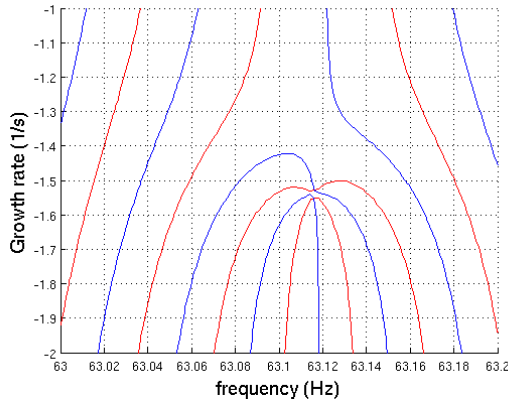


Figure B.4 - *Double mode for $M \neq 0$*

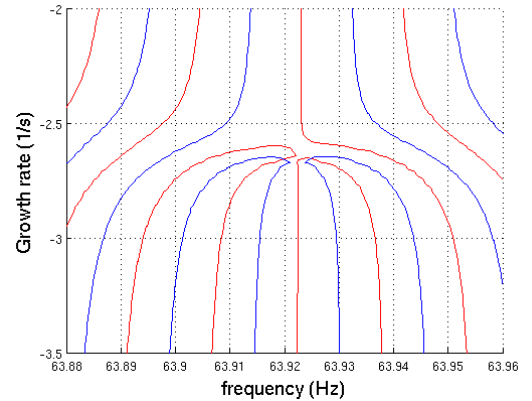


Figure B.5 - *Double mode for $\kappa \neq 0$*

Another fact is worth mentioning: in the determination of the mode shapes, the eigenfunctions assume a different expression because of a linear time dependent factor. If every mode is stable it could affect the linear approximation of small perturbations for short time intervals since the disturbance would be something proportional to $t \cdot e^{i\omega t}$ like shown in figure B.7, leading to a sort of bootstrap. In other words, even in the presence of modes always damped, the appearance of double eigenmodes (as well) could lead to a transient linear amplification of the perturbation, with an algebraic growth in time [36].

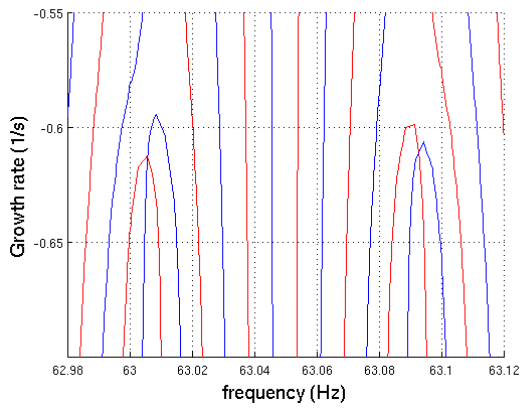


Figure B.6 - *Quasi double mode for one CBO configuration*

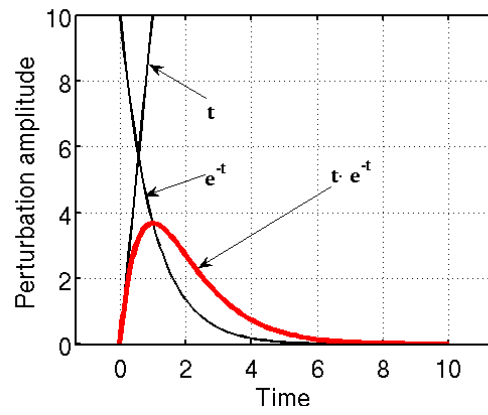


Figure B.7 - *Time dependent one-dimensional mode shape*

Appendix C

Specific heat ratio dependency

In the literature, the specific heats c_p and c_v are generally approximated as independent from temperature. Let us analyze the influence of this assumption on our model starting from analytical considerations. The specific heat ratio γ appears both in the mean flow computations and in LOMTI, when the speed of sound is to be evaluated in each duct, as $c_{si} = \sqrt{\gamma RT_i}$. From polynomial approximation of experimental results we get an expression for γ as function of the temperature T (pressure dependence is negligible)[18]. Thus γ is not always equal to 1.4, and an expression $\gamma_i = f(T_i)$ should be employed in each duct.

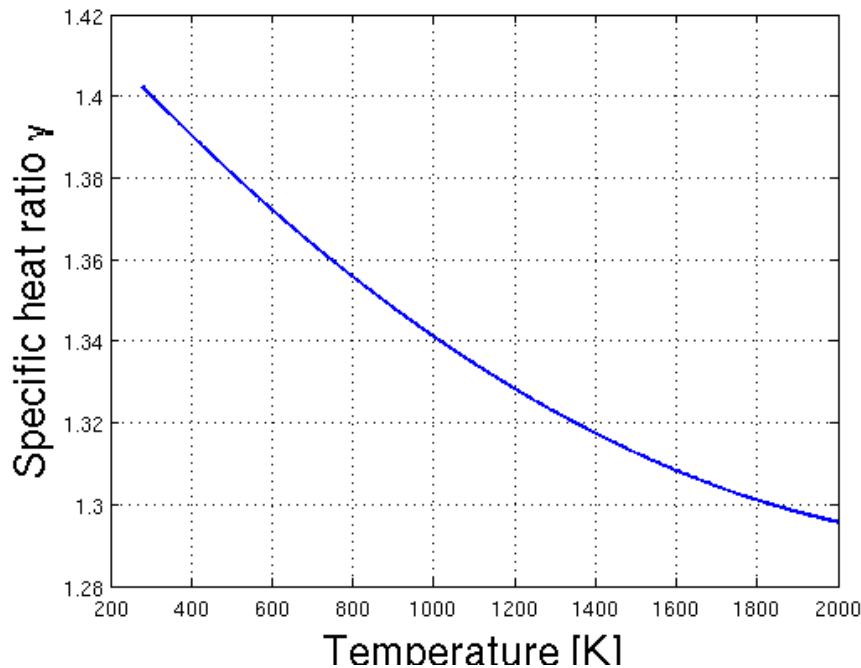


Figure C.1 - *Temperature dependency of γ for air.*

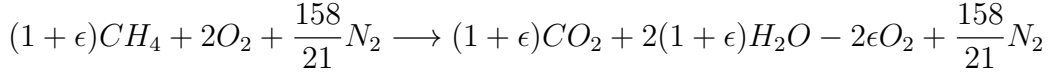
Therefore, if γ shifts from 1.4 to 1.3, we get a variation of c_s according to $1 - \frac{\sqrt{1.3}}{\sqrt{1.4}}$. The speed of sound variation affects eigenfrequencies since acoustical perturbations will be slower in ducts with higher temperature (such as combustion chamber). Strictly

geometrical frequencies are well represented by the expression:

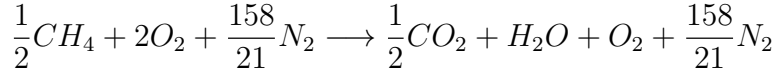
$$f_n = n \frac{c_s}{L}$$

where L is the effective length (or radius!) perturbations have to travel. Practically the speed of sound would shift by a 4% affecting frequencies by the same value. Since the most interesting modes are in the combustion chamber where $\gamma \approx 1.3$ the temperature dependency should be taken into account. No such analytical consideration is easy to be reproduced considering growth rate thus a numerical approach is performed.

Since chemical composition y_i in each duct varies according to fuel mixing and combustion, γ will be evaluated according both to T_i and y_i . The approximated overall reaction across the flame is:



Imposing $\epsilon = -0.5$ according to lean premix combustion we get the reaction:



Considering the molar mass of each species we get their molar fraction in each duct. Indeed molar fractions could differ in real gas turbine: generally there is more oxygen in products (up to 12%). Despite this we can disregard this approximation since results would be slightly different.

	N_2	O_2	CH_4	CO_2	H_2O
Plenum	79%	21%	-	-	-
Premixers	76%	20%	4%	-	-
Combustion Chamber	75%	8%	-	4%	8%

Table C.1 - *Approximated chemical composition.*

Specific heat c_p and will be evaluated according to polynomial expressions like:

$$c_p = a + bT + cT^2 + dT^3 + \frac{e}{T^2}$$

where coefficients are given in thermochemical databases for each species.

This approach leads to a significantly different values in mean flow parameters. Despite of this statement, thermal power has to be set in order to get the proper temperature in combustion chamber. This fact highlight a new problem: what temperature should be obtained in combustion chamber? Indeed flame temperature is about 1633 K, but it suddenly decays in regions far from reactions decreasing to 1500 K. In figure C.2 eigenmodes for $\gamma = f(T, y_i)$ are shown for two different combustion chamber temperature compared to those obtained for c_p and c_v independent from T and y_i .

Luckily results are not so different: thus the choices to have a temperature independent γ and a combustion chamber temperature near to the flame one are not so critical for eigenmodes' evaluation. Nevertheless computational time does not grow and the assumption of constant γ could be overcome anyway.

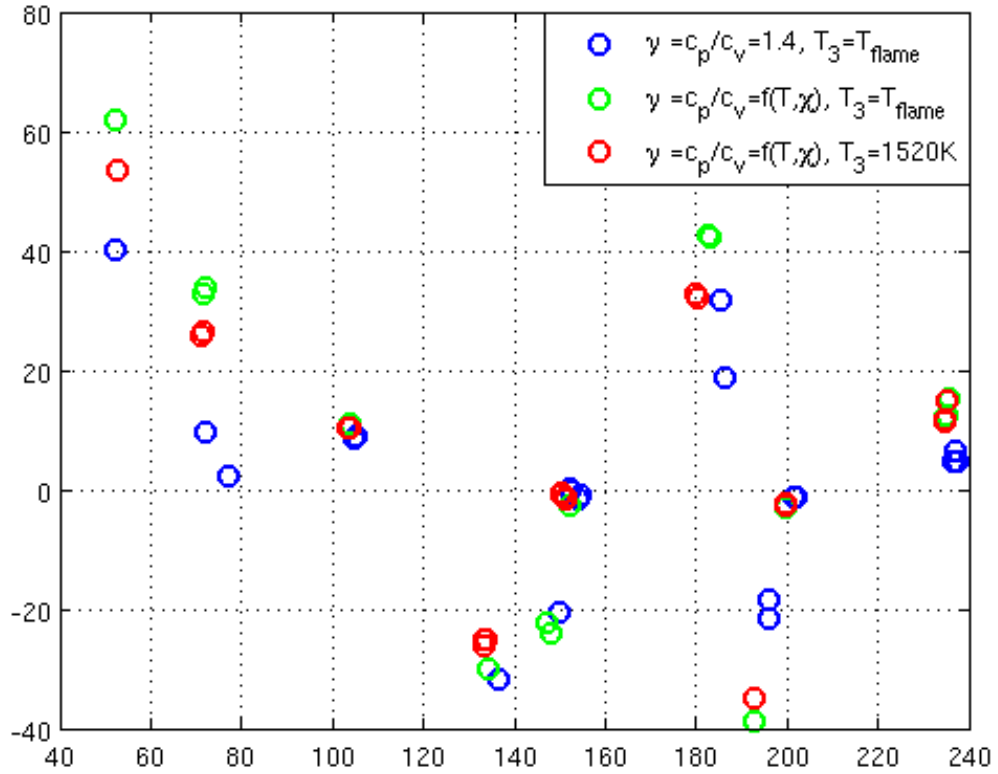


Figure C.2 - 20 CBO's configuration, $\tau=7$ ms, $\kappa=1$, hard wall BC at inlet and outlet.
 o: $\gamma=const$, $T_3 = T_{flame}$; o: $\gamma = f(T, y_i)$, $T_3 = T_{flame}$; o: $\gamma = f(T, y_i)$, $T_3 = 1520K$.

Here follows the three MATLAB functions useful to provide the proper values for c_p , c_v and γ in each duct.

Function for c_p and γ computation in the plenum.

```
function [cp_air , g_air]=g-plenum(T)

R=8.314472;    % J/(mol K)
t=T./1000;    % T in Kelvin

%----- O_2 -----
%-----

PM_O2=32;      % g/mol
R_O2=R./PM_O2; % kJ/(kg K)

a2=31.32234;
b2=-20.23531;
c2=57.86644;
d2=-36.50624;
e2=-0.007374;

cp_O2= (a2 + b2.*t + c2.*t.^2 + d2.*t.^3 + e2./t.^2)./PM_O2;
cv_O2=cp_O2-R_O2;

%----- N_2 -----
%-----

PM_N2=28;      % g/mol
R_N2=R./PM_N2; % kJ/(kg K)

a3=28.98641;
b3=1.853978;
c3=-9.647459;
d3=16.63537;
e3=0.000117;

cp_N2= (a3 + b3.*t + c3.*t.^2 + d3.*t.^3 + e3./t.^2)./PM_N2;
cv_N2=cp_N2-R_N2;

%----- air -----
%-----

cp_air=cp_N2.*.79+cp_O2.*.21;
cv_air=cv_N2.*.79+cv_O2.*.21;
g_air=cp_air./cv_air;

cp_air = cp_air.*1000 ;    %[J kg^-1 K^-1]
```

Function for c_p and γ computation in the premixers.

```

function [cp_un , g_un]=g-premix(T)

R=8.314472;    % J/(mol K)
t=T./1000;

%----- CH_4 -----
%-----
PM_CH4=16;          % g/mol
R_CH4=R./PM_CH4;   % kJ/(kg K)

a1=-0.703029;
b1=108.4773;
c1=-42.52157;
d1=5.862788;
e1=0.678565;

cp_CH4=(a1 + b1.*t + c1.*t.^2 + d1.*t.^3 + e1./t.^2)./PM_CH4;
cv_CH4=cp_CH4-R_CH4;

%----- O_2 -----
%-----
PM_O2=32;          % g/mol
R_O2=R./PM_O2;    % kJ/(kg K)

a2=31.32234;
b2=-20.23531;
c2=57.86644;
d2=-36.50624;
e2=-0.007374;

cp_O2=(a2 + b2.*t + c2.*t.^2 + d2.*t.^3 + e2./t.^2)./PM_O2;
cv_O2=cp_O2-R_O2;

%----- N_2 -----
%-----
PM_N2=28;          % g/mol
R_N2=R./PM_N2;    % kJ/(kg K)

a3=28.98641;
b3=1.853978;
c3=-9.647459;
d3=16.63537;
e3=0.000117;

cp_N2=(a3 + b3.*t + c3.*t.^2 + d3.*t.^3 + e3./t.^2)./PM_N2;
cv_N2=cp_N2-R_N2;

```

% unburned _____
 % _____

xN2=.76;
 xO2=.2;
 xCH4=.04;

cp_un=cp_N2.*xN2+cp_O2.*xO2+cp_CH4.*xCH4;
 cv_un=cv_N2.*xN2+cv_O2.*xO2+cv_CH4.*xCH4;
 g_un=cp_un./cv_un;

cp_un = cp_un.*1000 ; % [J kg⁻¹ K⁻¹]

Function for c_p and γ computation in the combustion chamber.

function [cp_b , g_b]=g_chamber(T)

R=8.314472; % J/(mol K)
 t=T./1000;

% N2 _____
 % _____

PM_N2=28; % g/mol
 R_N2=R./PM_N2; % kJ/(kg K)

a1=19.50583;
 b1=19.88705;
 c1=-8.598535;
 d1=1.369784;
 e1=0.527601;

cp_N2= (a1 + b1.*t + c1.*t.^2 + d1.*t.^3 + e1./t.^2)./PM_N2;
 cv_N2=cp_N2-R_N2;

% H2O _____
 % _____

PM_H2O=18; % g/mol
 R_H2O=R./PM_H2O; % kJ/(kg K)

a2=30.09200;
 b2=6.832514;
 c2=6.793435;
 d2=-2.534480;
 e2=0.082139 ;

cp_H2O= (a2 + b2.*t + c2.*t.^2 + d2.*t.^3 + e2./t.^2)./PM_H2O;
 cv_H2O=cp_H2O-R_H2O;

% O₂ _____
%

PM_{O2}=32; % g/mol
R_{O2}=R./PM_{O2}; % kJ/(kg K)

a3=30.03235;
b3=8.772972;
c3=-3.988133;
d3=0.788313;
e3=-0.741599;

cp_{O2}=(a3 + b3.*t + c3.*t.^2 + d3.*t.^3 + e3./t.^2)./PM_{O2};
cv_{O2}=cp_{O2}-R_{O2};

% CO₂ _____
%

PM_{CO2}=44; % g/mol
R_{CO2}=R./PM_{CO2}; % kJ/(kg K)

a4=58.16639;
b4=2.720074;
c4=-0.492289;
d4=0.038844;
e4=-6.447293;

cp_{CO2}=(a4 + b4.*t + c4.*t.^2 + d4.*t.^3 + e4./t.^2)./PM_{CO2};
cv_{CO2}=cp_{CO2}-R_{CO2};

% burned _____
%

xN₂=.75;
xO₂=.08;
xCO₂=.04;
xH₂O=.08;

cp_b=cp_N₂. * xN₂+cp_O₂. * xO₂+cp_CO₂. * xCO₂+cp_H₂O. * xH₂O;
cv_b=cv_N₂. * xN₂+cv_O₂. * xO₂+cv_CO₂. * xCO₂+cv_H₂O. * xH₂O;
g_b=cp_b./cv_b;

cp_b = cp_b.*1000 ; %[J kg⁻¹ K⁻¹]

Appendix D

LOMTI user guide

LOMTI is composed by several M-file (either scripts or functions). Just to understand how to find out an eigenmode with its relative eigenfunctions let us go through each step required describing the aim of each M-file encountered.

Mean flow computation First of all we have to calculate the mean flow values \bar{G}_i in each duct i . We have to run the function *mean flow.m* from the command window: as we can see in figure D.1 *mean flow.m* requires two entries. The first one, *guess.m*, is a script including geometrical and thermodynamic values (*guess.m* must be already present in the same folder of *mean flow.m*). The second one, *data.m*, is an M-file created by *mean flow*. In *guess.m* we have to set:

- all geometrical values of plenum, premixers and combustion chamber including whether *CBO's* are present or not;
- inlet pressure, temperature and mass flow rate (these values should be known);
- flame thermal power (this value is actually unknown, we have to tune it in order to provide the desired flame temperature in *data.m*);
- whether to take into account cooling or not;
- give initial values for thermodynamic variables required to start the optimization process;
- inlet/outlet boundary conditions (they will be useful only in the eigenmodes computation since mean flow boundary conditions have been already set, when we chose inlet pressure, temperature and mass flow rate)
- flame transfer function's parameters such as the distance of the reference point from the flame front (*dref*), FTF itself (*TF=2*) or $\kappa - \tau$ values for each burner;
- porosity of the grid upstream of each flame front.

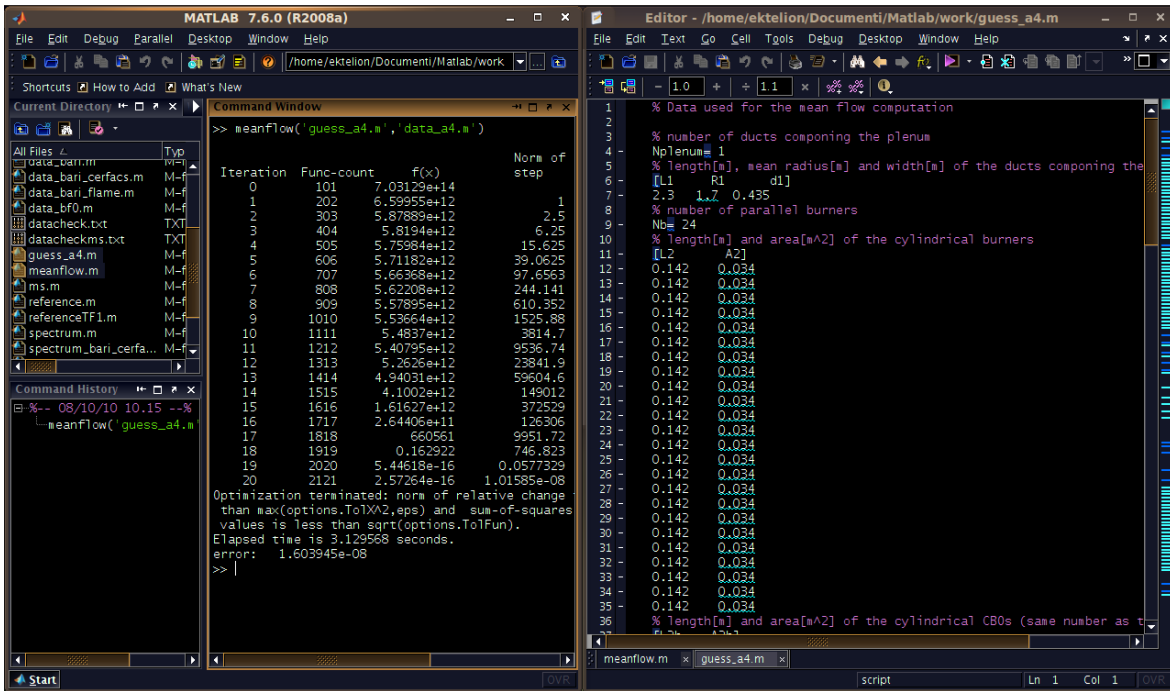


Figure D.1 - Screen shot after mean flow computation.

If we set $cerfacs=1$ $\kappa - \tau$ values will be computed as a function of ω_r and the values below are not read, otherwise we have to set $\kappa - \tau$ for each burner. When the optimization is terminated we have to check whether $f(x)$ and $Norm\ of\ step$ are small. If this does not occur probably the initial guess is too far from the solution. A first attempt to find out best initial values is to use the last ones obtained from the optimization: if the initial guess is very far from the solution this procedure hardly lead to acceptable results. Thus we have to check in the optimization phase which values are most affected by iterations and try to provide best initial guesses for them. Once the procedure is converged it is convenient to substitute initial values in *guess.m* with solution just obtained, in order to save time in further simulation; in fact, with initial guess very close to the possible solutions no more than 30 iterations are generally required for convergence. This means very few seconds of time machine as we can see in the penultimate line of the command window.

Refreshing the current folder, a new M-file, *data.m*, is present. Before proceeding any further let us check whether *data.m* is coherent with *guess.m*. First of all we have to check if the flame temperature T_3 is effectively correct, furthermore it is recommended to check whether R , c_p , γ , c_s and M assume acceptable values in each duct. As we can see *mean flow.m* could never be open during the computation of the mean flow, since it is only necessary to call it from the command window.

Eigenmodes computation We are now able to start looking for eigenmodes. We have to open the function *turbine.m*. This is the core of LOMTI: here most of the functions are called in order to find out the zero of the determinant. Let us examine all of its features.

Main code *turbine.m*.

```
function [x0,y0] = turbine%(xmin,xmax,ymin,ymax,Nr,Ni,x)

% tic

% time at the beginning of the computation
%-----
clk = clock;
disp(['Computation started at ', ...
      num2str(clk(4)), 'h ', num2str(clk(5)), ...
      'm ', int2str(clk(6)), 's']);

% path to the routines used during the computation
%-----
addpath('./routines');

% data read in file data
%-----
data='data_a4.m';
init

% Definition of omega
%-----
Nr=53; Ni=53;

%eps=1e-10;

xmin=140;
xmax=145;
ymin=eps;
ymax=5;
% test : xmin should not be exactly zero
if (xmin==0)
    error('xmin should not be exactly zero !!');
end

xmin = 2.*pi.*xmin;
xmax = 2.*pi.*xmax;

% grid
[x1,x2] = meshgrid(linspace(xmin,xmax,Nr), linspace(ymin,ymax,Ni));
omega=x1 +1i*x2;
omega=omega(:);

% checkdata: data written in file datacheck.m
%-----
datacheck = 'datacheck.txt';
```

checkdata

```

%%%%%%%%%%%%%%%%%%%%%%%%%%%%%%%%%%%%%%%%%%%%%%%%%%%%%%%%%%%%%%%%%%%%%%%%
% computation of the wave numbers : Kp, Km, K0, Kp/alphap , Km/alpham
%%%%%%%%%%%%%%%%%%%%%%%%%%%%%%%%%%%%%%%%%%%%%%%%%%%%%%%%%%%%%%%%%%%%%%%%
[Kp1, Kp2, Kp2b, Kp3, Km1, Km2, Km2b, Km3, K01, K02, K02b, K03, ...
    Kap1, Kap2, Kap2b, Kap3, Kam1, Kam2, Kam2b, Kam3] = ...
    disp_relation(Nr*Ni, Np, Nb, Ncbo,...
    Nc, omega, n, R1, R3, M, Cs, U);

%%%%%%%%%%%%%%%%%%%%%%%%%%%%%%%%%%%%%%%%%%%%%%%%%%%%%%%%%%%%%%%%%%%%%%%%
% computation of the boundary conditions
%%%%%%%%%%%%%%%%%%%%%%%%%%%%%%%%%%%%%%%%%%%%%%%%%%%%%%%%%%%%%%%%%%%%%%%%
[Y1, Y3, Ye1, Ye3] = bc(Nr*Ni, Nb, Nc, bc_in , bc_out , Kap1, Kam1, ...
    Kap3, Kam3, Kp3, Km3, K03, U1, Cs1, U3, Cs3, Lc3, gam_gas);

%%%%%%%%%%%%%%%%%%%%%%%%%%%%%%%%%%%%%%%%%%%%%%%%%%%%%%%%%%%%%%%%%%%%%%%%
% computation of the FTF parameters calculated by CERFACS
%%%%%%%%%%%%%%%%%%%%%%%%%%%%%%%%%%%%%%%%%%%%%%%%%%%%%%%%%%%%%%%%%%%%%%%%
if (cerfacs==1)
    [tau, kappa]=ntau_cerfacs(omega, indCBO, indnoCBO, Nb);
elseif (cerfacs==0) % otherwise, use the values in the input file
    tau = repmat( tau,length(omega),1);
    kappa = repmat(kappa,length(omega),1);
end

%%%%%%%%%%%%%%%%%%%%%%%%%%%%%%%%%%%%%%%%%%%%%%%%%%%%%%%%%%%%%%%%%%%%%%%%
% computation of the resolution matrix
%%%%%%%%%%%%%%%%%%%%%%%%%%%%%%%%%%%%%%%%%%%%%%%%%%%%%%%%%%%%%%%%%%%%%%%%
% Zhowe computed if howe=1 or Zhowe=0 if howe=0
Zhowe = Z_howe(omega, a_grid, h_grid, ...
rho2, U2, N_grid, S2) .* howe;

Amat = MAT(Nr*Ni, Nmat, Np, Nb, Nmodes, Ncbo, Nc, ...
    indCBO, indnoCBO, omega, jump1, jump3, ...
    Kp1, Kp2, Kp2b, Kp3, Km1, Km2, Km2b, Km3, ...
    K01, K02, K02b, K03, ...
    Kap1, Kam1, Kap2, Kam2,...
    Kap2b, Kam2b, Kap3, Kam3, ...
    kappa, tau, Q, rho, U, Cs, S, Lc, H, ...
    R1, R3, d1, d3, coeff1_theta, coeff3_theta, ...
    Y1, Y3, Ye1, Ye3, beta3, n,...
    theta, Zhowe, gam_gas, TF, dref);

Amat = reshape(Amat,Nmat,Nmat,Nr*Ni) ;

for i = 1:Nmat
    % isolate each colon of the matrix
    MATcolon = Amat(:,i,:);

```

```

    % identify the element of maximum absolute value
    MATmax = max(abs(MATcolon(:)));

    % divide all the elements of the colon by MATmax
    Amat(:,i,:) = MATcolon./MATmax;

end

%-----
% Matrix scaling
x=30;% x=15;
Amat = x.* Amat;
disp('-----')
disp(['Matrix scaling , x= ', num2str(x)]);
disp('-----')

if any(isinf(Amat(:)))
    error('Some elements of the matrix go to infinity ')
end
if any(isnan(Amat(:)))
    error('Some elements of the matrix are NAN')
end

%%%%%%%%%%%%%%%%%%%%%%%%%%%%%%%%%%%%%%%%%%%%%%%%%%%%%%%%%%%%%%%%%%%%%%%%%%
% computation of the determinant
%%%%%%%%%%%%%%%%%%%%%%%%%%%%%%%%%%%%%%%%%%%%%%%%%%%%%%%%%%%%%%%%%%%%%%%%%%
% toc
disp('I have completed the matrix computation ')
format long g
ildet=det_A(Amat, Nmat, Nr, Ni);

%-----
% Look for the zero or NAN values of the determinant

a=isnan(ildet);
a(a==0)=[];

if (isempty(a)==0)
    error('the determinant ildet has values equal to NAN');

elseif (isempty(ildet(ildet==0))==0)
    error('the determinant ildet has values equal to 0 ');
end

```

```
%-----  
% Maximum and minimum values of the determinant  
format long g  
dmax = max(ildet (:));  
dmin = min(ildet (:));  
  
% toc  
disp('I have completed the determinant computation')  
disp(['The max value in the determinant...  
(in absolute value) is ', num2str(dmax, '%1.2e')]);  
disp(['The min value in the determinant...  
(in absolute value) is ', num2str(dmin, '%1.2e')]);  
disp('-----')  
  
%%%%%%%%%%%%%%%%%%%%%%%%%%%%%%%%%%%%%%%%%%%%%%%%%%%%%%%%%%%%%%%%%%%%%%%%  
% computation of the eigenmodes  
%%%%%%%%%%%%%%%%%%%%%%%%%%%%%%%%%%%%%%%%%%%%%%%%%%%%%%%%%%%%%%%%%%%%%%%%  
[x0,y0] = find_eig(ildet , x1, -x2);  
  
  
% plot of the eigenmodes  
%-----  
figure(1), hold on, box on, grid on  
  
plot(x0,y0,'go','Markersize',18,'linewidth',2);  
%plot(x0,y0,'mo','Markersize',8,'linewidth',2);  
  
xlabel('Frequency','fontsize',18);  
ylabel('growth rate','fontsize',18);  
set(gca,'fontsize',18,'linewidth',2); box on
```

We have to call *turbine.m* from the command window. If we set its outputs as a vector composed by frequency f and growth rate GR it will be easier to manage them successively. Before running *turbine.m* we have to set something in its formulation. First of all we have to say which set of data should be used (we set $data='data-a4.m'$ just obtained¹). Then the number of discretization N_r and N_i in the complex plane should be set: this setting must be done once since it depends only on the effective physical memory (RAM) available at the moment.² This does not directly affect the accuracy of the solution but it affects the dimension of the current computational domain in order to obtain the same solution. This domain must be set giving the proper values to $xmin$, $xmax$ [Hz], $ymin$, $ymax$ [s^{-1}] that represent frequency and growth rate range where the latter has changed sign (this means that searching from $ymin=5$ to $ymin=10$ will find values in the stable half-plane where GR is negative). None of these values must be exactly equal to zero: zero frequencies have no physical meaning for

¹Remember to put it inside quotes since it is managed like a string.

² $N_r = N_i = 53$ is a proper value for an effective RAM equal to 3.2 GB.

our purposes; zero growth rate leads to numerical singularities that give a multitude of neutral eigenmodes. This fact is to be avoided using a small values $\pm eps$ instead of zero. Then a grid is created using the function *meshgrid* already implemented in MATLAB. Data are checked with the script *checkdata* located in the */routines* folder. Then wave numbers, boundary conditions, FTF parameters (if *cerfac=1*) and the resolution matrix are computed with, respectively, *disp-relation*, *bc*, *ntau-cerfac* and *MAT* functions. Since the values of the determinant could go to *NaN* or to zero it is necessary to renormalize the matrix multiplying a number on each line. We have to rescale matrix every time we go far from zero growth rate where determinant become very large (stable half-plane) or very small (unstable half-plane). Now the determinant is computed with *det-A* and an error message is shown if the scaling have not sorted the desired results (i.e. reducing the determinant value to a finite number). Eigenmodes are directly calculated by the function *find-eig* that finds the graphical intersections of the lines representing $real\{det(X)\} = 0$ and $imag\{det(X)\} = 0$. Since solutions are obtained from a graphical procedure they are reliable approximately to the fifth digit. Finally, two figures are plotted: one represents the isolines of the determinant and the other plots only their intersections. The first one is very important since its features provide information on the reliability of the results: lines must always appear with smooth variations, otherwise a closer window must be investigated (for example Window called 'Figure 110' in screenshot D.3 is still too large to get an accurate value for f and GR). It is clear that several windows must be analyzed in order to detect all the modes present in the whole plane. Just to make this work faster it is useful to analyze first very large windows that give an idea of the location of several modes (see appendix B), then focus on the place where the determinant displays perturbations in its trend.

In screenshot D.4 the proper closer window that have smooth variations in isolines is shown. This is a particular case where \bar{u} is very close to zero in each duct. This fact increases the number of oscillations of the determinant in a range of frequencies, thus a very small window is necessary to completely rely on the results. Fortunately, when the Mach number assumes a large value, larger windows are adequate to get smooth isolines.

Radial Dependency If the code with radial dependency is used it is necessary to define which radial mode we are investigating just after the call of *turbine.m* or directly writing $[f,GR]=turbine(m)$ ($m = 0$ for no radial dependency).

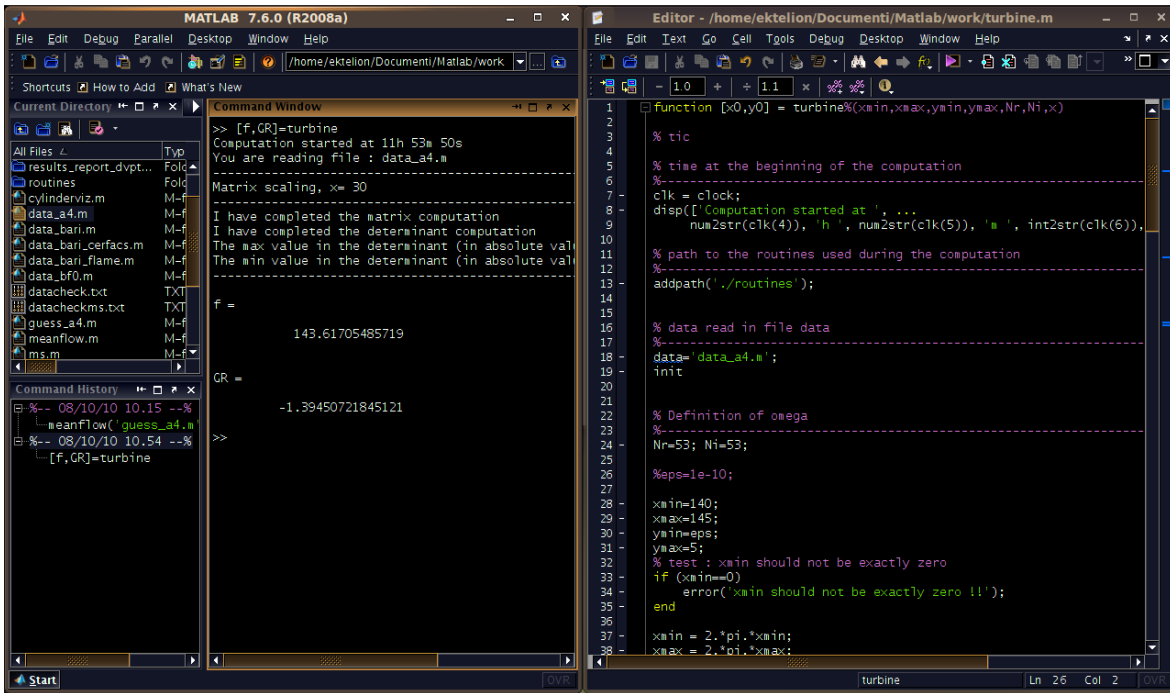


Figure D.2 - Screenshot after `turbine.m` run.

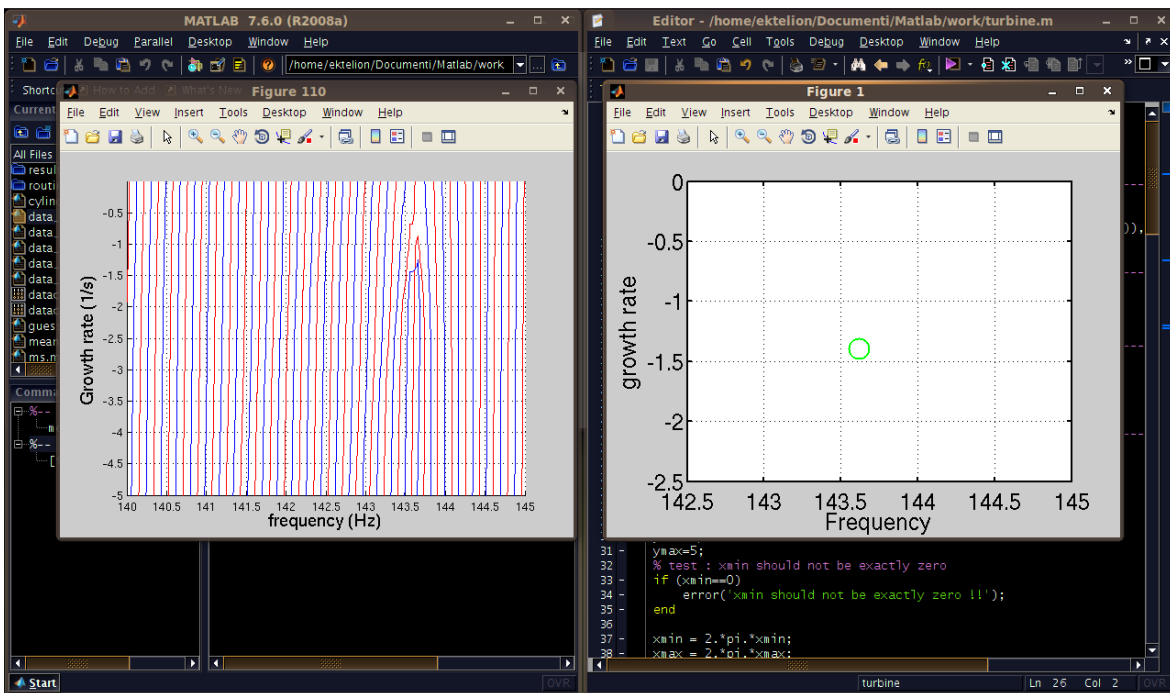


Figure D.3 - Screenshot of the windows obtained from `turbine.m`.

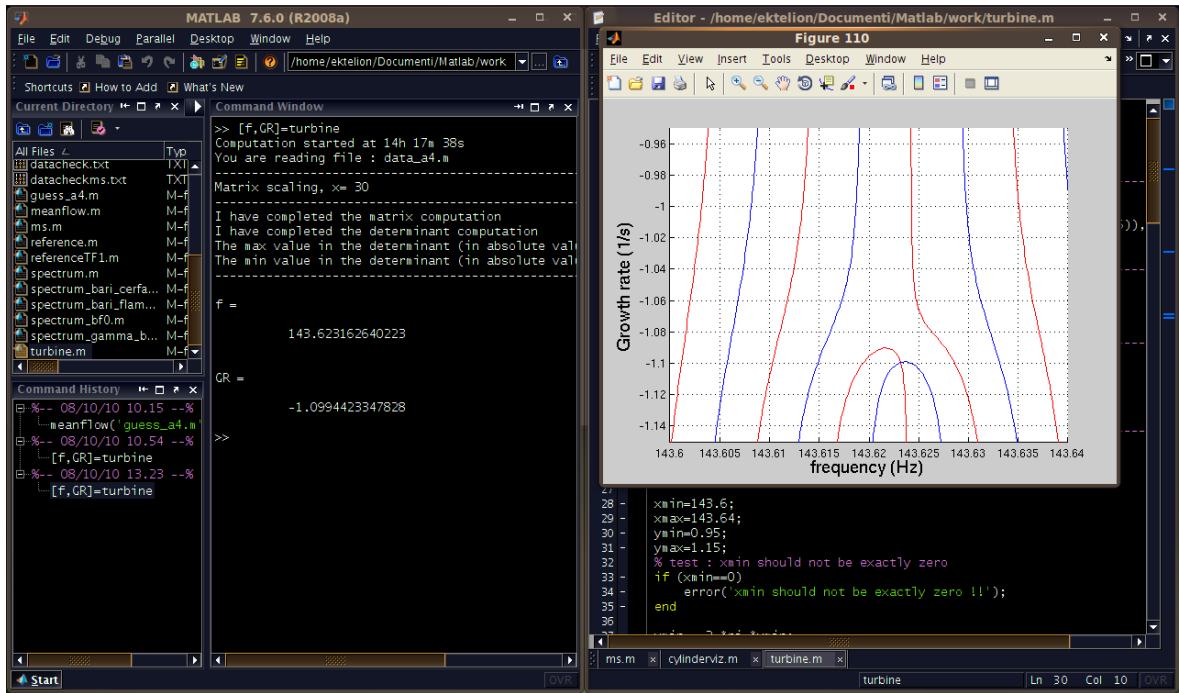


Figure D.4 - Screenshot after `turbine.m` run with a smaller window.

Mode shapes Once we have the proper value for f and GR we can open `cylinderviz.m` or `ms.m`. The script `cylinderviz.m` provides a three-dimensional image of pressure perturbations. To run this script we have to set $fre = f$ and $fri = GR$ and $data='data-a4.m'$. The variable $ntps$ represents the number of images taken in each period. It has to be set greater than 2 if we want to generate $ntps-1$ images (for a good resolution in time $ntps > 10$ is suggested). In order to generate a .gif (or .avi) file from the frame obtained another program not present in MATLAB (such as GIMP) is needed.

The script `ms.m` is useful to provide eigenfunctions of several variables at different θ as a function of x . Setting this script is equivalent to setting `cylinderviz.m`.

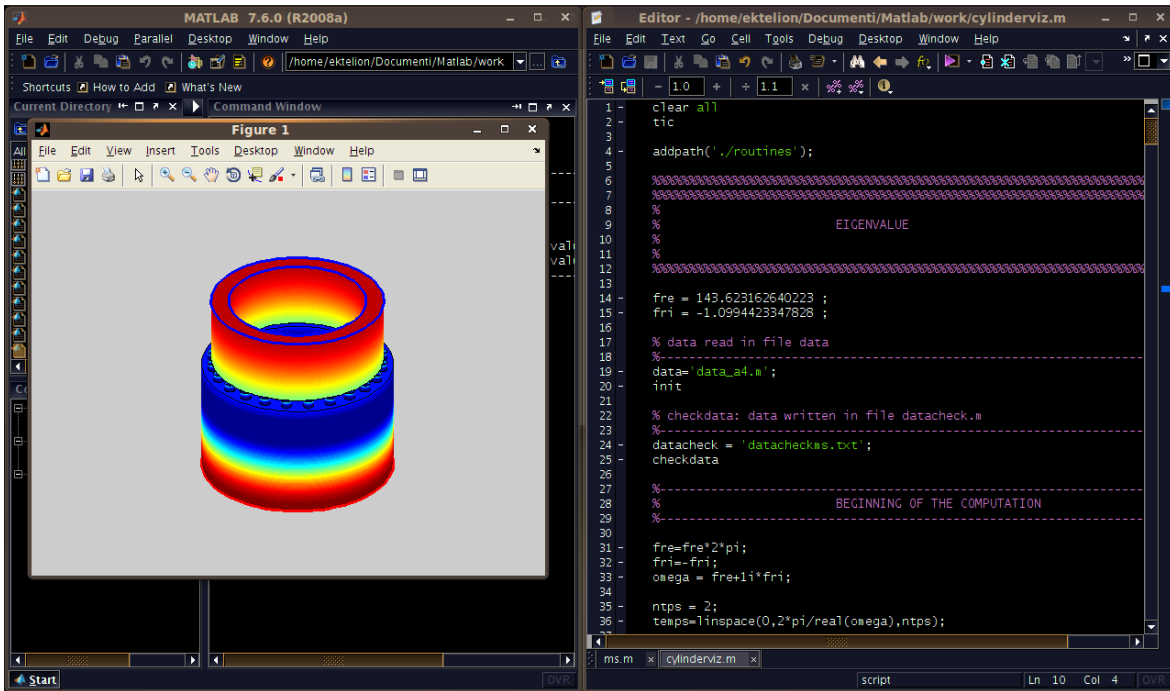


Figure D.5 - Screenshot after *cylinderviz.m* run with $ntps=2$.

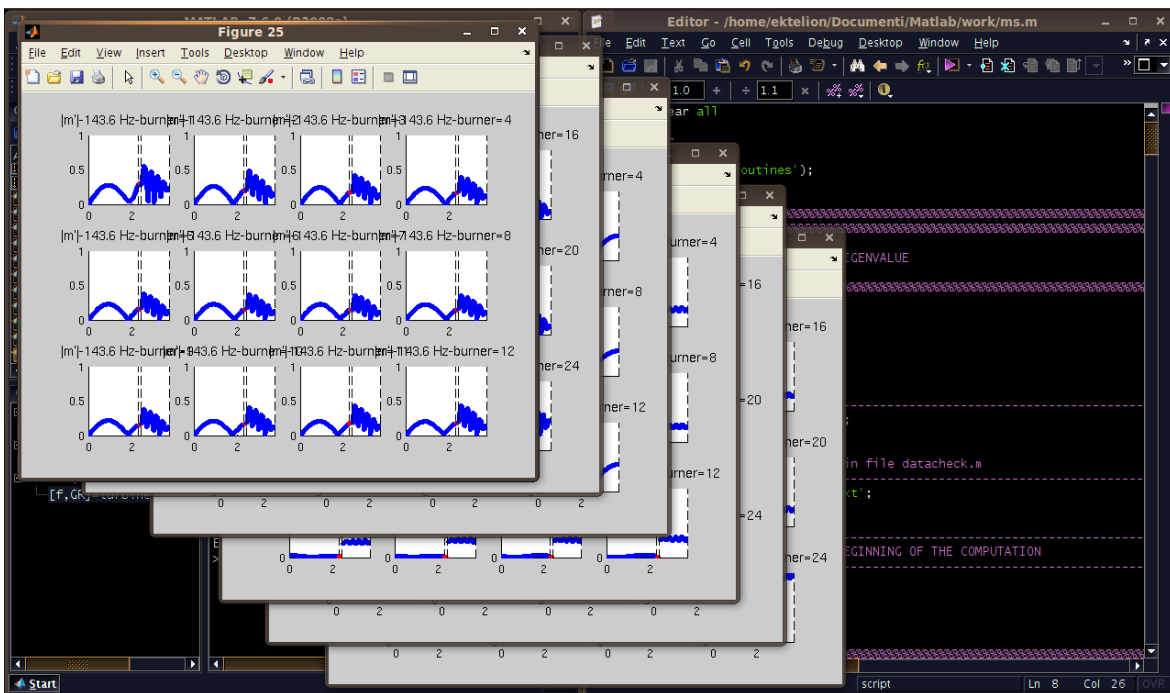


Figure D.6 - Screenshot after *ms.m* run.

Bibliography

- [1] M.Bargiacchi: *Instabilità termoacustiche in un condotto*, Tesi di Laurea Triennale in Ingegneria Meccanica, UNIGE, 2008
- [2] B.Higgins: *Journal of Natural Phylosophy and Chemical Arts*, Vol.1, 129, 1802
- [3] A.P.Dowling: *The calculation of thermoacoustic oscillations*, Journal of Sound and Vibration (1995) **180**(4), 557-581
- [4] S.Kato, T.Fujimori, A.P.Dowling, H.Kobayashi: *Effect of heat release distribution on combustion oscillation*, Proceedings of the Combustion Institute 30 (2005) 1799-1806
- [5] A.P.Dowling, S.R.Stow: *Acoustic Analysis of Gas-turbine Combustors*, Journal of Propulsion and Power, Vol. 19 (13). pp. 369-410 (2005)
- [6] G.J.Bloxside, A.P.Dowling, P.J.Langhorne: *Reheat buzz: an acoustically coupled combustion instability. Part 2. Theory*, J. Fluid Mech. (1988), vol 193, pp. 445-473
- [7] A.Quarteroni, F.Saleri: *Introduzione al calcolo scientifico*, Springer (2006), pp. 124-129
- [8] S.M.Sarpotdar, N.Ananthkrishnan, S.D.Sharma: *The Rijke Tube A Thermoacoustic Device*, Department of Aerospace Engineering Indian Institute of Technology (Bombay), (2003)
- [9] F.Nicoud, T.Poinsot: *Thermoacoustic instabilities: Should the Rayleigh criterion be extended to include entropy changes?*, Combustion and Flame 142 (2005) 153-159
- [10] B.T.Chu: *On the energy transfer to small disturbances in fluid flow (Part I)*, Acta Mech. (1965) 215-234
- [11] T.C.Lieuwen: *Physiscs of Premixed Combustion-Acoustic Wave Interaction*, Journal of Propulsion and Power, Vol. 19 (12). pp. 315-362 (2005)
- [12] A.Di Vita: *On Rayleigh's criterion and stability of premixed flames*, Technical report Ansaldo Ricerche (2008)
- [13] G.Campa, S.M.Camporeale: *Influence of flame and burner transfer matrix on thermoacoustic combustion instability modes and frequency*, Proceedings of ASME Turbo Expo 2010: Power for Land, Sea and Air, June 14-18,2010, Glasgow,UK

- [14] S.Evesque, W.Polifke: *Low order acoustic modelling for annular combustors: validation and inclusion of modal coupling*, Proceedings of ASME Turbo Expo 2002: June 3-6,2002, Amsterdam, Netherlands
- [15] J.Favier: *Coupling between combustion instabilities in annular combustors with multiple burners*, Technical report Ansaldo Energia (2009)
- [16] A.Guaus: *Mean flow computation in a model of the Sesta's burner based on experimental data*, Technical report Ansaldo Energia (2009)
- [17] K.Truffin, T.Poinsot: *Comparison and extension of methods for acoustic identification of burners*, Combustion and Flame, 142(4):388-400 (2005)
- [18] M.A.Ceviz, I.Kaymaz: *Temperature and airfuel ratio dependent specific heat ratio functions for lean burned and unburned mixture*, Energy Conversion and Management 46 (2005) 2387-2404
- [19] < <http://webbook.nist.gov/chemistry/> > 2010, May
- [20] D.You, V.Yang, X.Sun: *Three-dimensional linear stability analysis of gas turbine combustion dynamics*, Pennsylvania State University, University Park, Pennsylvania, AIAA 2005
- [21] A.P.Dowling: *Modelling and control of combustion oscillations*, ASME Turbo Expo June 6-9, 2005, Reno-Tahoe, Nevada, GT2005-68452
- [22] A.L.Birbaud, S.Ducruix, D.Durox, S.Candel: *The nonlinear response of inverted "V" flames to equivalence ratio nonuniformities*, Combustion and Flame 154 (2008) 356-367
- [23] W.Polifke, C.Lawn: *On the low-frequency limit of flame transfer functions*, Combustion and Flame 151 (2007) 437-451
- [24] G.Campa, S.M.Camporeale: *Modellistica Termoacustica dell'Instabilità di Combustione*, Technical report Ansaldo Energia 2/3/2010
- [25] G.Campa: *Calcolo acustico camera anulare attuale*, Technical report Ansaldo Energia 28/5/2010
- [26] G.Campa, S.M.Camporeale: *Calcolo acustico camera anulare attuale*, Technical report Ansaldo Energia 12/7/2010
- [27] H.Shalaby, A.Laverdant, D.Thévenin: *Direct numerical simulation of a realistic acoustic wave interacting with a premixed flame*, Proceedings of the Combustion Institute 32 (2009) 1473-1480
- [28] V.Bellucci, P.Flohr, C.O.Paschereit, F.Magni: *On the Use of Helmholtz Resonators for Damping Acoustic Pulsations in Industrial Gas Turbines*, Journal of Engineering for Gas Turbines and Power, April 2004, Vol. 126/**271**

- [29] D. L. Gysling, G. S. Copeland, D. C. McCormick, W. M. Proscia: *Combustion System Damping Augmentation With Helmholtz Resonators*, Journal of Engineering for Gas Turbines and Power, April 2000, Vol. 122/**269**
- [30] S. Akamatsu, A. P. Dowling: *Three Dimensional Thermoacoustic Oscillation in a Premix Combustor*, Proceedings of ASME Turbo Expo 2001: June 4-7,2001, New Orleans, Louisiana
- [31] T.Poinsot: *SESTA: AVSP-LOMTI comparison*, Technical Report CERFACS, June 2010
- [32] A.Guaus: *Implementation in LOMTI of a model for the turbine AE94.3A*, Technical report, UNIGE (2010)
- [33] A.Guaus: *Implementation in LOMTI of the radial dependence for configurations with parallel burners*, Technical report, UNIGE (2010)
- [34] F.F.Ehrich: *Gas turbine engine with screech attenuating means*, US Patent, 3,437,173, 1969
- [35] F.Negro: *Proprietà delle interazioni forti in campi esterni*, Master Thesis, MFN UNIGE 2010
- [36] Trefethen LN, Trefethen AE, Reddy SC, Driscoll TA: *Hydrodynamic stability without eigenvalues*, Science, 1993, 261:578584
- [37] Stephen R. Turns: *An introduction to Combustion*, McGraw-Hill, 2000, 253-283
- [38] F.A.Williams: *Combustion theory*, Benjamin/Cummings Publishing Company, 1985, 581-584
- [39] H. Jones: *The Mechanics of Vibrating Flames in Tubes*, Proc. R. Soc. Lond. A 1977 353, 459-473
- [40] G.A.Richards, D.L.Straub, E.H.Robey: *Passive control Instabilities in Stationary Gas Turbine*, Journal of Propulsion and Power 19 (2005), pp. 533579
- [41] H.Ax, U.Stopper, W.Meier, M.Aigner, F.Güthe: *Experimental analysis of the combustion behavior of a gas turbine burner by laser measurement techniques*, GT2009-59171, ASME Turbo Expo 2009, June 8-12, 2009, Orlando, Florida

ídpǫm